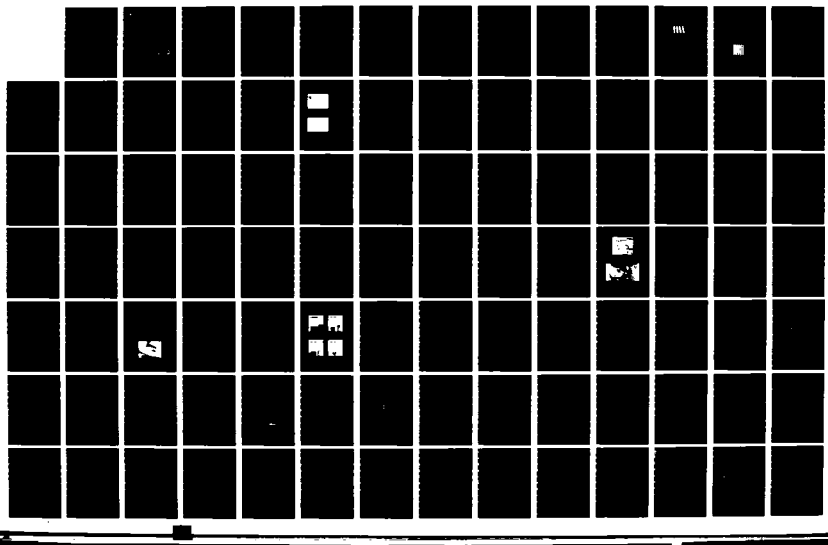


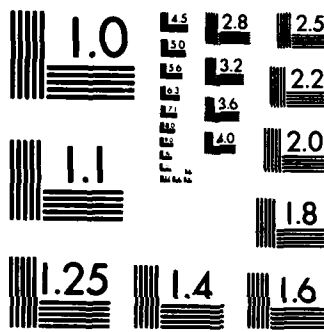
AD-A135 073 AIR FORCE ACADEMY AERONAUTICS DIGEST - FALL/WINTER 1982 1/2  
(U) AIR FORCE ACADEMY CO J DEJONGH ET AL SEP 83  
USAFRA-TR-83-15

UNCLASSIFIED

F/G 20/4

NL





MICROCOPY RESOLUTION TEST CHART  
NATIONAL BUREAU OF STANDARDS-1963-A

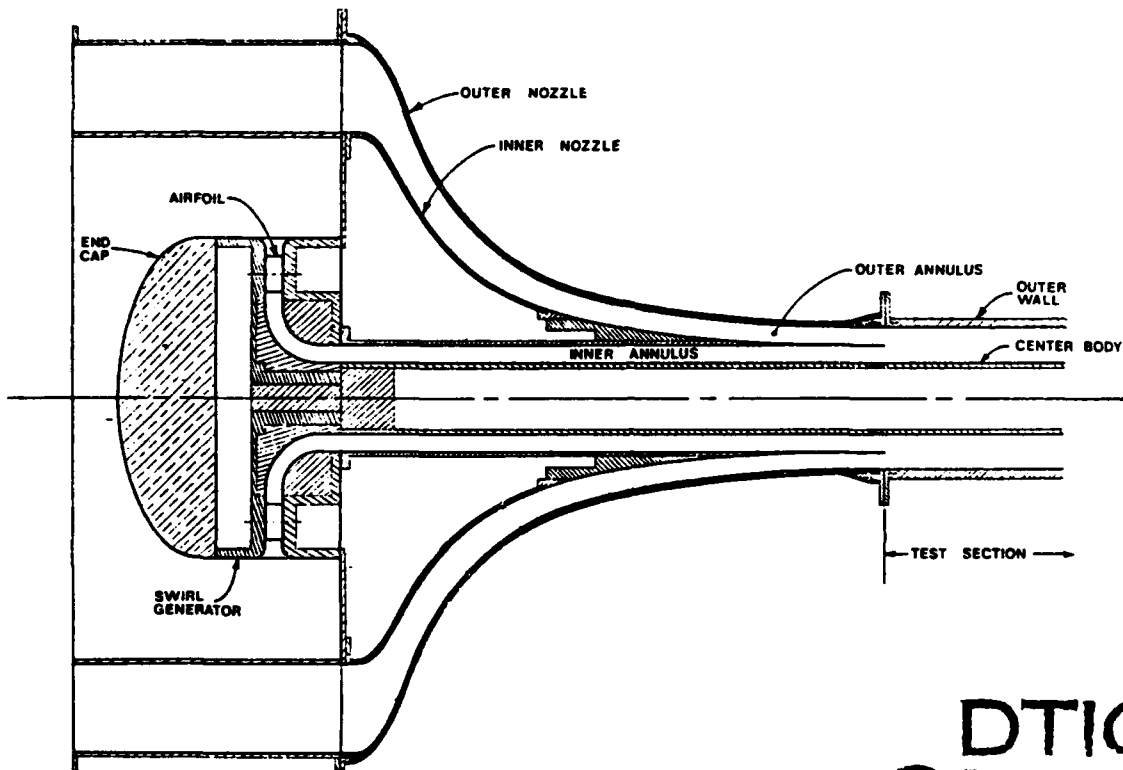


12

USAFA-TR-83-15

AD-A135073

# AIR FORCE ACADEMY Aeronautics Digest - Fall/Winter 1982



SWIRL GENERATOR & NOZZLES

SEPTEMBER 1983

Final Report

DTIC

NOV 30 1983

S H

APPROVED FOR PUBLIC RELEASE: DISTRIBUTION UNLIMITED

Department of Aeronautics  
Dean of the Faculty  
United States Air Force Academy  
Colorado 80840

DRAFT FILE COPY

83 11 20 195

COVER:

The cover shows a schematic of a swirl flow generator, which was used by Major Jack Mattingly in an experimental study of the mixing of 2 incompressible co-annular airstreams with substantial swirl present in the inner stream. For more information on the results of this study, see Major Mattingly's article in this issue of the Aeronautics Digest.

Editorial Review by Maj Robert M. Hogge, Department of English  
USAF Academy, Colorado Springs, Colorado 80840

This document is presented as a compilation of monographs worthy of publication. The United States Air Force Academy vouches for the quality of research, without necessarily endorsing the opinions and conclusions of the authors.

This Digest has been cleared for open publication and/or public release by the appropriate Office of Information in accordance with AFR 190-1 and DODD 5230.9. There is no objection to unlimited distribution of the Digest to the public at large, or by DTIC to the National Technical Information Service.

This Digest has been reviewed and is approved for publication.



Thomas E. McCann, Lt. Colonel, USAF  
Director of Research, Studies, and Analysis

UNCLASSIFIED  
SECURITY CLASSIFICATION OF THIS PAGE

REPORT DOCUMENTATION PAGE					
1a. REPORT SECURITY CLASSIFICATION <u>Unclassified</u>			1b. RESTRICTIVE MARKINGS		
2a. SECURITY CLASSIFICATION AUTHORITY			3. DISTRIBUTION/AVAILABILITY OF REPORT Approved for Public Release Distribution Unlimited		
2b. DECLASSIFICATION/DOWNGRADING SCHEDULE					
4. PERFORMING ORGANIZATION REPORT NUMBER(S)  USAFA-TR-83-15			5. MONITORING ORGANIZATION REPORT NUMBER(S)		
6a. NAME OF PERFORMING ORGANIZATION  Dept. of Aeronautics		6b. OFFICE SYMBOL (If applicable)	7a. NAME OF MONITORING ORGANIZATION		
6c. ADDRESS (City, State and ZIP Code)  U.S. Air Force Academy Colorado Springs, CO 80840			7b. ADDRESS (City, State and ZIP Code)		
8a. NAME OF FUNDING/SPONSORING ORGANIZATION		8b. OFFICE SYMBOL (If applicable)	9. PROCUREMENT INSTRUMENT IDENTIFICATION NUMBER		
8c. ADDRESS (City, State and ZIP Code)			10. SOURCE OF FUNDING NOS.  PROGRAM ELEMENT NO.      PROJECT NO.      TASK NO.      WORK UNIT NO.		
11. TITLE (Include Security Classification)  Air Force Academy Aeronautics Digest					
12. PERSONAL AUTHOR(S) EDITORS: DeJongh, J., Heiser, W., Hogge, R., Arends, M., Higgins, A.M., and Jumper, E.					
13a. TYPE OF REPORT  Final Report		13b. TIME COVERED FROM _____ TO _____		14. DATE OF REPORT (Yr., Mo., Day) 1983, September	15. PAGE COUNT
16. SUPPLEMENTARY NOTATION					
17. COSATI CODES			18. SUBJECT TERMS (Continue on reverse if necessary and identify by block number) Aerodynamics, Fluid Dynamics, Thermodynamics, Wave Equation, Skin Friction Drag, Swirling Flow, Square Missiles, Engineering Education, Optimal Control Strategy		
19. ABSTRACT (Continue on reverse if necessary and identify by block number)  This <u>Digest</u> covers unclassified research in aeronautics performed by individuals assigned to or associated with the United States Air Force Academy. This report includes technical papers in the specific areas of aerodynamics, propulsion, fluid dynamics, thermodynamics, and engineering education.					
20. DISTRIBUTION/AVAILABILITY OF ABSTRACT  UNCLASSIFIED/UNLIMITED <input checked="" type="checkbox"/> SAME AS RPT. <input type="checkbox"/> DTIC USERS <input type="checkbox"/>			21. ABSTRACT SECURITY CLASSIFICATION  Unclassified		
22a. NAME OF RESPONSIBLE INDIVIDUAL  Major Jay E. DeJongh			22b. TELEPHONE NUMBER (Include Area Code) 303-472-4010	22c. OFFICE SYMBOL DFAN	

## PREFACE

This report is the tenth issue of the Air Force Academy Aeronautics Digest\*. Our policy is to print articles which represent recent scholarly work by students and faculty of the Department of Aeronautics, members of other departments of the Academy and the Frank J. Seiler Research Laboratory, researchers directly or indirectly involved with USAFA-sponsored projects, and authors in fields of interest to the USAFA.

In addition to complete papers, the Digest includes, when appropriate, abstracts of lengthier reports and articles published in other formats. The editors will consider for publication contributions in the general field of Aeronautics, including:

- Aeronautical Engineering
  - Aerodynamics
  - Flight Mechanics
  - Propulsion
  - Structures
  - Instrumentation
- Fluid Dynamics
- Thermodynamics and Heat Transfer
- Biomechanics
- Engineering Education
- Aeronautical History

Papers on other topics will be considered on an individual basis. Contributions should be sent to:

Editor, Aeronautics Digest  
 DFAN  
 US Air Force Academy  
 Colorado Springs, CO 80840

The Aeronautics Digest is edited at present by Maj Jay E. DeJongh, PhD; William H. Heiser, PhD; Maj Robert M. Hogge, PhD, who provided the final editorial review; Maj A.M. Higgins, PhD; and Maj E.J. Jumper, PhD. Our thanks also to Associate Editor, Martha Arends, and Production Artist, Deborah Ross, of Contract Technical Services, Inc.



for  
NTIS

\*Previous issues of the Digest can be ordered from the Defense Technical Information Center (DTIC), Cameron Station, Alexandria, VA 22324.

VOL...	REV Codes
Avail and/or	
Dist	Special
A-1	

(CONT'D P. A.)

## CONTENTS

<u>Section</u>	<u>Page</u>
I. AERODYNAMICS	1
INVESTIGATION OF THE AERODYNAMICS OF SQUARE CROSS-SECTION MISSILES ----Nathan H. Jones and Gerald J. Zollars	2
II. INSTRUMENTATION	35
INVESTIGATION OF A STALL-ANTICIPATING DEVICE FOR AIRFOILS ----Scott P. Goodwin and William A. Buzzell	36
III. FLUID DYNAMICS	59
MIXING OF CONSTANT-AREA ANNULAR FLOWS WITH SWIRL ----Jack Denton Mattingly	60
IV. THERMODYNAMICS AND HEAT TRANSFER	100
NEW CONTROLS FOR ADVANCED RESIDENTIAL HEATING SYSTEMS ----Robert C. Winn	101
V. ENGINEERING EDUCATION	126
SOME TOPICS ON GAS BLOW WAVE PROPAGATION (PART 1) ONE ----Daniel H. Daley	127
VI. THE ENGINEER'S BOOKSHELF	140
ENGINEERS AND THE ART OF WRITING ----Robert M. Hogge	141
VII. ERRATA	147

**USAFA-TR-83-15**

**SECTION I**

**Aerodynamics**

INVESTIGATION OF THE AERODYNAMICS  
OF SQUARE CROSS-SECTION MISSILES

Nathan H. Jones\* and Gerald J. Zollars\*\*

Abstract

A series of tests were recently performed to expand the aerodynamic data base of square cross-section missiles. Forces and moments were measured on various square missile configurations in a subsonic wind tunnel. In addition, we quantitatively evaluated the flow field by measuring pressures in the vicinity of the leeward side of various missile configurations. The flow field surrounding the missile was found to vary significantly with changes in the missile's axial length position, corner radius variation, and roll angle variation. An increase in missile fineness ratio, however, did not affect the flow field substantially. Finally, the attachment of fins to the square cross-section missiles produced additional vortices in the flow field and a significant increase in the magnitude of forces and moments acting on the missiles.

I. Introduction

A still unresolved problem faced by missile designers is how to fit square components efficiently into missiles that have round cross sections. While a square cross-section missile would improve packing efficiency and yield a greater usable volume for a given frontal area, it must be designed aerodynamically so that it will not produce undesirable flight qualities.

Unfortunately, there is very little aerodynamic data on square cross-sectional bodies. Two-dimensional studies of noncircular cylinders were conducted by Polhamus (Refs. 1 and 2); square missiles, at high angles of attack, were examined by Clarkson, et al. (Ref. 3); and, more recently, Knoche, Schamel, and Schneider analyzed the general aerodynamics of square missiles (Refs. 4 and 5). But, in general, the data base is still too limited to allow for development and production of square missiles.

To widen this data base, the USAF Armament Laboratory and the USAF Academy have been conducting a research program to analyze the aerodynamic

---

\*CIC, USAF Academy

\*\*Major, USAF, Assistant Professor of Aeronautics, DFAN

characteristics of square cross-section missiles. The purpose of this paper is to supplement previous studies conducted at the Air Force Academy (Refs. 6, 7, and 8). We do not intend to provide a physical interpretation of all of the wind-tunnel test data, but only to report the results as observed or measured in the experiment. Flow fields of various square-missile configurations were investigated by measuring pressures and velocities on the leeside of the square missiles at various stations along the missiles' length. In addition, pressures and velocities were obtained in a flow field plane arbitrarily set approximately 2/3 of the missiles' length back from the nose to determine roll angle and corner radius effects. Fin effects were also investigated by measuring forces and moments acting on the finned missiles and by evaluating the flow field through measuring pressures on the leeward side of finned missiles. Finally, limited data were collected to determine the effects of fineness ratio (the ratio of missile length to width). A detailed analysis of the results of these tests follows the discussions of the wind tunnel, test apparatus, wind-tunnel models, and measurement techniques.

## II. Wind Tunnel

All testing was done in the USAF Academy subsonic wind tunnel, a continuous-flow, closed-circuit tunnel having a 2- x 3-feet-wide test section and an operating Mach number range of 0.04 to 0.35 at atmospheric pressure. A maximum Reynolds number per unit length of 1.6 million per foot is possible in this tunnel, which is fully described in Ref. 9.

## III. Test Apparatus

A seven-hole probe (described in Ref. 10) was used to measure leeside pressures and flow velocities. The probe was developed at the Air Force Academy and calibrated for incompressible flows up to Mach 0.3. Because

of its small diameter (approximately 0.1 inches), this probe did not significantly disturb the flow. Also, the probe has demonstrated 95 percent accuracy in measuring flows at angles up to 80 degrees off the probe axis (Ref. 10), making it a very reliable tool for performing pressure and cross-velocity measurements in complicated flows.

A 3-directional, traverse mechanism was used to position the probe (Figure 1). Once the probe was positioned at a station along the missile body, the traverse mechanism moved the probe vertically and horizontally to take flow field pressure measurements.

Force and moment data were obtained using a 0.75-inch, steady-state, internally-mounted strain-gauge balance. This balance has an accuracy of about 0.1 percent. All forces and moments were recorded in the body-axis system with the origin at the balance center. The data were also resolved into the tunnel-axis system for ease of comparison at all roll angles. Figure 1 shows the positive force directions for the tunnel-axis system relative to the missile and traverse mechanism.

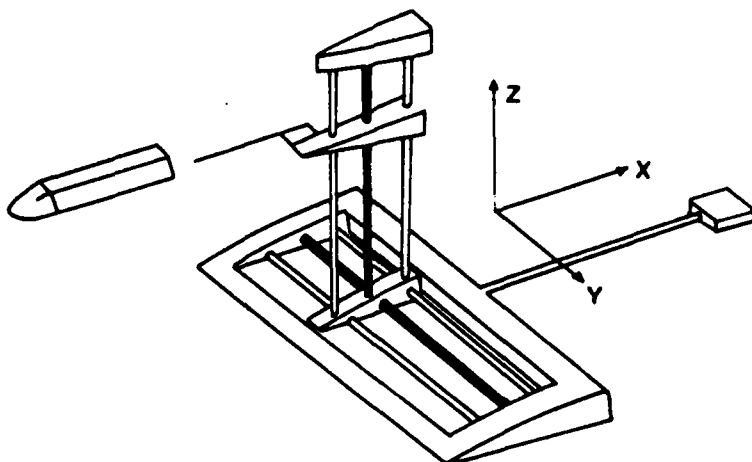


Figure 1. Positive Tunnel Axis Directions

**IV. Wind Tunnel Models**

Four wind tunnel models, having a typical missile fineness ratio equal to 7.5, were used for all of the tests except those for determining the effects of fineness ratio. Each model had a different body cross section (Figure 2).

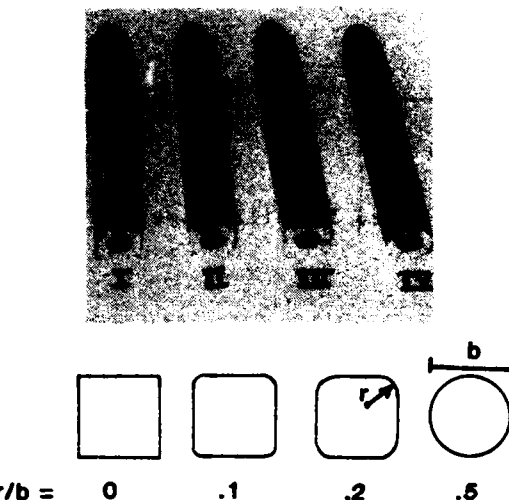


Figure 2. Low Fineness-Ratio Missile Shapes

The body cross sections ranged from square to round and were defined by a corner radius ratio ( $r/b$ ),  $r$  being the radius of the corners and  $b$  being the diameter of the circular missile. Each model was designed to satisfy wind tunnel constraints and therefore consisted of a 12-inch-long body section, which was attached to a 3-inch-long, blunted, tangent-ogive nose (Figure 3).

For the investigation of the aerodynamics of finned missiles, the same missile-body shapes were used, but a set of fins was attached to each missile body, as shown in Figure 3. These fins were 4 inches long at the base and 1.25 inches wide.

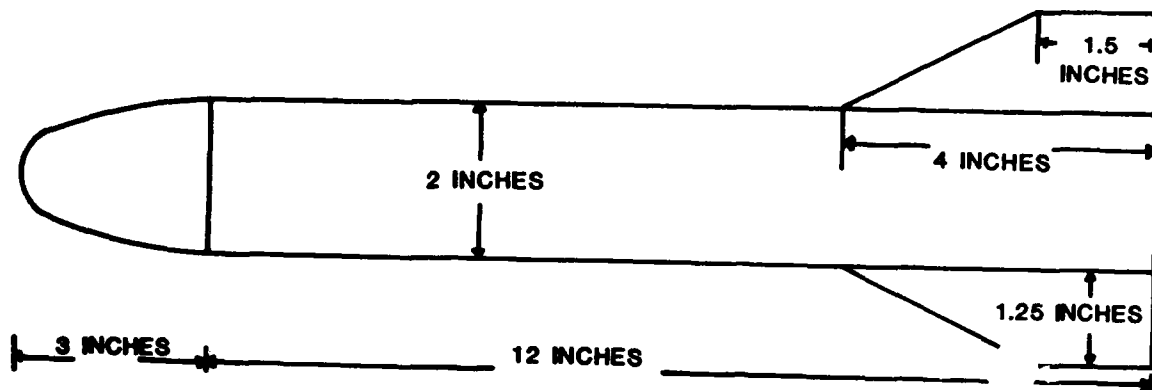


Figure 3. Finned Missile Dimensions

Five different missile bodies, having fineness ratios of 16 (approximately twice the fineness ratio of the original missiles), were used to determine the effects of fineness ratio. These missile shapes and their corner-radius ratios are shown in Figure 4.

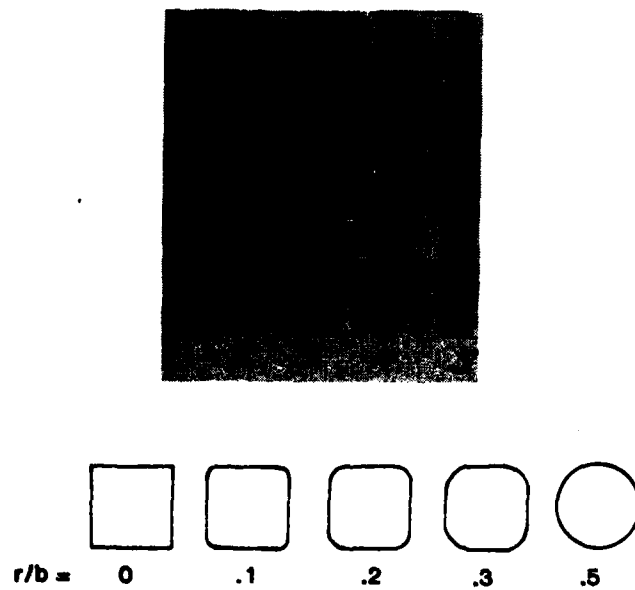


Figure 4. High Fineness-Ratio Missile Shapes

Four of the 5 missile body shapes had the same cross-sectional geometries as the original 4 missile shapes; an additional missile shape had an r/b of 0.3 to expand our data base further. Fineness-ratio effects were determined by comparing the aerodynamic test results obtained for the 2 different fineness-ratio missiles.

All missile bodies, noses, and fins were made from aluminum, with the center of the missile bodies being hollow for mounting purposes.

#### V. Measurement Techniques

The measurements taken in these tests may be grouped into 2 general categories: force and moment measurements and flow-field pressure measurements. Force and moment measurements were taken as described in the Test Apparatus section.

Flow-field pressure measurements were taken in measurement planes perpendicular to the axis of the tunnel. Each measurement plane was approximately 4.5 inches by 4.5 inches. Approximately 400 data measurements were taken at points spaced approximately 0.25 inches from each other in both x and y directions in the measurement plane.

The primary flow-field disturbance investigated was the vortex, since vortex positions and strengths affect aerodynamic forces and moments. To investigate vortices, the 2 components of velocity in the crossflow plane and the coefficient of total pressure were measured at each measurement point.

Velocity crossflow measurements were plotted as a series of vectors originating at the respective points in the measurement grid, the length of each velocity vector being proportional to the magnitude of the crossflow velocity at that point. These plots were useful in visualizing the vortices and their approximate locations. Figure 5 is a typical velocity crossflow plot, illustrating 2 vortices in the flow field.

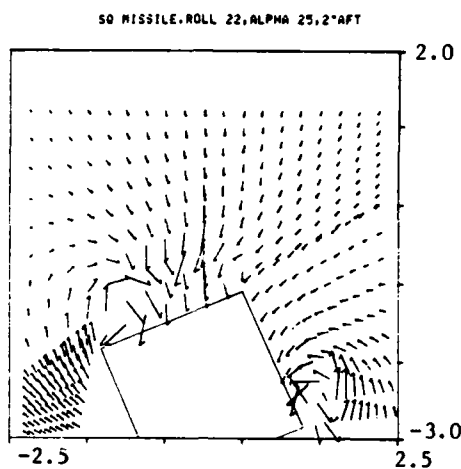


Figure 5. Typical Velocity Crossflow Plot, View Looking Downstream (Horizontal and Vertical Scales in Inches)

A nondimensional coefficient of total pressure,  $C_{Total}$ , was also measured at each grid point and was the primary parameter used to analyze the flow fields.  $C_{Total}$  is the difference between the local total pressure ( $P_{o_{Local}}$ ) at the measurement point and the tunnel's overall total pressure ( $P_{o_{Tunnel}}$ ), nondimensionalized by the tunnel's dynamic pressure ( $P_{o_{Tunnel}} - P_{\infty_{Tunnel}}$ ), where  $P_{\infty_{Tunnel}}$  is the tunnel static pressure:

$$C_{Total} = \frac{P_{o_{Local}} - P_{o_{Tunnel}}}{P_{o_{Tunnel}} - P_{\infty_{Tunnel}}} \quad (1)$$

Basically,  $C_{Total}$  is nothing more than a nondimensional number that gives an indication of what the total pressure is at some point in the flow. Because  $P_{o_{Tunnel}}$  is always greater than  $P_{o_{Local}}$  in the flow,  $C_{Total}$  will always be negative.  $C_{Total}$  is related to vortex strength, since a stronger vortex causes more viscous losses, resulting in a lower (more negative)  $C_{Total}$ . Because a vortex is strongest at its center,  $C_{Total}$  will be most negative near the vortex center. Thus, by comparing  $C_{Total}$  measurements for various missile configurations, one can determine which

configurations have stronger vortices and how the positions of these vortices change relative to the missile body.

#### VI. Test Results

Using the measurement techniques described in Section V, 4 sets of tests were conducted. These tests investigated first, the flow field along the axial length of the missile; second, how the flow field plane (arbitrarily set 2/3's back from the nose along the missile body) was affected by roll angle and corner radius; third, how the addition of fins to the square bodies affected the flow field; and fourth, how a change in fineness ratio affected the flow field.

##### A. Axial Length Effects

To determine how the flow field varied along the axial length of the missile, the square missile (I) without fins (Figure 2) was used. Measurements were taken and plotted looking downstream in various planes behind the nose of the missile, which was arbitrarily oriented at an asymmetric roll angle of 22.5 degrees and an angle of attack of 25 degrees.

Figure 6 illustrates the variation of flow field data with axial length for the square missile. Velocity crossflow plots are shown on the leeward side of the missile at 0, 6, 8, and 10 inches behind the nose-body junction. In Figure 6a, left and right vortices are shown to form at the nose-body junction. Figure 6b, which shows the velocity-crossflow plot at 6 inches behind the nose-body junction, indicates that both vortices are in the proximity of the missile body. By 8 inches aft (Figure 6c), the left vortex is shown to move farther away from the body. At ten inches aft (Figure 6d), the left vortex is even farther away from the missile body, while the right vortex still remains in the proximity of the body.

Thus, Figures 6a-d illustrate that after the vortices are formed near the nose-body junction of the missile, the left vortex moves away from the missile body, while the right vortex tends to remain near the body the entire length of the missile.

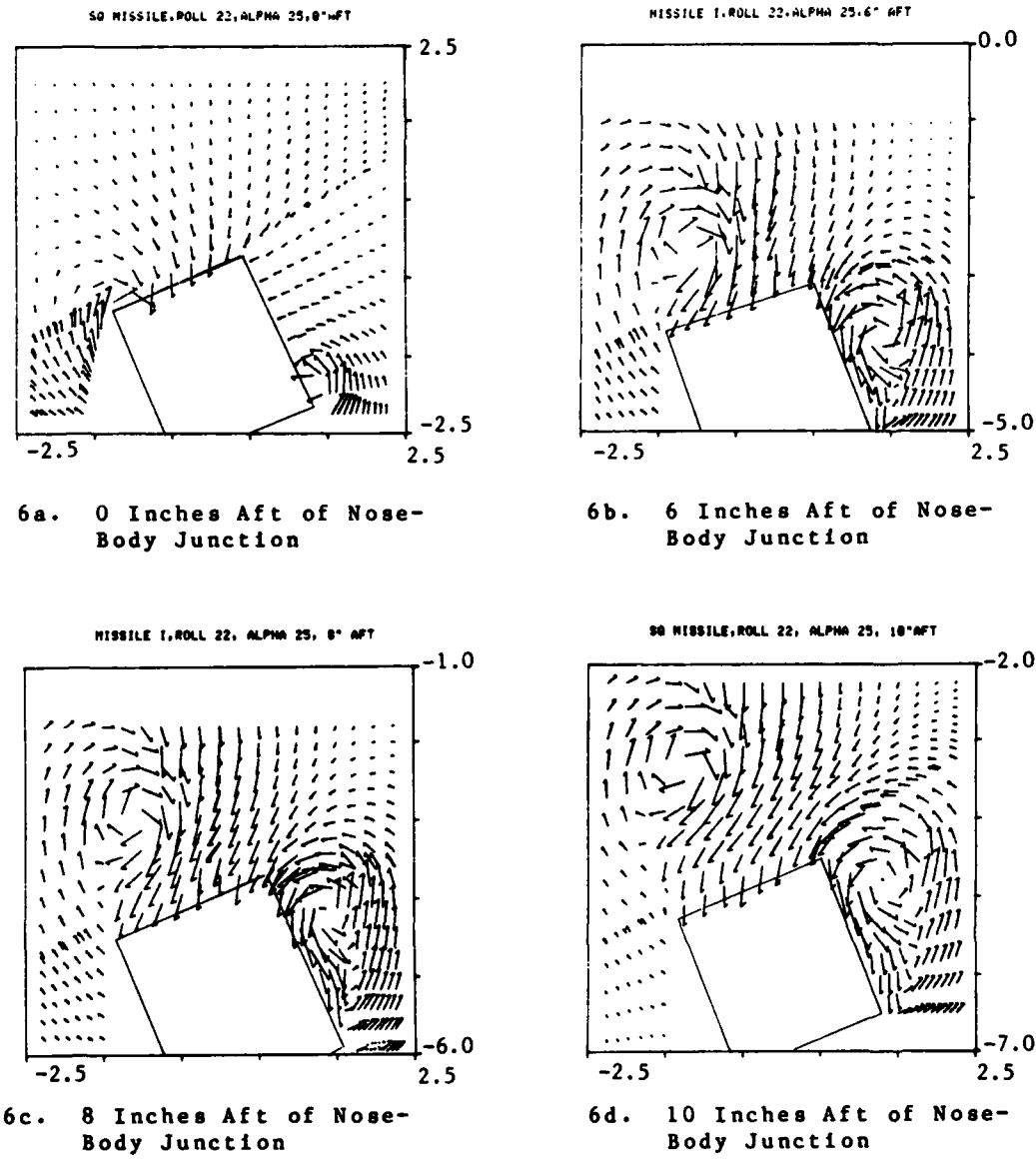


**Figure 6. Square Missile Velocity Crossflow, 25 Degrees Angle of Attack, 22 Degrees Roll, View Looking Downstream (Horizontal and Vertical Scales in Inches)**

Figure 7 shows the total pressure contours along the missile length. Vortices are apparent in Figure 7, and their relative strengths can be determined by the magnitude of total pressure at their centers. As shown in Figures 7a-d, the right vortex remains fairly constant in strength throughout the missile length, as indicated by the values of total pressure. The right vortex does, however, move up along the width of the missile, as illustrated in Figures 7a-d. The left vortex has not even formed at the nose-body junction (Figure 7a), indicating that it forms somewhere between 0 and 2 inches behind the nose (Figures 7a and b). It then gains strength to 6 inches (Figure 7c), and then remains fairly constant to the aft end of the missile (Figure 7d).

Figure 8 shows surface oil photographs taken in past experiments for the test conditions described in Figures 6 and 7, except that a higher tunnel velocity of 360 ft/sec was used (Ref. 6). These oil-flow pictures substantiate the test results shown in Figures 6 and 7, indicating how vortex position changes along the axial length of the missile. For instance, Figure 8a shows a top view of the upper left side of the missile (looking downstream). A line due to the vortex appears at the nose of the missile in the same relative position as that of the vortex shown in Figure 6a. This line diminishes in sharpness as it extends down the missile length, indicating that the vortex moves farther away from the missile body. This conclusion was demonstrated in Figures 6a-d. Figure 8b, which portrays the right side of the missile (looking downstream), also agrees with the pressure contours shown in Figure 7a-d. This figure shows that a vortex line starts at the lower part of the nose and travels the length of the missile while moving across its width. An identical observation was made from Figure 7. The results of this oil flow agree with the crossflow-velocity plots and total-pressure measurements, confirming a general pattern of vortex development.

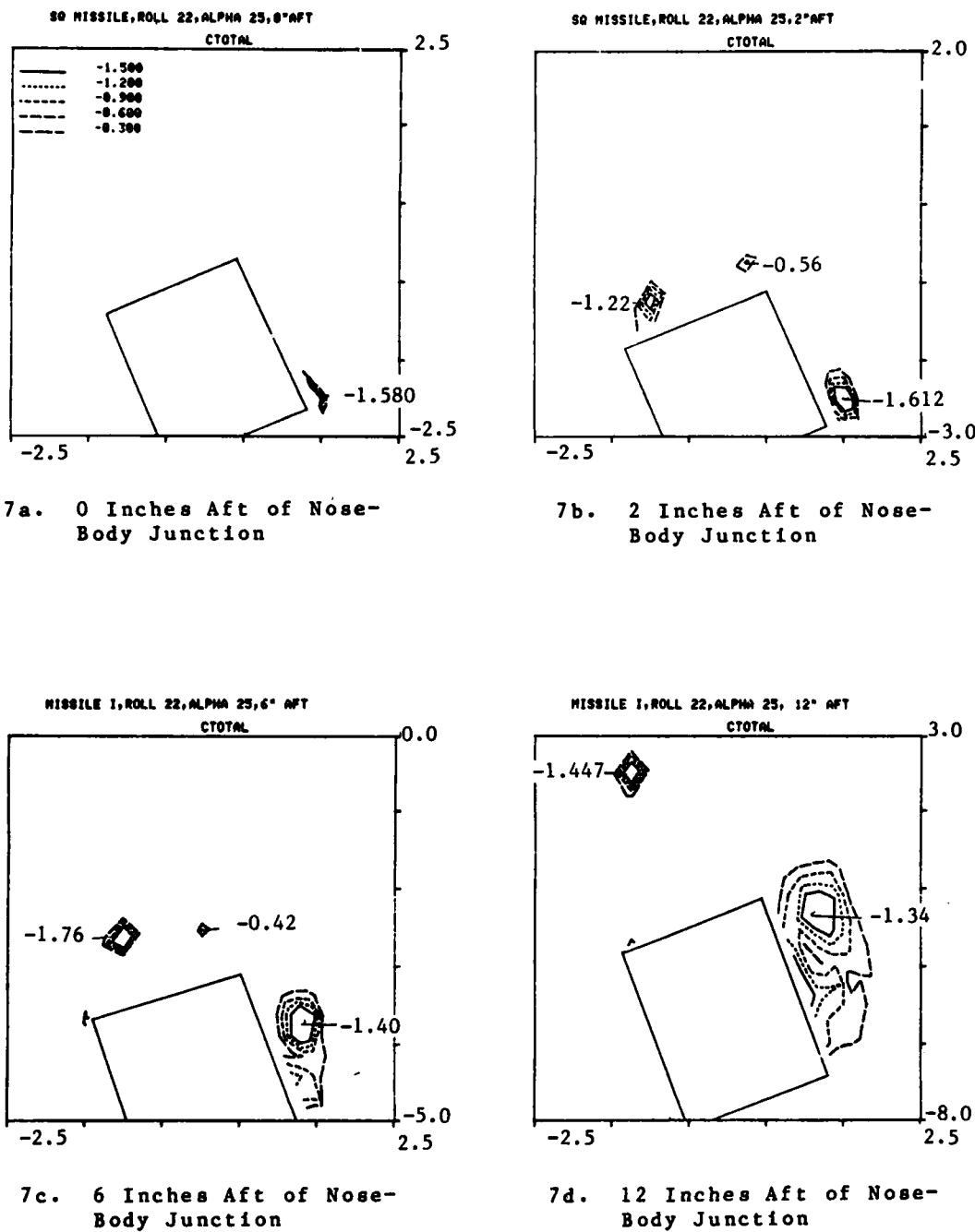
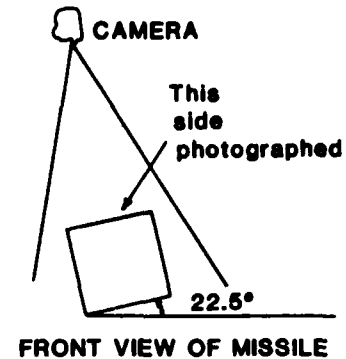


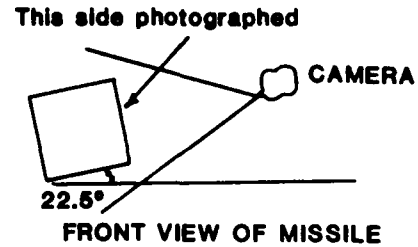
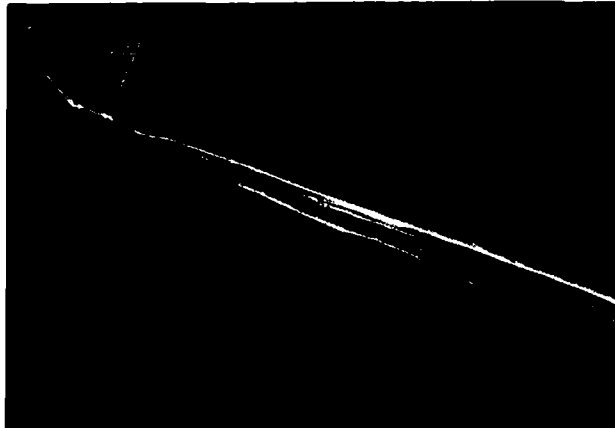
Figure 7. Square Missile C<sub>TOTAL</sub> Contours, 25 Degrees Angle of Attack, 22 Degrees Roll, View Looking Downstream (Horizontal and Vertical Scales in Inches)

A



8a. Top Left Side View (When Looking Downstream)

B



8b. Right Side View (When Looking Downstream)

Figure 8. Square Missile Oil Flow Photographs, 25 Degrees Angle of Attack, 22 Degrees Roll

### B. Roll Angle and Corner Radius Effects

In order to determine the effects of roll angle and corner radius on the flow field, pressure measurements were taken in the flow field at a plane other than the aft plane, as previously illustrated by Lijewski, et al. (Ref. 8). Tests were performed on the 3 noncircular missiles without fins (Figure 2). All 3 missile bodies were tested at 5 roll angles and 25 degrees angle of attack. The measurement plane was set 2/3's of the way back from the missile nose, and data were plotted in the flow-field plane looking downstream.

#### 1. Roll Angle Effects

As in previous Air Force Academy tests, roll angle affected the missile's flow field in a specific way. Figure 9a illustrates total pressure contours for the square missile at the symmetrical 0-degrees-roll configuration and shows that, as expected, essentially equal and symmetrical vortices were present. As the missile was rolled to the asymmetric 11- and 22.5-degree configurations (Figures 9b and c), the left vortex became stronger, while the right vortex retained about the same strength (as shown by the values of total-pressure coefficients) but moved lower along the right side of the body. In the 33-degree-roll configuration (Figure 9d), the right vortex became slightly stronger, while the left vortex remained approximately the same as in the 22.5-degree-roll configuration. Finally, in the symmetrical 45-degree-roll configuration (Figure 9e), the left and right vortices became equal and symmetrical again. These results agree with previous USAF Academy tests taken in a plane aft of the missile (Ref. 8) and add new data for the 11- and 33-degree-roll configurations.

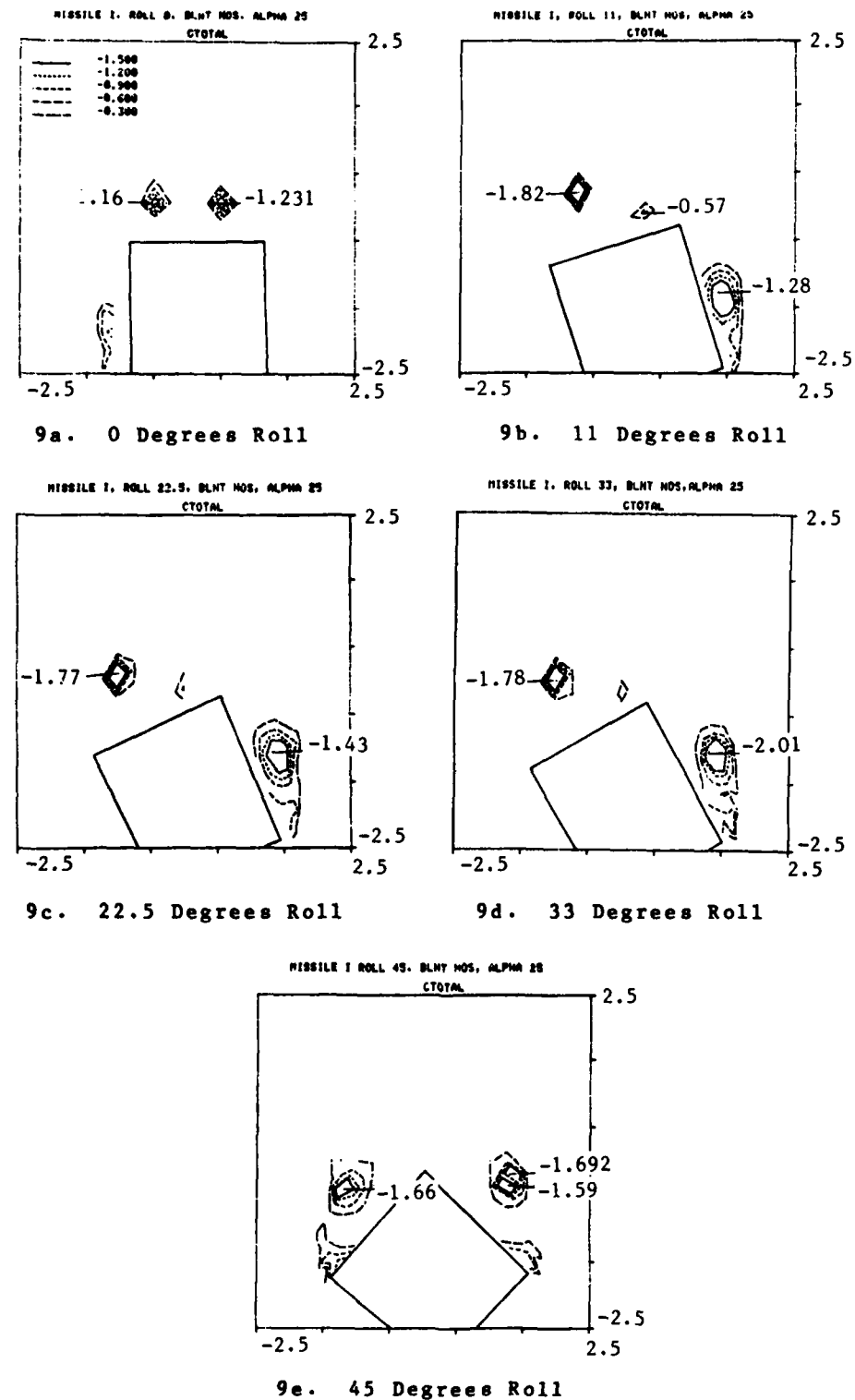


Figure 9. Square Missile CTotal Contours, 25 Degrees Angle of of Attack, Data Plane 2/3 Behind Nose, View Looking Downstream (Horizontal and Vertical Scales in Inches)

## 2. Corner Radius Effects

Corner radius also affected the flow field. As the corner radius ratio ( $r/b$ ) of the missile was varied from 0 (the square missile) to corner-radius ratios of 10 percent and 20 percent, significant differences in flow fields were observed for both symmetrical- and asymmetrical-roll configuration. Figure 10 shows the total pressure contours for the symmetrical 0-degree-roll configuration. As the cross-section shape of the missile is changed from square (Figure 10a) to more rounded (20 percent corner-radius ratio, Figure 10c), the vortices along the missile move slightly closer to the body. The vortices also tend to lose strength as corner-radius ratio increases from the square missile (Figure 10a) to the 20 percent corner-radius ratio missile (Figure 10c).

Figure 11 represents the asymmetric 33-degree-roll configuration. Again, vortices tend to stay closer to the missile body and to lose strength as corner radius increases from that of the square missile (Figure 11a) to that of the 20-percent, corner-radius missile (Figure 11c).

## C. Fin Effects

Tests were also conducted on the 4 previously used missiles with fins added (Figure 2) to determine how the fins affected forces and moments, and the flow field. Force and moment data were taken for 5 roll angles at various angles of attack. The flow field was analyzed by measuring pressures in a flow-field plane at the aft end of the missile. Missiles were tested at roll angles of 0, 22, and 45 degrees and an angle of attack of 25 degrees.

Figure 12 shows the force and moment coefficients for the finned and unfinned missiles plotted against corner radius ( $r/b$ ) for the symmetric

roll angle of 0 degrees and 25 degrees angle of attack. Figure 12a shows the lift coefficients ( $C_L$ 's) for the finned and unfinned missiles. Clearly, the finned missiles have greater lift due to the fins. Increasing the corner radius decreased the lift of the finned missiles in a nonlinear way by about the same amount that it decreased the lift of the unfinned missiles.

Figure 12b shows the drag coefficients ( $C_D$ 's) for the 4 missiles with and without fins. Because of the addition of fins, the drag for the finned missiles increased by a nearly constant amount over that for the unfinned missiles. The corner radius affected the finned missiles in the same manner as it did the unfinned missiles: drag decreased as corner radius increased.

Figure 12c shows the side-force coefficients ( $C_y$ 's) for the finned and unfinned missiles. As would be expected for a symmetric-roll condition, the side-force coefficient is relatively small for both the finned and unfinned missiles tested. The addition of fins slightly increases the magnitude of the side forces, as shown in the figure. In both cases side force decreases slightly with increasing corner radius.

Figure 12d shows the pitching-moment coefficients ( $C_M$ 's) for the missiles with and without fins. Pitching moment decreased significantly for the finned missiles as compared to the unfinned missiles, since the fins acted as small wings and generated strong negative pitching moments at positive angles of attack. As shown in the figure, pitching moment decreased with increasing corner radius in about the same manner for both the finned and unfinned missiles.

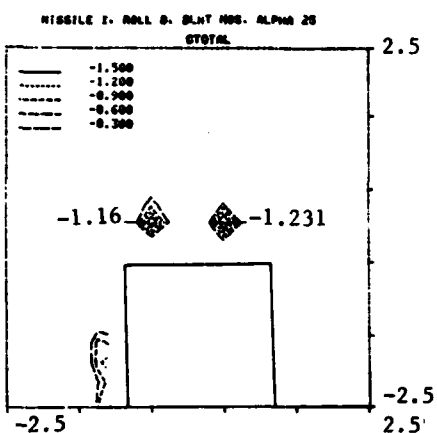
Figure 13 shows the force and moment coefficients for the square missile with and without fins at 0 degrees of roll and various angles of attack. Figures 13a and b show the lift and drag coefficients, respectively. Lift and drag show the same pattern of variation for

missiles without fins as for those with fins. In each case, the finned missiles had higher force-coefficient values at all angles of attack, and the difference in force coefficients between the finned and unfinned missiles became greater with increasing angle of attack. This pattern is caused by the fins themselves, which provide additional lift and drag forces.

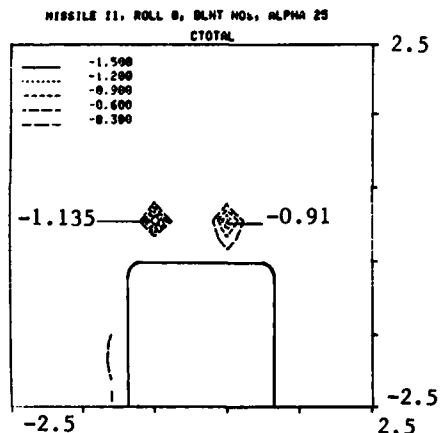
Figure 13c illustrates the side force coefficient ( $C_y$ ) variation with angle of attack for the finned and unfinned square missile. As observed previously, the magnitude of side force is relatively small, and in both cases the side force rises slightly with an increasing angle of attack. But the finned missile does not have a significantly higher side force than the unfinned missile.

Figure 13d shows the variation of the pitching moment with the angle of attack for the finned and unfinned square missiles. Pitching moment for the unfinned missile is positive and increases with increasing angle of attack, while for the finned missile it is negative and decreases with increasing angle of attack. These test results indicate that the addition of fins stabilizes the missile body, as would be expected.

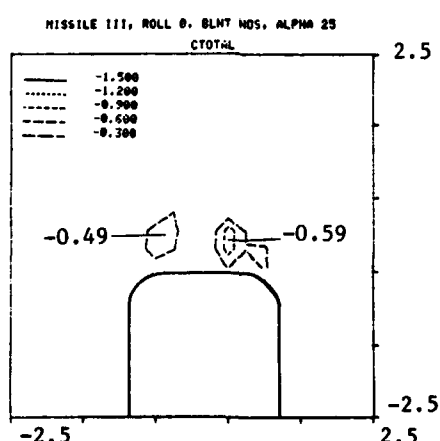
Figures 14 and 15 show the total-pressure contours taken at the aft end of a finned and unfinned square missile at 45 degrees of roll and 25 degrees angle of attack. The pressure contour data was plotted looking downstream. The finned missile (Figure 14) has 2 additional vortices located near the fintips that the unfinned missile does not have. These additional vortices come off the tips of the fins and are the only significant differences between the flow fields of the finned and unfinned missiles. These additional vortices contribute to some of the differences observed in the forces and moments between the finned and unfinned missiles in Figures 12 and 13.



10a. Square Missile

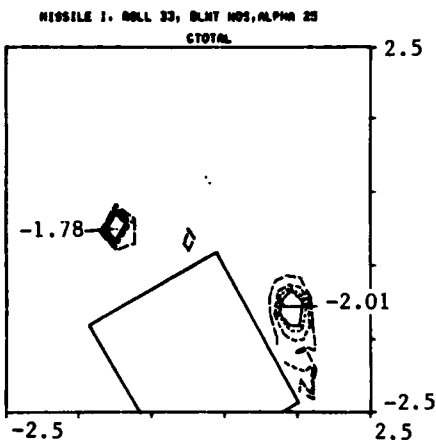


10b. 10 Percent Corner Radius Missile

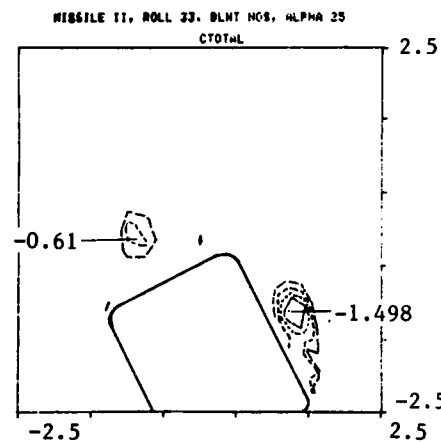


10c. 20 Percent Corner Radius Missile

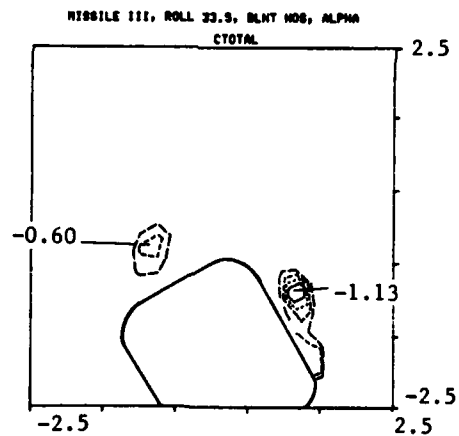
Figure 10. C<sub>TOTAL</sub> Contours, 25 Degrees Angle of Attack, 0 Degrees Roll, View Looking Downstream (Horizontal and Vertical Scales in Inches)



11a. Square Missile



11b. 10 Percent Corner Radius Missile



11c. 20 Percent Corner Radius Missile

Figure 11. C<sub>TOTAL</sub> Contours, 25 Degrees Angle of Attack, 33 Degrees Roll, View Looking Downstream (Horizontal and Vertical Scales in Inches)

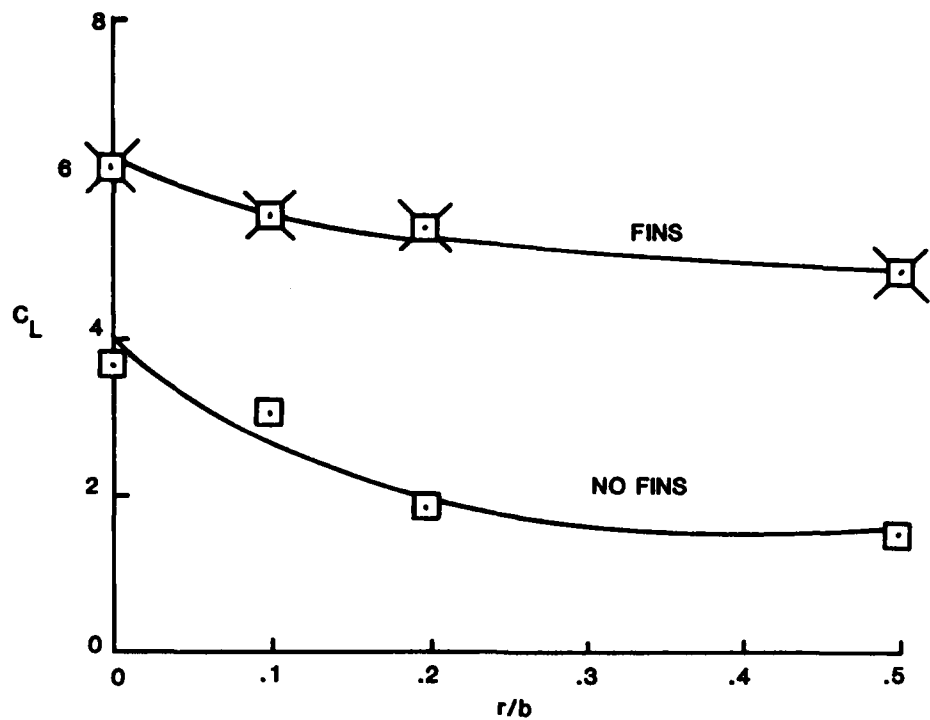
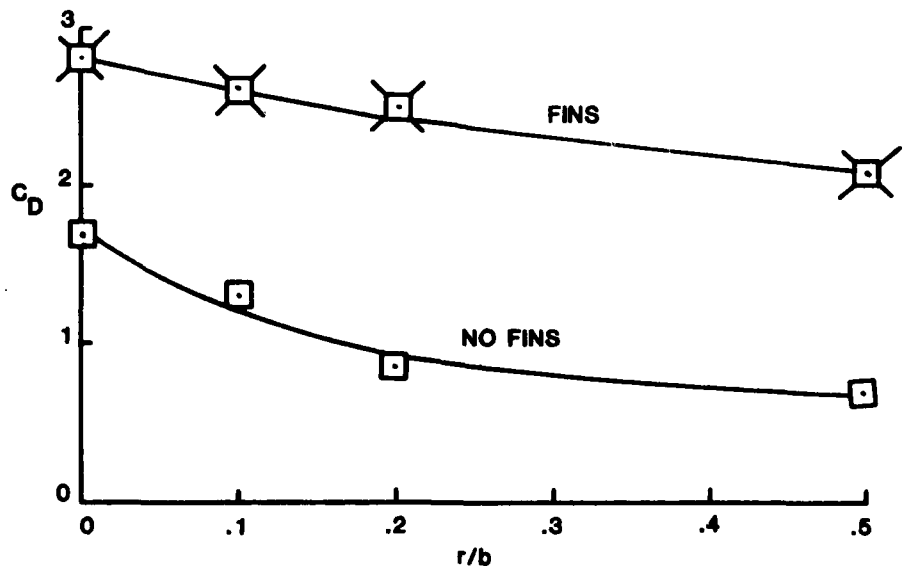
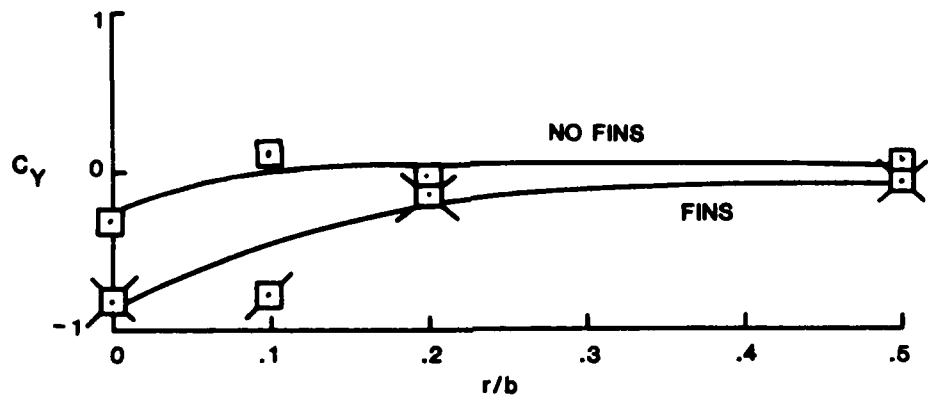
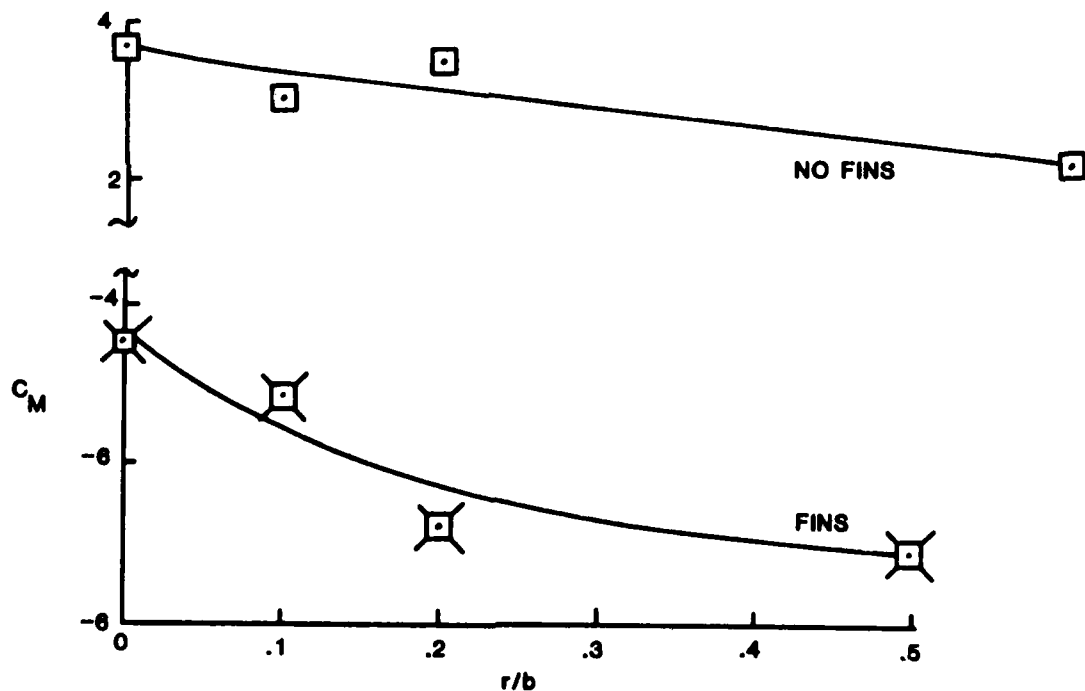
12a. Lift Coefficient ( $C_L$ ) versus Corner Radius ( $r/b$ )12b. Drag Coefficient ( $C_D$ ) versus Corner Radius ( $r/b$ )

Figure 12. Force and Moment Coefficients versus Corner Radius,  
25 Degrees Angle of Attack, 0 Degrees Roll



12c. Side Force Coefficient ( $C_y$ ) versus Corner Radius ( $r/b$ )



12d. Pitching Moment Coefficient ( $C_M$ ) versus Corner Radius ( $r/b$ )

Figure 12. Force and Moment Coefficients versus Corner Radius,  
25 Degrees Angle of Attack, 0 Degrees Roll

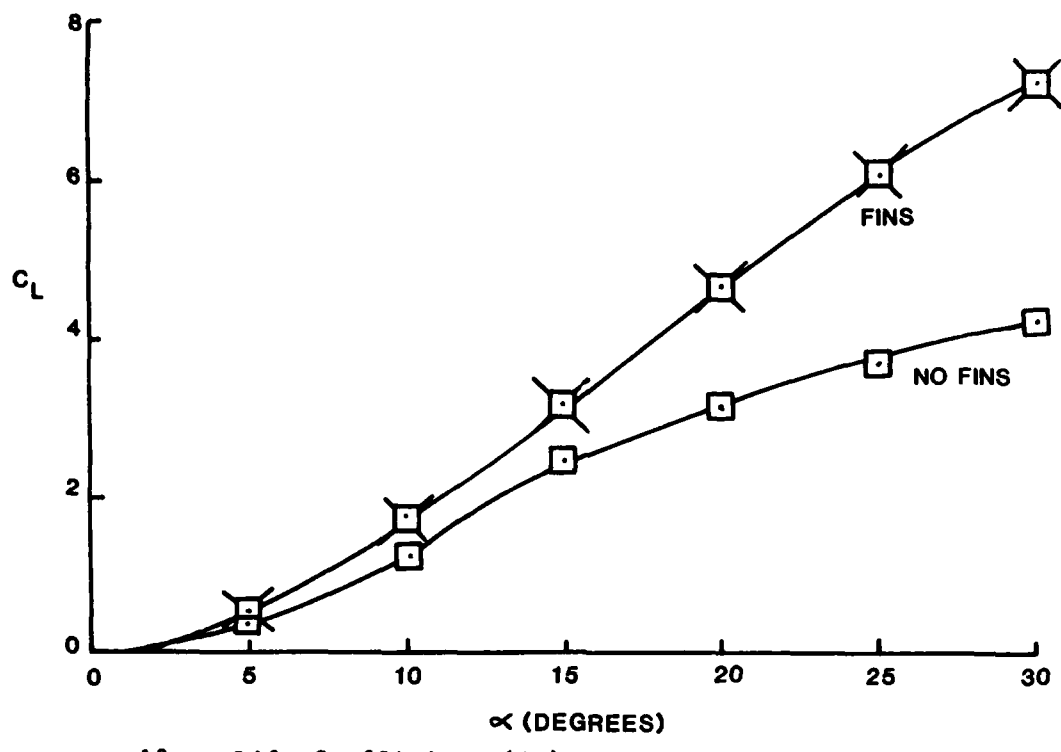
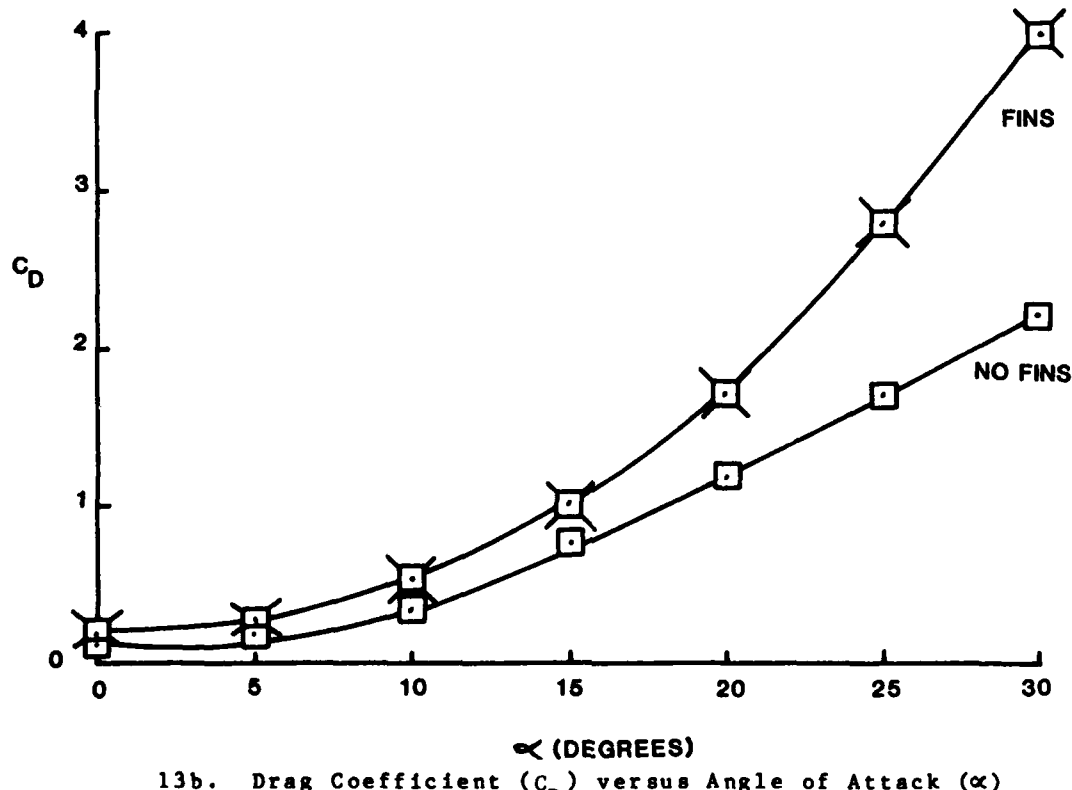
13a. Lift Coefficient ( $C_L$ ) versus Angle of Attack ( $\alpha$ )13b. Drag Coefficient ( $C_D$ ) versus Angle of Attack ( $\alpha$ )

Figure 13. Square Missile Force and Moment Coefficient versus Corner Radius, 25 Degrees Angle of Attack, 0 Degrees Roll

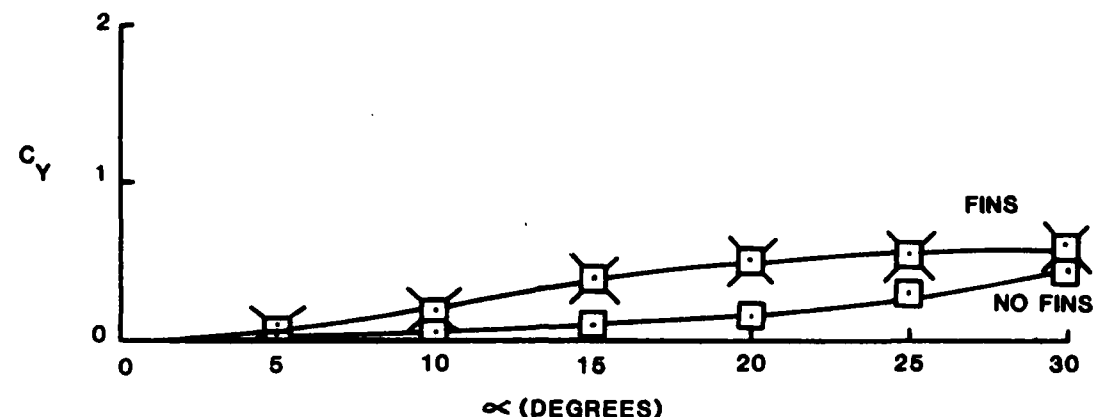
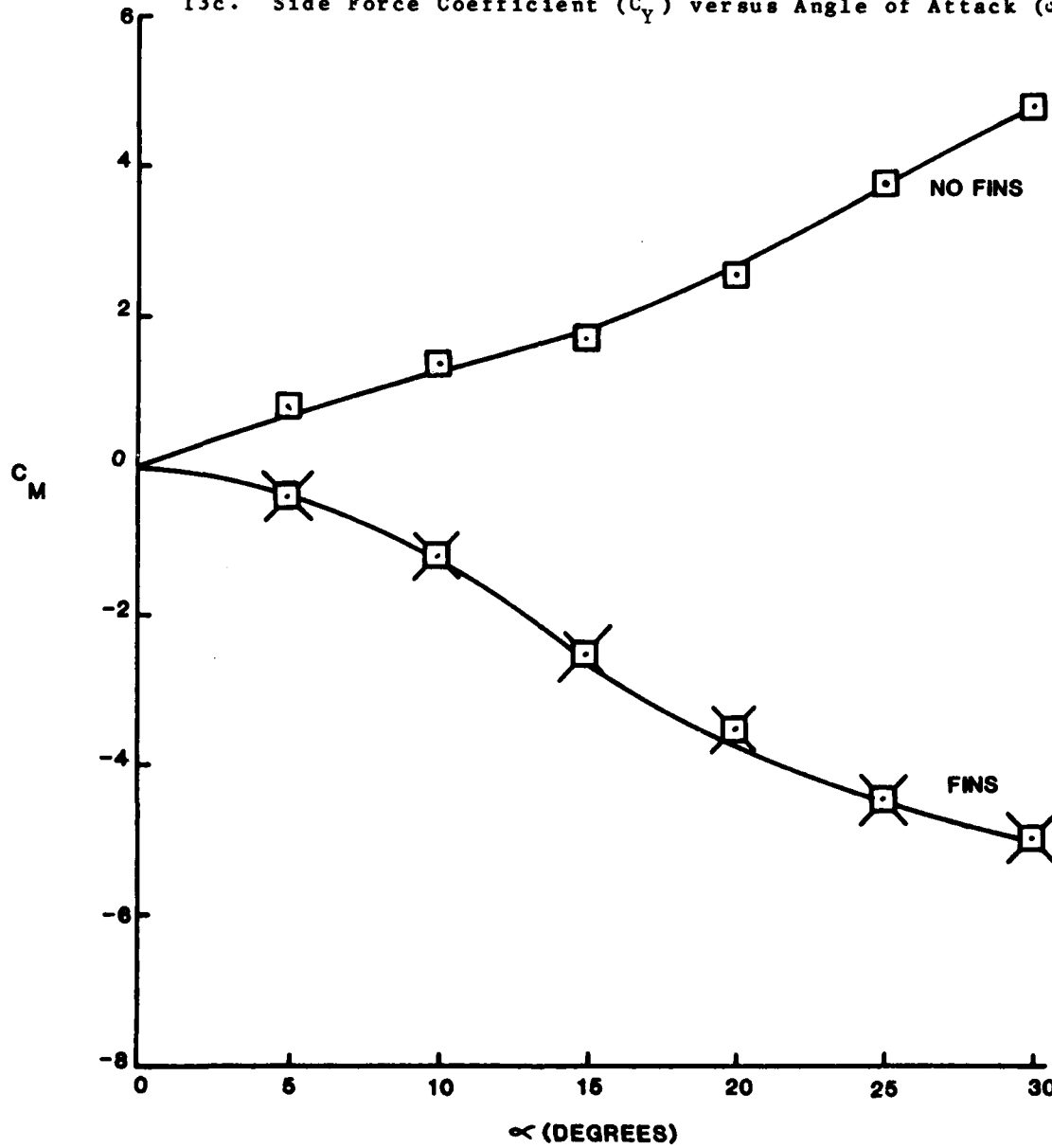
13c. Side Force Coefficient ( $C_Y$ ) versus Angle of Attack ( $\alpha$ )13d. Pitching Moment Coefficient ( $C_M$ ) versus Angle of Attack ( $\alpha$ )

Figure 13. Square Missile Force and Moment Coefficient versus Corner Radius, 25 Degrees Angle of Attack, 0 Degrees Roll

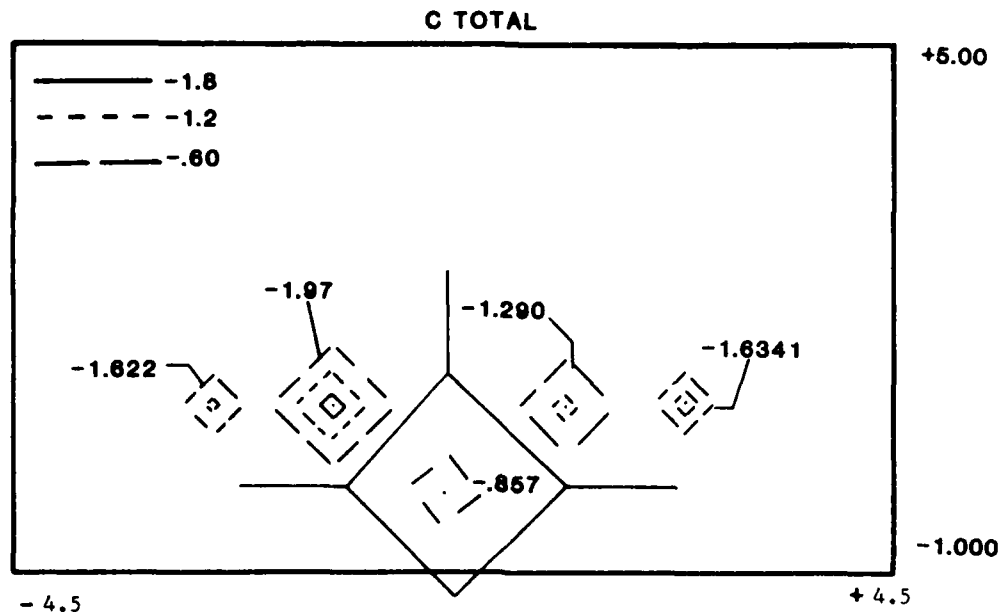


Figure 14. Finned Square Missile Total Pressure Contours, 25 Degrees Angle of Attack, 45 Degrees Roll, Aft Plane, View Looking Downstream

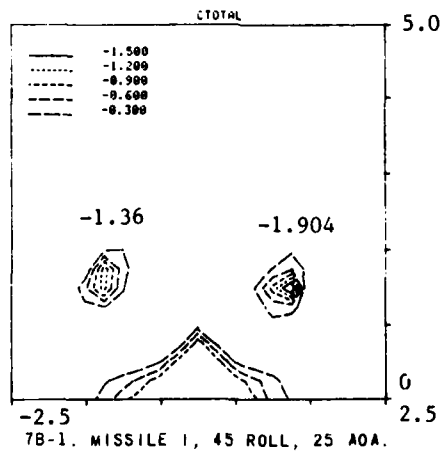


Figure 15. Unfinned Square Missile Total Pressure Contours, 25 Degrees Angle of Attack, 45 Degrees Roll, Aft Plane, View Looking Downstream (Horizontal and Vertical Scales in Inches)

#### D. Fineness Ratio Effects

The effects of fineness ratio (the ratio of missile length to width) were investigated by testing a set of 5 unfinned missiles (Figure 4) with a fineness ratio of approximately 16 and comparing test results with data obtained for missiles with a fineness ratio of 7.5. Flow-field data for these high fineness-ratio missiles were taken in a measurement plane at the aft end of the missile and plotted looking upstream for 5 roll angles at 30 degrees angle of attack. Since previous flow-field data for the low fineness-ratio missiles were plotted looking downstream, this new set of data must be reversed for the purpose of comparison.

Corner radius appeared to affect the flow field of the high fineness-ratio missiles (16) in the same manner as it did that of the low fineness-ratio missiles (7.5) previously analyzed. Figure 16 shows the total pressure contours for the 5 high-fineness-ratio missiles at 0 degrees of roll and 30 degrees angle of attack. As the corner-radius ratio increased from 0 (the square missile, Figure 16a) to 0.5 (the round missile, Figure 16e), the strength of both the left and right vortices decreased. This trend was also observed for the lower fineness-ratio missiles, as shown in Figure 17.

Changes in roll angle were also observed to have the same effect on the flow fields of both the higher and lower fineness-ratio missiles. Figure 18 illustrates the effect of roll angle on the flow field by showing total pressure contours for the 20-percent corner-radius missile at 5 roll angles and 30 degrees angle of attack. As with the lower fineness-ratio missiles, symmetrical vortices formed at symmetrical roll angles (Figures 18a and 18e), and asymmetrical vortices formed at asymmetrical roll angles (Figures 18b, c, and d).

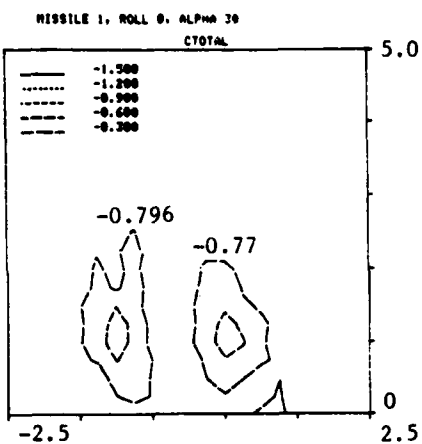
Apparently there are no conclusive differences between the flow fields around the higher and the lower fineness-ratio missiles. At

0-degrees roll the vortices around the higher fineness-ratio missiles in Figure 16 tend to be slightly weaker than those around the lower fineness-ratio missiles in Figure 17. However, when comparing the flow fields around the 20 percent corner radius missiles, the vortices around the higher fineness-ratio missiles (Figure 18) are slightly stronger than those around the lower fineness-ratio missiles (Figure 19).

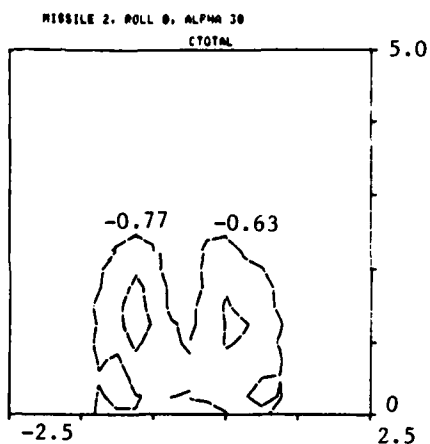
Quantitative comparisons of vortex strengths and locations between the 2 fineness-ratio missiles are difficult to make for 3 reasons. First, the higher fineness-ratio missiles were tested at a higher angle of attack (30 degrees versus 25 degrees for the lower fineness-ratio missiles). Second, the higher fineness-ratio missiles had a smaller width (1.5 inches versus 2 inches for the lower fineness-ratio missiles). Finally, although flow-field pressure measurements were taken at the aft end of both missiles, the high fineness-ratio missile was 8 inches longer than the lower fineness-ratio missile; consequently, the measurement plane was approximately 7 inches farther downstream from vortex initiation. Certainly, each of these factors will affect the quantitative characteristics of the flow field.

Although these differences create problems in comparing the flow fields of the 2 missiles quantitatively, the flow-field patterns can be compared qualitatively. The test results, as shown in Figures 16 through 19, illustrate that the flow field patterns for the 2 missiles are basically similar, indicating that the fineness ratio does not significantly affect flow-field patterns.

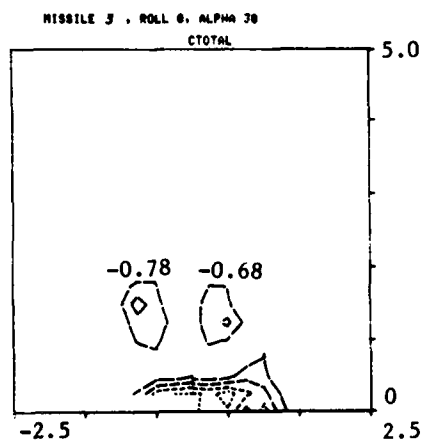
USAFA-TR-83-15



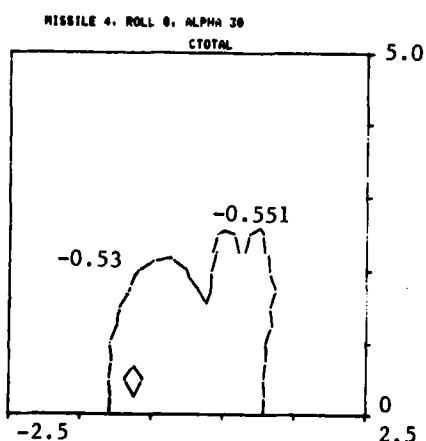
16a. Square Missile



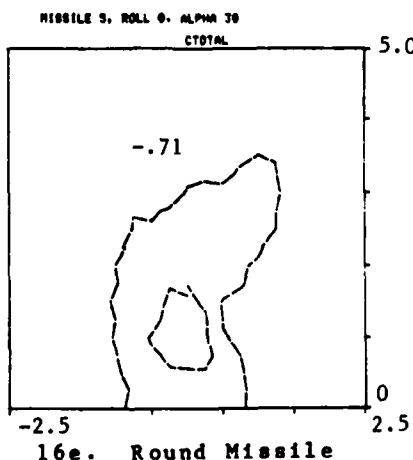
16b. 10 Percent Corner Radius Missile



16c. 20 Percent Corner Radius Missile

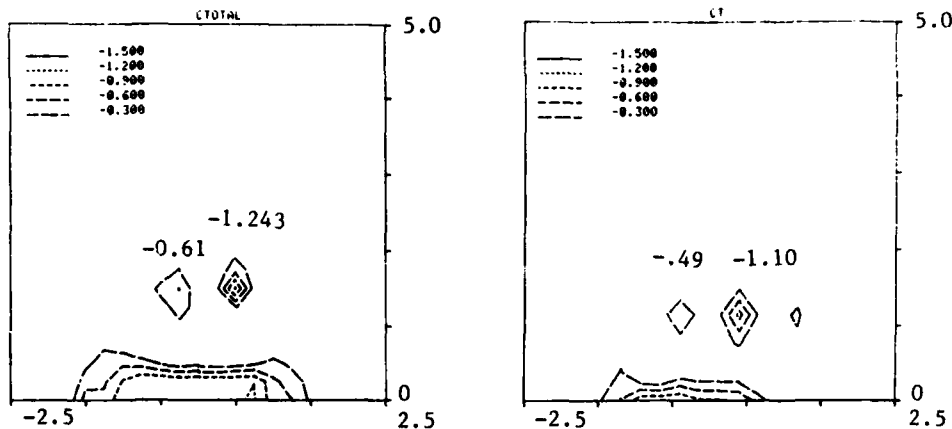


16d. 30 Percent Corner Radius Missile

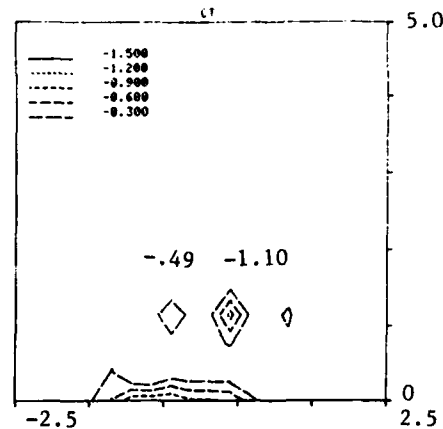


16e. Round Missile

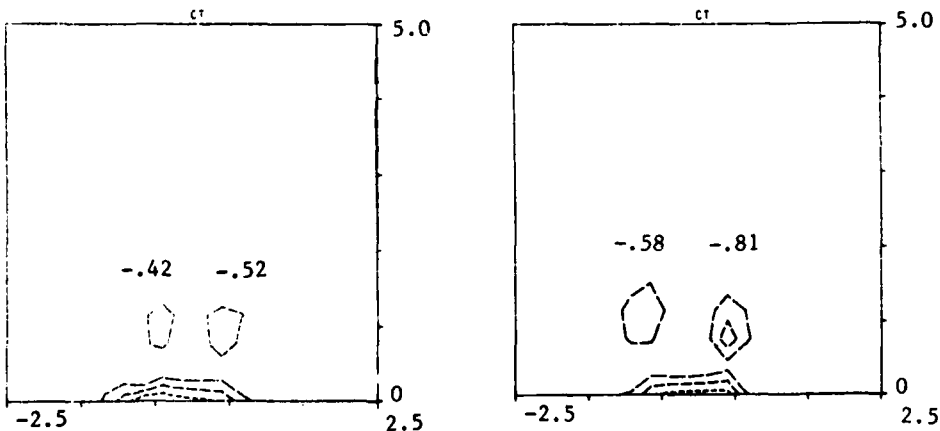
Figure 16. High Fineness-Ratio Missile Total Pressure Contours,  
30 Degrees Angle of Attack, 0 Degrees Roll, Aft  
Plane, View Looking Downstream (Horizontal and  
Vertical Scales in Inches)



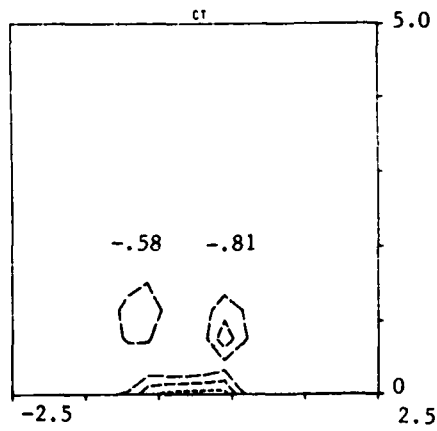
17a. Square Missile



17b. 10 Percent Corner Radius Missile



17c. 20 Percent Corner Radius Missile



17d. Round Missile

Figure 17. Low Fineness-Ratio Missile Total Pressure Contours,  
25 Degrees Angle of Attack, 0 Degrees Roll, Aft  
Plane, View Looking Downstream (Horizontal and  
Vertical Scales in Inches)

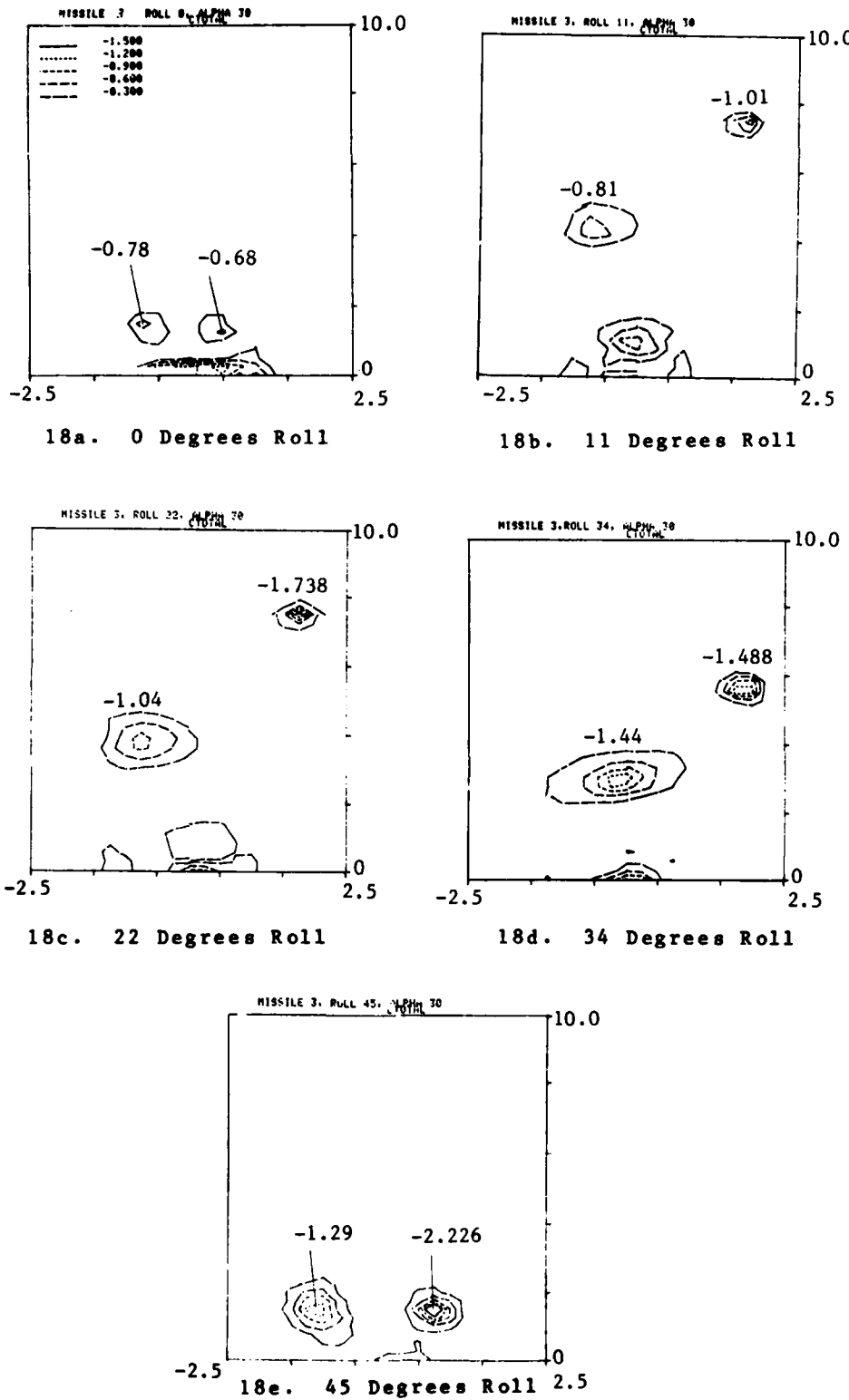
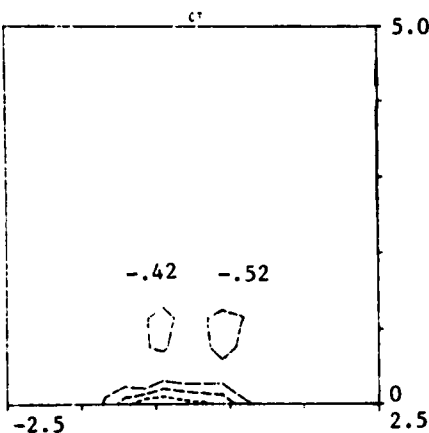
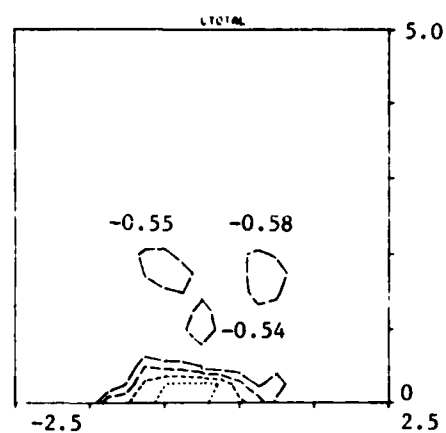


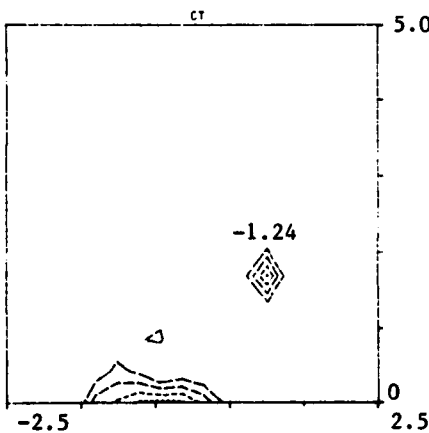
**Figure 18.** 20 Percent Corner Radius High Fineness-Ratio Missile Total Pressure Contours, 30 Degrees Angle of Attack, Aft Plane, View Looking Upstream (Horizontal and Vertical Scales in Inches)



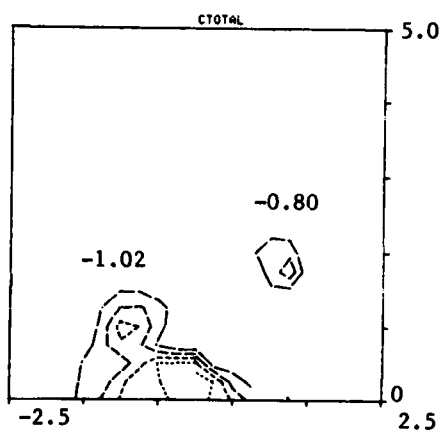
19a. 0 Degrees Roll



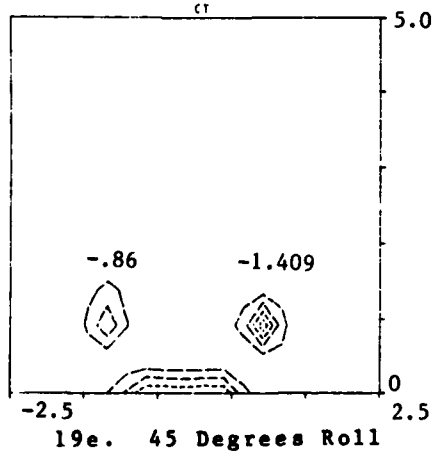
19b. 11 Degrees Roll



19c. 22 Degrees Roll



19d. 33 Degrees Roll



19e. 45 Degrees Roll

**Figure 19.** 20 Percent Corner Radius Low Fineness-Ratio Missile Total Pressure Contours, 25 Degrees Angle of Attack, Aft Plane, View Looking Upstream (Horizontal and Vertical Scales in Inches)

VII. Conclusions

In summary, 4 sets of tests have been conducted on square cross-section missiles. In the first set of tests (axial flow-field measurements), 2 vortices were observed along the missile body for the entire length of the missile. Quantitative pressure measurements taken along the body confirm the conclusions made from past qualitative oil-flow patterns observed on the missile bodies. The left vortex was shown to increase slightly in strength as it moved back along the missile body while at the same time moving away from the body. The right vortex formed with considerable strength, remained fairly constant, and stayed in the proximity of the missile body along the entire missile length.

In the second set of tests, flow-field measurements were taken at a plane 2/3's back from the nose to investigate roll-angle and corner-radius effects. As in previous USAF Academy tests (Ref. 8), roll angle was found to cause symmetrical-vortex patterns for symmetrical-roll configurations and asymmetric-vortex patterns for asymmetric-roll configurations. Also increasing corner radius was found to decrease vortex strength and keep the vortices closer to the missile body.

In the third set of tests, the addition of fins to the test models caused the lift and drag forces to increase and pitching moment to decrease. All forces increased progressively with increasing angle of attack, and the pitching moment grew more negative with increasing angle of attack. The addition of fins did not change the manner in which corner radius affected the forces and moments. Fins affected the flow field in that a vortex was generated near each fin tip.

The fourth set of tests indicated that the higher fineness-ratio missiles produced approximately the same flow field patterns as the lower fineness-ratio missiles.

In general, these 4 tests have been useful in supplementing existing

aerodynamic research on square missiles and adding to the square missile data base. Additional testing still needs to be conducted. Even more important, however, is the application of this basic research to the design of an operational square missile. Certainly the series of tests conducted in this basic research will aid missile designers in determining whether square missiles are feasible in the future.

References

1. Polhamus, E.C., E.W. Geller, and K.T. Grunwald. "Pressure and Force Characteristics of Noncircular Cylinders as Affected by Reynolds Number with a Method for Determining the Potential Flow about Arbitrary Shapes," NASA TR R-46, 1959.
2. Polhamus, E.C. "Effect of Flow Incidence and Reynolds Number on Low-Speed Aerodynamic Characteristics of Several Noncircular Cylinders with Applications to Directional Stability and Spinning," NASA TR R-29, 1959.
3. Clarkson, M.H., G.N. Malcolm, and G.T. Chapman. "A Subsonic, High Angle of Attack Flow Investigation at Several Reynolds Numbers," AIAA Journal, Vol. 16, Jan. 1978, pp. 53-60.
4. Knoche, H.G. and W. Schamel. "Aerodynamic Characteristics of Bodies with Rectangular Cross Section," AIAA Aerospace Sciences Meeting, January 1981, Paper No. 81-0145.
5. Schneider, W. "Experimental Investigation of Bodies with Non-Circular Cross Section in Compressible Flow," AGARD CPP 336, Missile Aerodynamics, September 1982, pp. 19-1 - 19-11.
6. Daniel, D.C., T.R. Yechout, and G.J. Zollars. "Experimental Aerodynamic Characteristics of Missiles with Square Cross Sections," Journal of Spacecraft and Rockets, Vol. 19, No. 2, March-April 1982, pp. 167-172.
7. Daniel, D.C., L.E. Lijewski, and G.J. Zollars. "Experimental

- Aerodynamic Studies of Missiles with Square Cross Sections," AGARD CPP 366, Missile Aerodynamics, September 1982, pp. 18-1 - 18-15.
8. Lijewski, L.E., G.J. Zollars, T.R. Yechout, and B.F. Haupt. "Experimental Flowfield Measurements of Missiles with Square Cross Sections," AIAA Aerospace Sciences Meeting, January 1982, Paper No. 82-0055.
9. "Subsonic and Trisonic Wind Tunnel Facilities." Department of Aeronautics, United States Air Force Academy.
10. Gerner, A. and G. Sisson. "Seven-Hole Probe Data Acquisition System," USAFA-TN-81-8, 18 November 1981.

**USAFA-TR-83-15**

**SECTION II**

**Instrumentation**

INVESTIGATION OF A STALL-ANTICIPATION  
DEVICE FOR AIRFOILS

Scott P. Goodwin\* and William A. Buzzell\*\*

Abstract

The subject of this paper is the testing of an experimental pressure and reverse-flow sensing device (a "shaped block") to discover if it could be used to anticipate the aerodynamic stall of an airfoil at low speeds and high angles of attack. The particular phenomenon investigated was the change in pressure that occurred when the flow in the airfoil boundary layer reversed direction. Analytical predictions of the boundary layer thickness revealed that a block 0.02 inches in height would be contained entirely in the boundary layer, allowing accurate measurements to be made. Testing was conducted at freestream Mach numbers of 0.1 and 0.2, with angles of attack varying in increments from -5 to +25 degrees. The shaped blocks detected reverse flow in the boundary layer and also anticipated stall of the airfoil at approximately 4 to 5 degrees of angle of attack less than the stall angle of 20 degrees.

I. Introduction

The phenomenon of stall has been of great concern to pilots, flight test engineers, and researchers since man began to fly. Various techniques for detecting the onset of stall (ranging from simple strings and reed-type devices to the sophisticated angle-of-attack vanes of today's modern fighter aircraft) have been used with varying degrees of success. Although these devices will not be discussed in detail, it is important to note that these sensors share 2 characteristics. First, each measures some condition of the airflow that may indicate the approach of stall. Second, all current stall-sensing devices operate by measuring a freestream condition such as angle of attack. The device discussed here, the shaped block, measures a flow condition but breaks with the tradition of stall sensors by measuring the flow conditions in the boundary layer. Since changes in the flow over the airfoil occur first in the boundary layer, this device is more sensitive in detecting an approaching stall than a freestream sensor is.

---

\*C1C USAF Academy

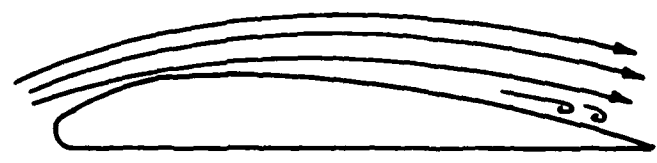
\*\*Captain, USAF, Assistant Professor of Aeronautics, DFAN

The purpose of the testing was to determine if the shaped block could anticipate the onset of stall of an airfoil at high angles of attack and low Mach numbers. To accomplish this purpose, 6 shaped blocks were mounted on a constant cross-section, 18-inch span, 6-inch chord NACA 0015 airfoil with end plates. The end plates served to eliminate tip effects and approximate an infinite wing. The model was then placed in the USAF Academy's 2-feet x 3-feet subsonic wind tunnel and tested at Mach numbers of 0.1 and 0.2. What follows is a brief discussion of the theory of stall, the operation of the shaped block, and the results of testing the blocks as stall-anticipating devices.

## II. Airfoil Stall

As an airfoil moves through the atmosphere at low angles of attack, the air, under normal conditions, flows smoothly around the object, and the flow remains attached to the body's surface (Figure 1a). As the angle of attack increases, the flow begins to separate from the airfoil near the trailing edge (Figure 1b). The separation point moves forward as the angle of attack increases. When the separation point reaches the leading edge, the airfoil stalls (Figure 1c). The separated flow moving across the upper surface of the airfoil has increased in pressure, since it is no longer accelerating around a streamlined object. Such acceleration normally causes the pressure on the upper surface to fall below that on the lower surface. This pressure difference is the source of lift. The rise in pressure (occurring as the separation point approaches the leading edge) results in a loss of lift as the pressures on the upper and lower surfaces equalize, causing the airfoil to stall.

Within the boundary layer on a cambered airfoil, the velocity profile (Figure 2) is influenced by an adverse pressure gradient that decreases the flow's momentum.



NORMAL FLOW

Figure 1a.



SEPARATED FLOW

Figure 1b.

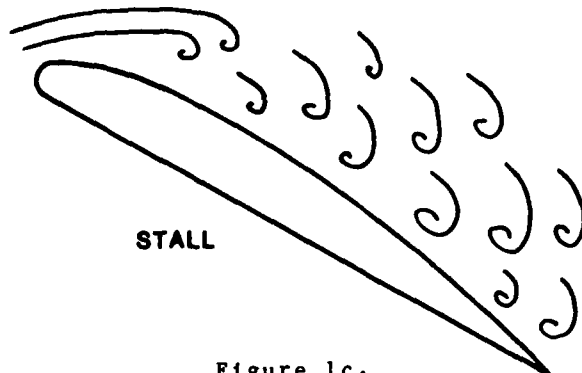


Figure 1c.

Figure 1. Airfoil Flow Series

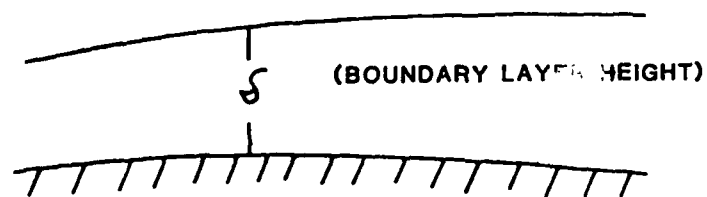


Figure 2. Typical Boundary Layer

Because of the pressure gradient, the airflow slows until a point is reached where the flow velocity near the surface is 0. This point, where  $(\partial u / \partial y)_{y=0} = 0$  (Ref. 1), is called the separation point. Downstream from the separation point the direction of flow in the boundary layer reverses. The shaped blocks, explained in more detail in the following section, measure this phenomenon.

### III. The Shaped Block

The shaped blocks used in this experiment were small aluminum equilateral triangles 0.2-inch on a side. The blocks were 0.020 inches in height, and holes 0.020 inches in diameter (bisecting each side) were drilled to act as pressure ports. Figure 3 provides a detailed drawing of the device. Aerodynamic and manufacturing considerations, as well as a boundary-layer analysis (presented later in this paper), were the deciding factors in choosing the blocks' size. Earlier work done at the USAF Academy, using shaped blocks to determine skin friction coefficients (Ref. 2), demonstrated that blocks smaller than those just described were not any more sensitive to boundary layer flow changes. In addition, this block size was convenient for machining purposes.

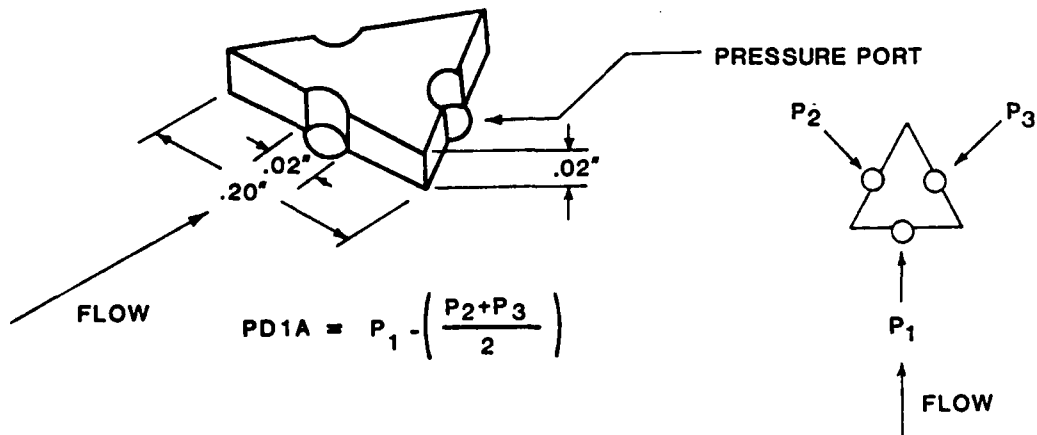


Figure 3. Shaped Block Detail

The shaped block senses pressure in much the same manner as a pitot-static system. Pressure Port 1 (see Figure 3 for the numbering system) faces into the flow. This port detects a quasi-total pressure slightly lower than the freestream total pressure yet equal to the sum of the static atmospheric pressure and the dynamic pressure resulting from the flow velocity impinging upon the block's face. But Ports 2 and 3 are screened from the flow and register only the static pressure. The pressures sensed at Ports 2 and 3 are averaged and then subtracted from the pressure at Port 1 to give the parameter called PDIA defined by the following equation:

$$PDIA = P_1 - \left( \frac{P_2 + P_3}{2} \right) \quad (1)$$

The values of PDIA for each velocity profile (Figure 4) are the key to the operation of the shaped block. At low angles of attack, the boundary-layer velocity profile is as shown in Figure 4b. Port 1 acts as a total-pressure source, while Ports 2 and 3 behave as static sources. In this condition, PDIA is greater than 0. But as the angle of attack increases, a separation point develops (Figure 4c). Because the local velocity at the shaped block is 0, pressures at Ports 1, 2, and 3 are equal, so PDIA will equal 0. Finally, as the flow reverses (Figure 4d), the roles of the pressure ports reverse. Ports 2 and 3 will now be total sources with a pressure greater than that at Port 1, which will be a static pressure. At this point PDIA is negative and indicates flow reversal or total separation and the onset of stall. The following table summarizes the shaped block's operation.

Table I  
PDIA SUMMARY

PDIA	Flow Indication
> 0 (+)	Normal, Attached Flow
= 0	Beginning of Separation
< 0 (-)	Reverse Flow

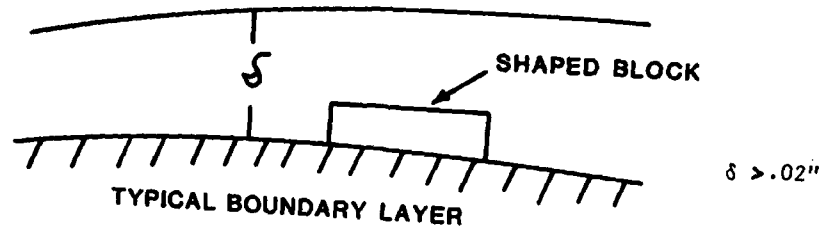


Figure 4a.

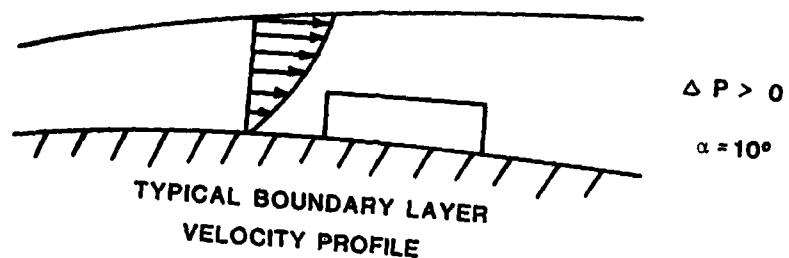


Figure 4b.

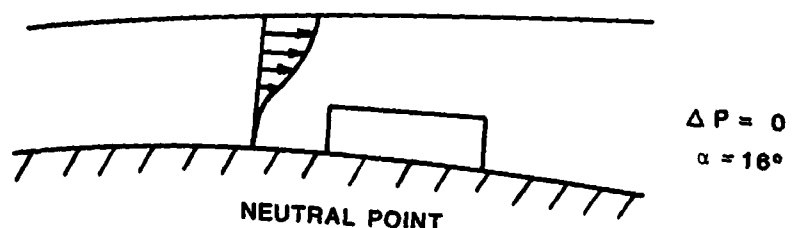


Figure 4c.

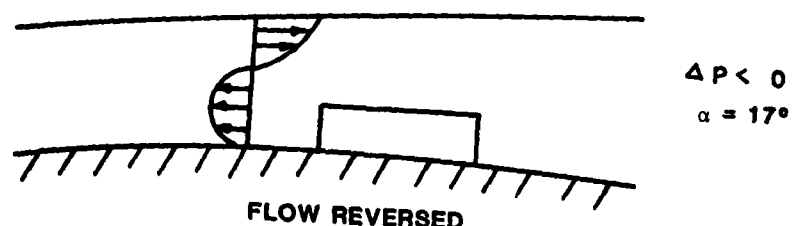


Figure 4d.

Figure 4. Boundary Layer Velocity Profiles

Before testing could begin, the shaped blocks had to be sized. Since flow reversal occurs in the boundary layer, the shaped-block height must not extend above the layer. When the boundary layer is laminar at higher velocities, it will be at its thinnest. Therefore, the thickness of the laminar boundary layer will determine the maximum size of the shaped block. The following equations were used to calculate and plot the boundary-layer thickness as a function of chord at standard day conditions, using a flat-plate approximation (Ref. 1).

$$Re_x = \frac{\rho_\infty V_\infty x}{\mu} \quad (2)$$

$$\delta_{Laminar} = \frac{5.2x}{\sqrt{Re_x}} \quad (3)$$

After running tests at the USAF Academy (Ref. 2), the results (Figure 5) indicated that a block 0.02 inches in height (if located aft of the point of maximum airfoil thickness) would be entirely contained by the boundary layer.

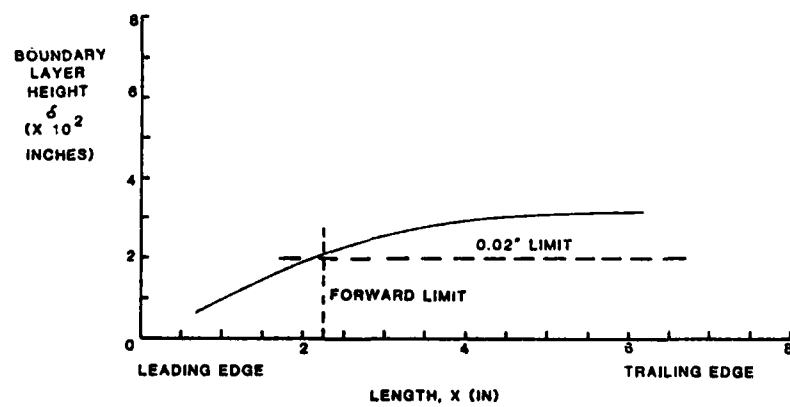


Figure 5. Shaped Block Limits

IV. Test Set-up and Procedures

The purpose of the experiment was to determine if the shaped blocks could anticipate stall. To this end, the blocks were mounted on a model that was stepped through angles of attack up to and past stall. Both digital and analog data were collected and substantiated using 2 methods of flow visualization, tufting and oil flow.

The test model was a constant cross-section NACA 0015 airfoil (Figures 6 and 7).

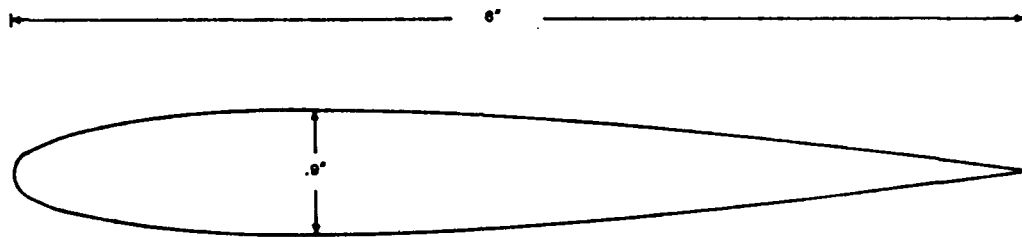


Figure 6. NACA 0015 Cross Section

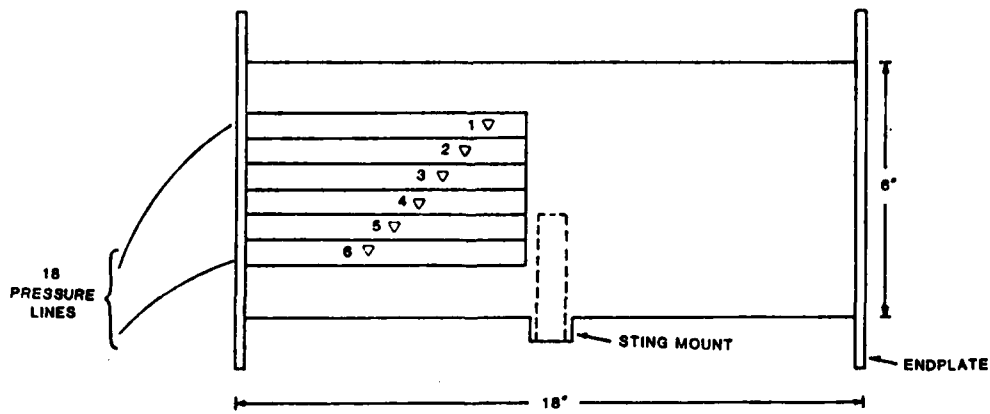


Figure 7. Model - Top View

It was fitted with end plates to eliminate tip effects and allow it to approximate an infinite wing. This particular model was selected because it had been fitted for earlier testing with removable slats (Ref. 3) that greatly simplified the instrumentation of the model (Figures 8 and 9). Six shaped blocks were mounted on the upper surface of the airfoil, staggered both spanwise and chordwise. Stall begins at the trailing edge and moves forward. Once this condition reaches the maximum-thickness point, the airfoil (for all practical purposes) is stalled. Therefore, the blocks were placed along the chord so that any propagation of the stall would be sensed from the aftmost block (located close to the trailing edge) forward through successive blocks to the point of maximum thickness. Thus, the blocks were placed in the region of primary interest, between the trailing edge and the point of maximum thickness, to detect the propagation of stall. The blocks were staggered spanwise to minimize any possible interference effects between the blocks, and each block was mounted on a slat channeled out to allow for the installation of flexible tubing (Figure 9).

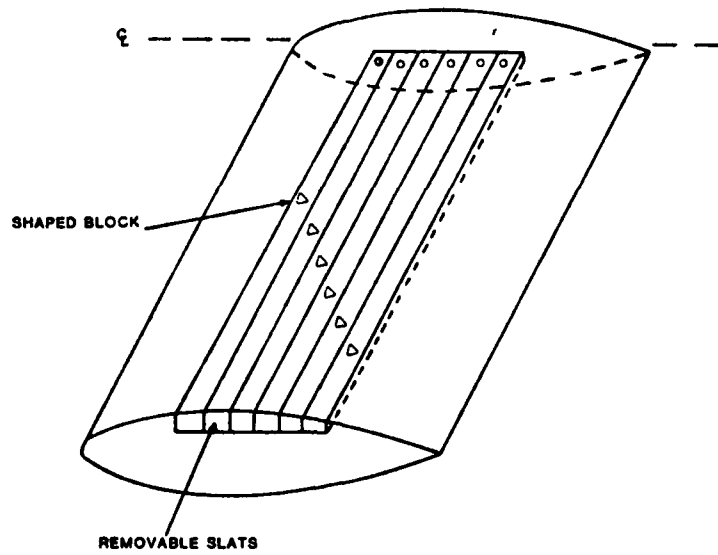


Figure 8. Model - End View

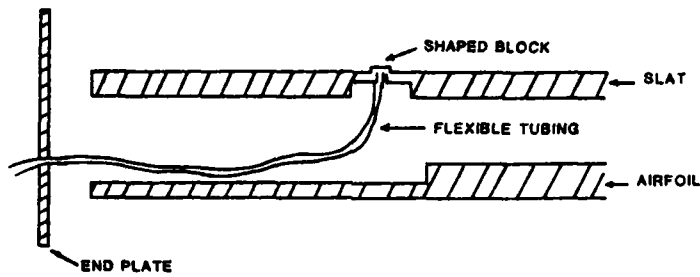


Figure 9. Model Instrumentation - Exploded View

The model was mounted on a 0.75-inch Mark II force balance manufactured by the Task Corporation. The balance uses strain gauges to convert lift, drag, and moment data into voltage signals, which are then input directly into a PDP 11/45 digital computer for storage, manipulation, and output using the USAF Academy's standard control and data-reduction program. This program was modified slightly to fit the particular needs of this project. The balance itself was installed in the 2-feet by 3-feet test section of the USAF Academy's subsonic wind tunnel (Figures 10 and 11). Data from each of the 18 pressure ports were collected through a 48-channel pressure scanning valve manufactured by the Scani-Valve Corporation (Figure 12). The scanning valve is a pressure-measuring device capable of sensing the pressure at a number of different locations by means of a single-pressure transducer and a rotary arm that samples each pressure channel in turn. The scani-valve's output signals were also fed into the PDP 11/45 computer. Figure 13 depicts the flow of data during the experiment.

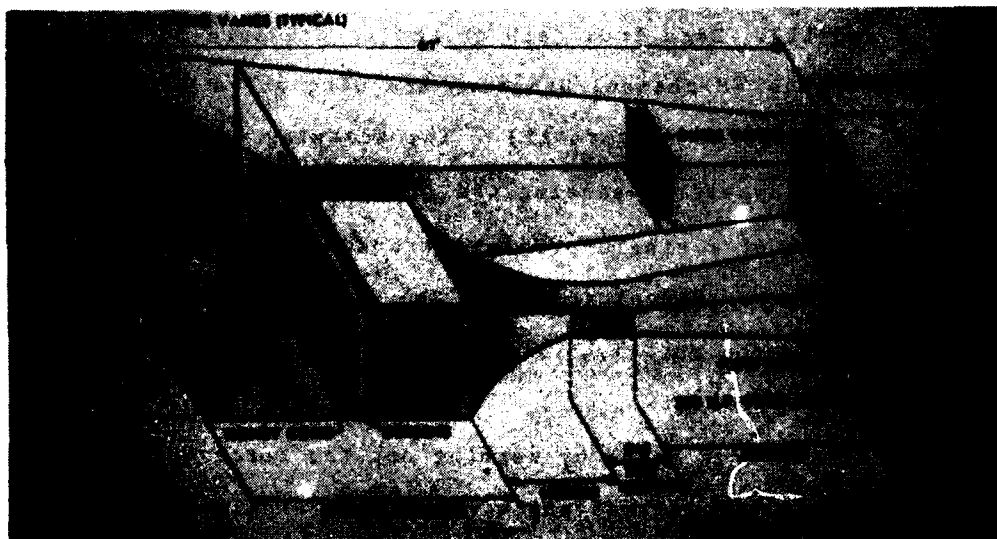
A typical test run began by zeroing out the force balance. The model was then placed at its initial angle of attack, and the wind tunnel was brought up to the test Mach number of either 0.1 or 0.2. Next, the model was stepped through a series of angles of attack ranging from -5 to +25 degrees in increments of 1 degree, pausing at each angle to collect data.

USAFA-TR-83-15



A

Figure 10. Model Mounted in Wind Tunnel



B

Figure 11. USAFA 2' x 3' Subsonic Wind Tunnel

USAF-A-TR-83-15

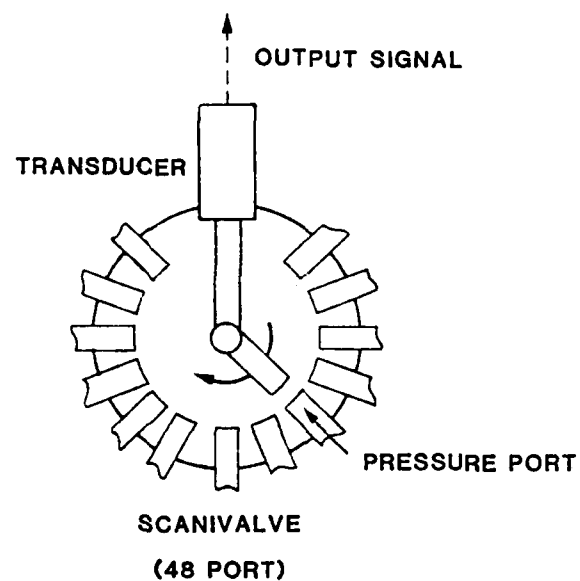


Figure 12. Scanivalve

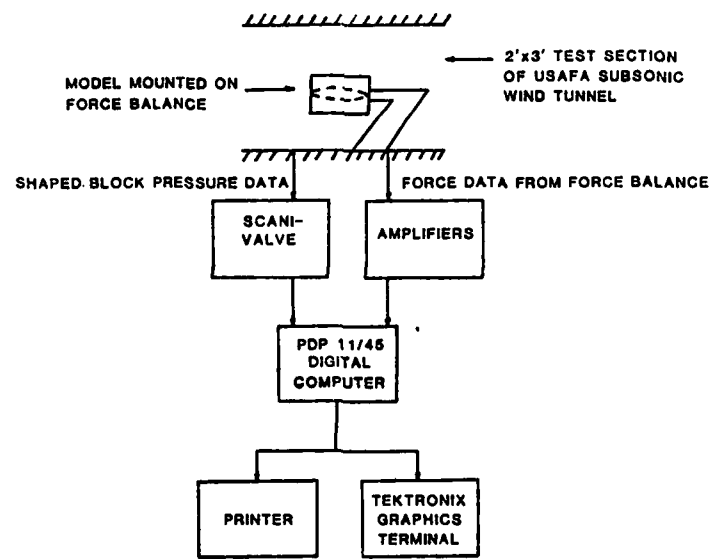


Figure 13. Data Flow

Additionally, the tests were repeated in increments of half and quarter degrees, as well as using analog traces, to insure that the method of moving the model was not influencing the data in any way. The data collected at each angle of attack included the lift and drag on the model as well as the pressure data for each port of each shaped block. After the data were reduced by the computer, they were printed out in tabular form and plotted using a Tektronix Graphics Terminal.

V. Results

The model aerodynamically duplicated previous work and compared well with published data. Plots of  $C_L$  versus  $\alpha$  (Figures 14 and 15) produced from wind tunnel data agreed with data produced by the tests described in Ref. 3 and the curves shown in Ref. 4.

In general, the shaped blocks performed as predicted. The results are summarized in Table II. The runs done at  $M = 0.1$  show that the airfoil stalls sooner at lower velocities. Given the same air density, wing area, and lift curve for 2 different speeds, this result would be expected. The table also shows that the shaped blocks do not anticipate stall as well when  $M = 0.1$ . At  $M = 0.2$  the blocks anticipated stall 5 degrees of angle of attack in advance of the actual stall as compared to 3 degrees for  $M = 0.1$ . This is because the lower Mach number produced a smaller and more-difficult-to-detect pressure difference across the shaped block.

The only inconsistency in the data is in Run 12. Prior to this run, half of the airfoil had been painted black in preparation for an oil-flow study. Consequently, the roughness of this paint surface altered the Reynolds number and had the effect of tripping the boundary layer, making it turbulent. The more energetic turbulent flow had more momentum to overcome the adverse pressure gradient, meaning that it reversed its

direction later. Because of this altered condition, stall was anticipated at a higher angle of attack than normal. The rough paint was removed, and a smoother paint finish was applied.

The only prediction found not to be true was that the progression of stall could be observed moving forward from the trailing edge. With the aftmost block (Block 6), there were some indications of this progression, showing reversal 1 degree before the other blocks, but no significant pattern of stall propagation was noted. The most important result was that the shaped blocks anticipated stall 5 degrees before it occurred at an angle of attack of 20 degrees.

Test Run 13 was a typical one, so that the remainder of this paper will analyze in detail the results of this particular test. Run 13 was done at  $M = 0.2$  and angles of attack from  $-5$  to  $+25$  degrees in 1-degree increments. The airfoil stalled at approximately 20 degrees angle of attack, although the blocks predicted stall at  $\alpha = 16$  degrees. Figures 14 and 16 illustrate the lift curve of the model and summarize the pressure data for each shaped block using the parameter PDIA explained earlier.

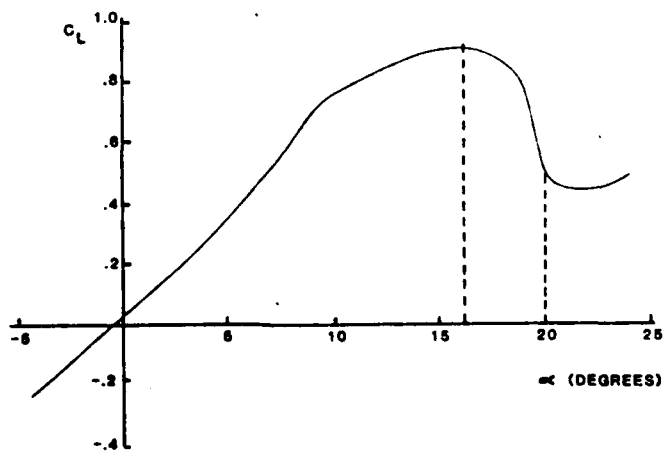


Figure 14. Digital  $C_L$  versus  $\alpha$  Curve

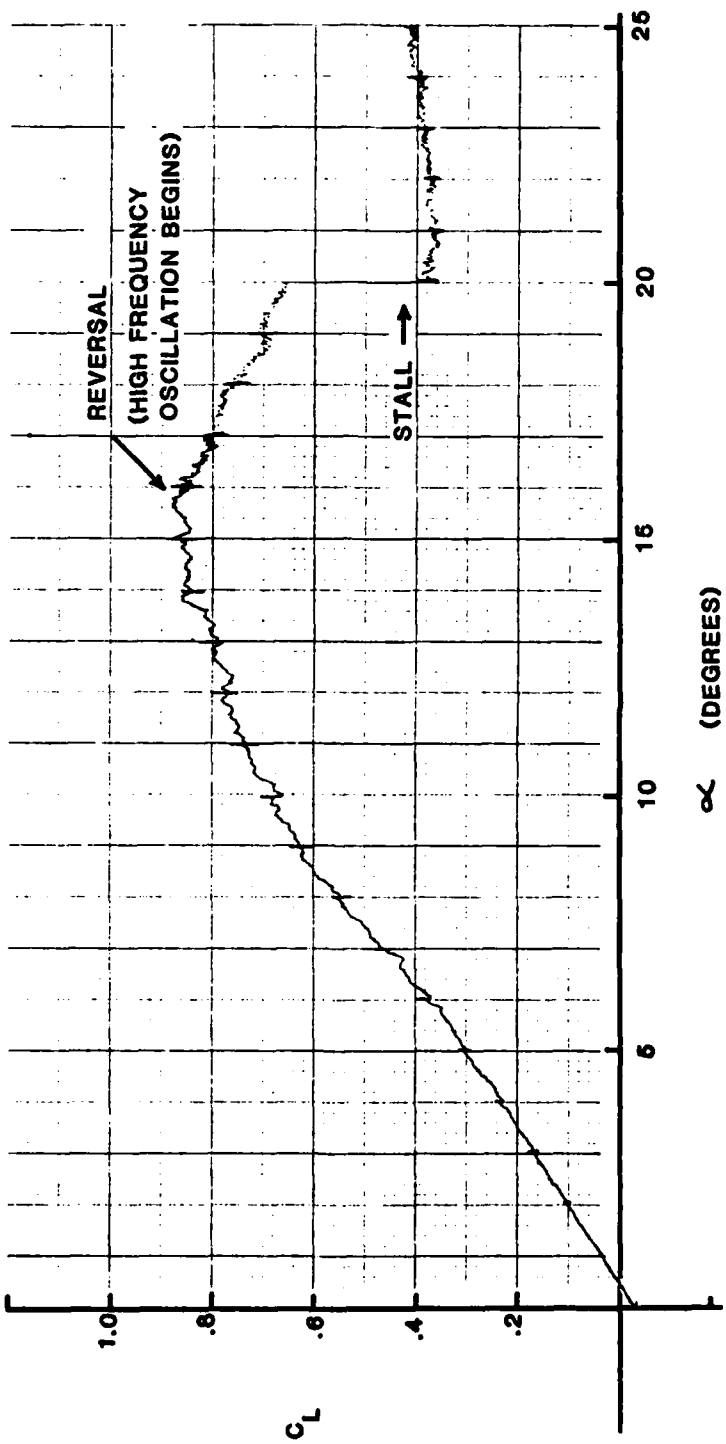


Figure 15. Analog  $C_L$  versus a Trace

Table II  
SUMMARY OF TEST RESULTS

RUN	M	$\alpha_{MIN}$	$\alpha_{MAX}$	$\Delta\alpha$	a Reversal of Block						$\alpha_{STALL}$
					1	2	3	4	5	6	
1	.1	-5	25	1	18	17	17	16	16	16	19
2	.2	-5	25	1	16	16	16	16	16	15	20
3	.2	5	20	.5	16.5	16.5	16.5	16.5	16.5	15	20
4	.1	5	20	.5	17	17	17	17	17	16.5	*
5	.2	2	22	.5	16.5	16.5	16.5	16.5	16.5	14	20
6	.1	2	22	.5	16.5	16.5	16.5	16.5	16	15	16.5
7	.1	13	21	.25	17.5	17.5	17.25	17	16.5	15.25	17.5
8	.2	13	21	.25	15.75	15.75	15.75	15.75	15.75	15.5	19.75
9	.2	-5	25	1	15	15	15	15	15	15	**
10	.2	-5	25	1	15	15	15	15	15	14	20
11	.2	-5	25	1	15	15	15	15	15	15	20
12	.2	-5	25	1	20	20	20	19	19	17	20
13	.2	-5	25	1	16	16	16	16	16	16	20
14	.2	5	22	.5	15	15	15	15	14.5	14.5	20
15	.2	12	21	1	16	15	15	15	15	15	20

\* Invalid C Data -- Incorrect Amplifier Gains

\*\* No Lift Data Taken on This Run

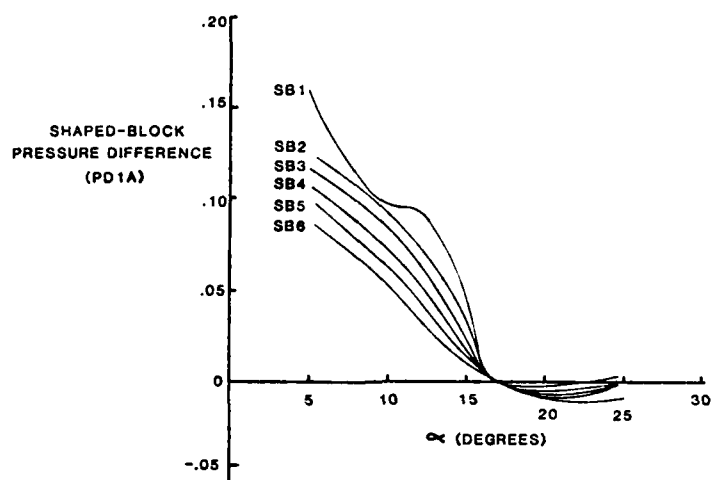


Figure 16. Digital Pressure Summary

A number of other methods were used to verify the digital data. First, half of the model was tufted (Figure 17). The tufts were adequate to show when the model stalled, but because of their large size in comparison to the boundary-layer height, they could not remain unaffected by the freestream and therefore did not show where flow reversal occurred.



Figure 17. Tufted Airfoil

Next, the results of Run 13 were duplicated using analog traces of the variables of interest. Referring back to Figures 14 and 15, it can be seen that the analog trace of Figure 15 verifies the digital  $C_L$  versus the  $\alpha$  curve of Figure 14, demonstrating that stall does occur at 20 degrees. Figure 18 is a trace of all 3 pressures from Block 1, the most forward-mounted device. Pressure 1 is greater than Pressures 2 and 3, until an angle of attack of 16 degrees is reached, substantiating the results already obtained. While Port 1 acts as a total pressure source, the values of pressure at Ports 2 and 3 were static and essentially equal. At 16 degrees angle of attack, there was a crossover of the pressure traces as flow reversal occurred. Following reversal, all of the pressures remain fairly constant, since each port is in a region of separated, turbulent flow and senses only the local ambient pressure. In addition, at the point of reversal the analog traces indicate that the frequency of oscillation of the pressures increases by a factor of approximately 3. (But this frequency could not be determined accurately because of mechanical damping of the plotter pen.) The random motion of the turbulent flow accounts for this oscillation of pressure, so that this frequency jump is another indicator that separation has occurred.

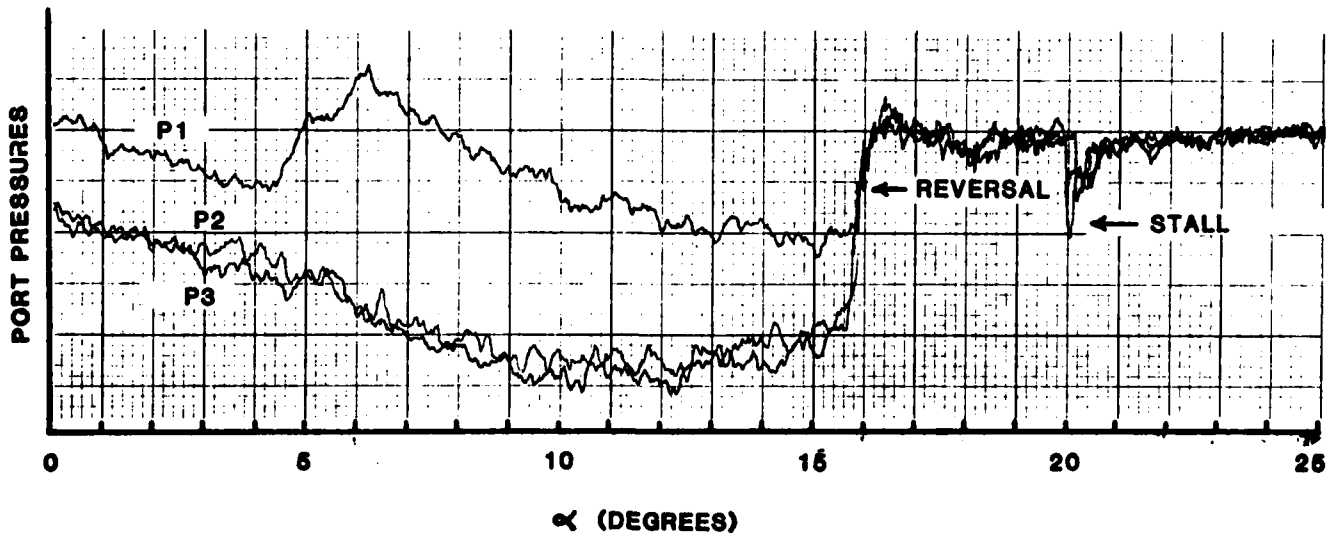


Figure 18. Analog Pressure Trace

The final method of verification was the use of flow visualization by means of oil flows. For this purpose, 1/2 of the model was painted with a smooth black paint. For each run, the painted portion of the model was sprayed with a fine mist of white oil droplets. The model was set at a predetermined angle of attack, and the tunnel was brought to the test velocity. After allowing sufficient time for the oil to flow (approximately 2 minutes), the model was removed from its mount and photographed. Figure 19 illustrates the results of the oil flows at the conditions of Run 13. At an angle of attack of 10 degrees, the flow was mostly attached with some separation at the trailing edge. But when the angle was increased to 16 degrees, the area of separation was greatly increased. At 17 degrees, the beginnings of reverse flow could be seen at the trailing edge. Finally, when the angle of attack was set at 20 degrees, there was no movement of the oil across the surface, indicating complete separation and stall.

All of this mutually supporting information indicates that stall of this particular NACA 0015 airfoil occurs at 20 degrees angle of attack and that the shaped blocks detect stall 4 to 5 degrees prior to the actual occurrence of stall.

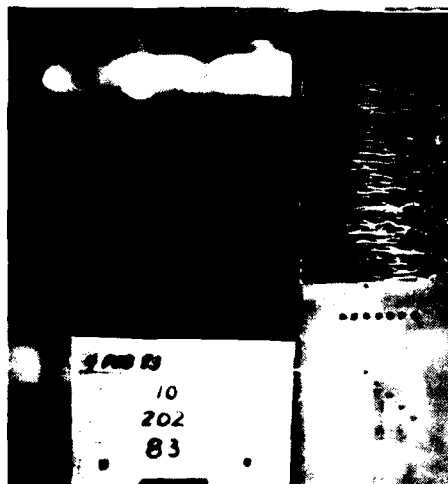


Figure 19a.

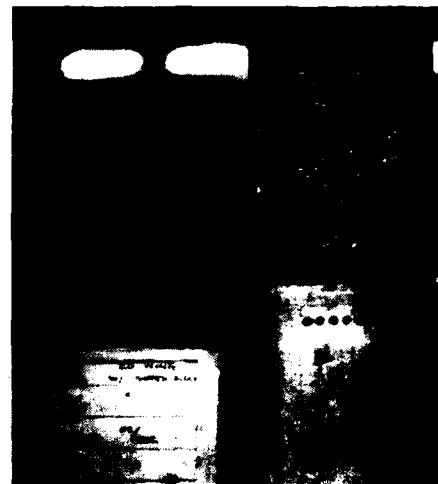


Figure 19b.

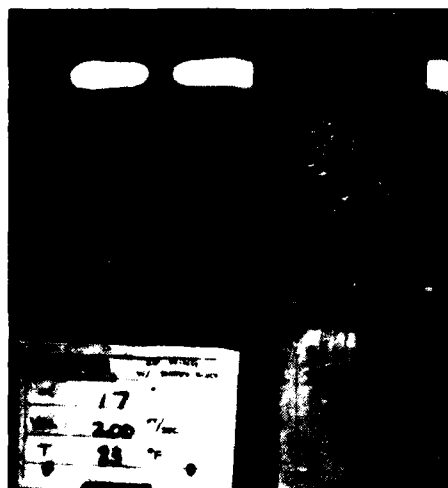


Figure 19c.



Figure 19d.

Figure 19. Oil Flows

VI. Conclusions

The shaped block is successful in anticipating stall approximately 5 degrees of angle of attack in advance of stall. And it has several other distinct advantages. First, it is a simple device, with no moving parts or delicate electrical sensors, requiring nothing more than a pressure transducer and a small microcomputer to reduce data. The only foreseeable difficulty is that the ports could become clogged by debris. However, this condition could be easily avoided by mounting a pressure transducer, with its sensing element flush with the surface of the airfoil, under each port. A second advantage is that with some very simple calibration the shaped block could be used to determine flow direction. Finally, it is a boundary-layer device. Currently, all other stall-warning systems measure only freestream velocities. By measuring boundary-layer conditions, the shaped block offers a higher degree of sensitivity.

The shaped block has 2 possible applications. The first is its obvious potential as a stall-anticipating device for aircraft. However, there is another less evident but more important task that this sensor could accomplish internally in turbomachinery. When testing new engine components, the device could be installed in areas where reverse flow is a concern. For example, if the shaped block could be successfully used to anticipate stall in a compressor, this use would be a truly significant breakthrough.

VII. Recommendations

This paper has generated 4 recommendations. First, further testing, using an oscilloscope, should be conducted to examine the usefulness of the pressure-frequency increase discussed earlier as another indicator of approaching stall. Second, the shaped block should be applied to other airfoils to see if similar results are discovered. The shaped block would

be particularly well suited for use on airfoils having well defined peaks of  $C_{L_{Max}}$ , since the angle at which PDIA equals 0 almost nearly coincides with the angle for  $C_{L_{Max}}$ . This characteristic allows the generation of a clear plot of PDIA versus  $\alpha$ , showing distinct drops when the flow reverses and the airfoil stalls. Third, this device should be evaluated against other boundary-layer devices to determine its value as a stall anticipator. One sensor that could be tested is a back-to-back pitot tube, currently employed in freestream measurements; it could be scaled down for use in the boundary layer and calibrated to sense the flow direction. Finally, the shaped block's application to turbomachinery should be investigated. Engineers at the USAF Academy have already acted upon this particular recommendation and are currently conducting application testing in compressors.

#### Symbols

##### English Symbols

$C_L$	coefficient of lift
$P$	pressure
$Re_x$	local Reynolds number
$u$	velocity component in x-direction
$V_\infty$	freestream velocity
$x$	distance aft of leading edge
$y$	vertical distance above airfoil surface

##### Greek Symbols

$\alpha$	angle of attack (angle between airfoil chord line and the freestream)
$\delta_{laminar}$	height of laminar boundary layer
$\rho_\infty$	freestream air density

References

1. Kuethe, A.M. and Chow, C.Y., Foundations of Aerodynamics: Bases of Aerodynamic Design, 3rd ed., John Wiley and Sons, New York, 1976, pp. 308-316.
2. Buzzell, W.A., "Final Report -- Development and Testing of a Skin Friction Measurement Device for Use in Turbomachinery." USAFA Technical Note in preparation.
3. Chow, C.Y., Jumper, E.J., Gay, T.C., Hoffman, M.A., and Suhr, S., "Aerodynamic Effects of Spanwise Grooves on a Symmetrical Airfoil," USAFA-TR-80-17, DFAN, USAFA, 1980, pp. 1-12.
4. Abbott, J.H. and Von Doenhoff, A.E., Theory of Wing Sections, Dover Publications, New York, 1959, pp. 324, 462.
5. McCormick, B.W., Aerodynamics, Aeronautics, and Flight Mechanics, John Wiley and Sons, New York, 1979, pp. 66-68, 163-168.

**USAF-A-TR-83-15**

**SECTION III**

**Fluid Dynamics**

MIXING OF CONSTANT-AREA ANNULAR FLOWS WITH SWIRL

Jack Denton Mattingly\*

Abstract

This paper reports the results of an experimental study of the mixing of 2 incompressible co-annular air streams with substantial swirl present in the inner stream. A five-hole pressure probe was used to measure the flow properties, including mean velocity, total pressure, and static pressure. The measurements reveal that the swirl in the inner stream creates a highly complex flow field and increases the mixing of the 2 air streams.

I. Introduction

The turbulent mixing of 2 concentric incompressible streams with swirl present in the inner stream (Figure 1) has been extensively researched in recent years, primarily because of its application to combustion and the swirling wake behind a propeller for propulsion or a windmill (Ref. 1). Swirling flows have been classified by King, Rothfus, and Kermode (Ref. 2) according to the wall boundary conditions into the types listed below:

1. unconfined swirling flows in which the wall effects are negligible (e.g. wake behind propeller or windmill),
2. small L/D confined swirling flows, which occur in large-diameter chambers where sidewall effects strongly interact with the swirl to produce significant secondary reverse flows (e.g. combustors), and
3. large L/D confined swirling flows, which occur in tubes where circumferential wall effects interact strongly with the swirl flow (e.g. tubes of heat exchangers).

To date, most investigations of this flow configuration have studied the mixing of fuels and air in combustors where a secondary reverse flow (Figure 2) provides the necessary flame stability and greatly influences the mixing process (Refs. 3 through 7). In many engineering applications

---

\*Major, USAF, Associate Professor of Aeronautics, DFAN

of turbulent mixing with swirl, however, a centerbody may be present, and the secondary reverse flow is absent. For example, in modern turbofan engines the engine core stream is mixed with the fan stream to improve the engine thrust and/or to reduce the nozzle exhaust noise.

Experimental data and analytical methods have been developed for unconfined swirling flows and small L/D swirling flows in combustion chambers (Refs. 1 through 8). But the experimental data for the turbulent mixing of 2 concentric incompressible streams in a constant cross-sectional area channel, with swirl present in the inner stream, is limited and insufficient. To my knowledge, the only research in this area is a study by Launder and Morse (Ref. 9) of a swirling jet with and without an external coaxial stream. Apparently no research has been performed with a centerbody present, a configuration with many applications to turbofan engines.

This study experimentally obtained the variation of mean flow properties for the turbulent mixing of 2 concentric incompressible air streams, with swirl present in the inner stream, flowing through a constant area annulus. Five sets of experiments were performed with a swirl ratio (tangential to axial velocity ratio) of 0.8 in the inner stream. The test configuration for the experiments is shown in Figure 3 and the mass flow ratio listed in Table I. A five-hole probe was used for mean flow measurements of the mixing. A discussion of the five-hole probes, test apparatus, and experimental results appears below.

### II. Five-Hole Pressure Probe

The five-hole pressure probe consists of a single forward hole, positioned along the probe centerline, surrounded by 4 additional holes on a conical surface, as shown in Figure 4.

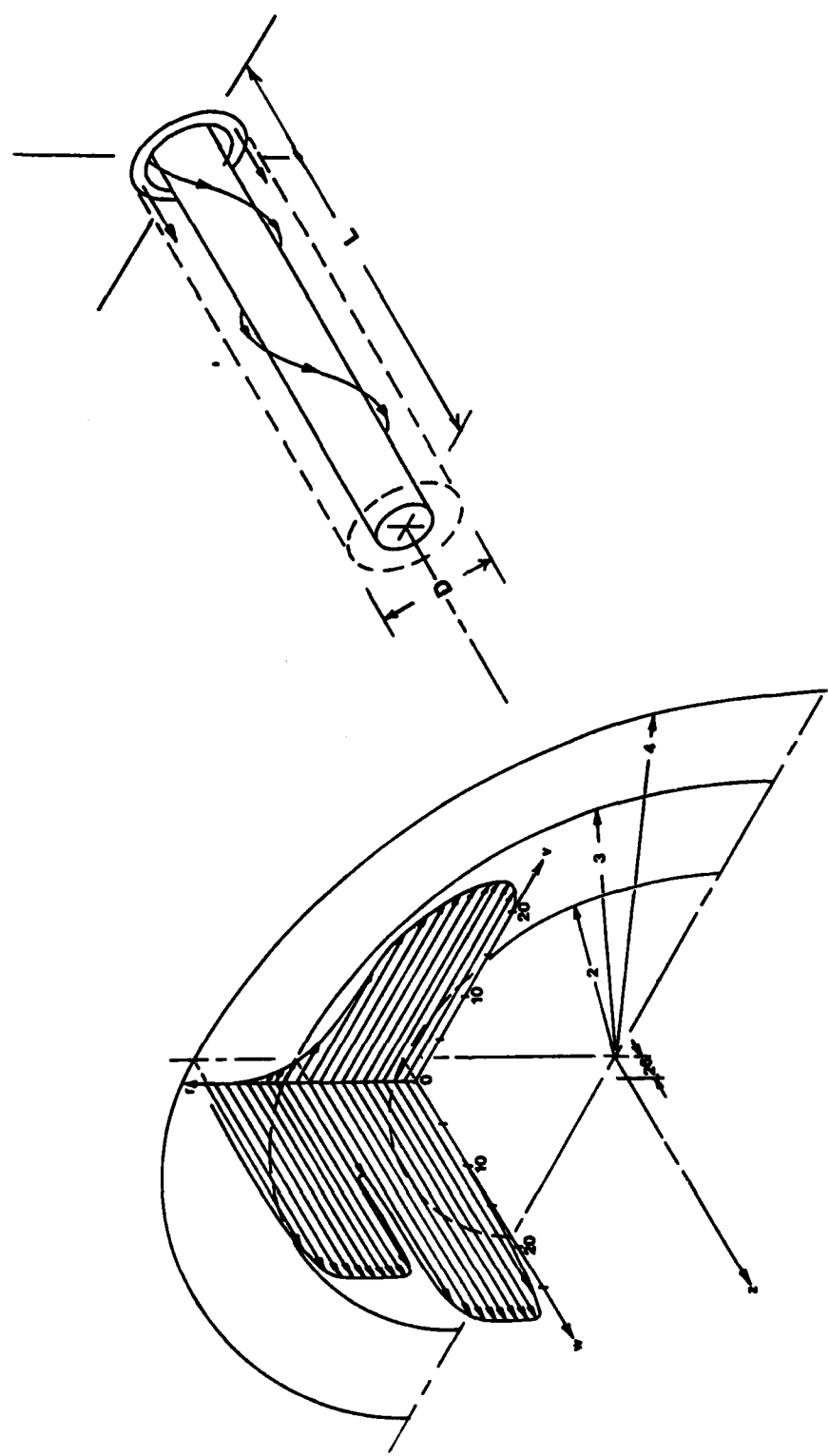


Figure 1. Flow Configuration of Interest

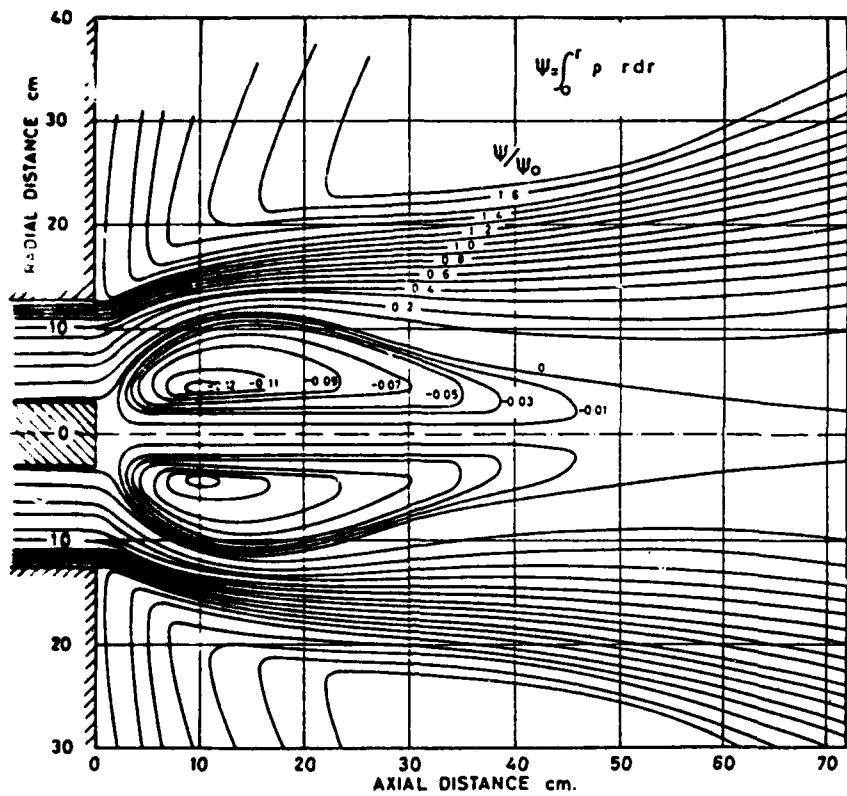


Figure 2. Streamlines of Recirculation Eddy in Swirling Annular Free-jet,  $S = 1.57$  (Ref. 4)

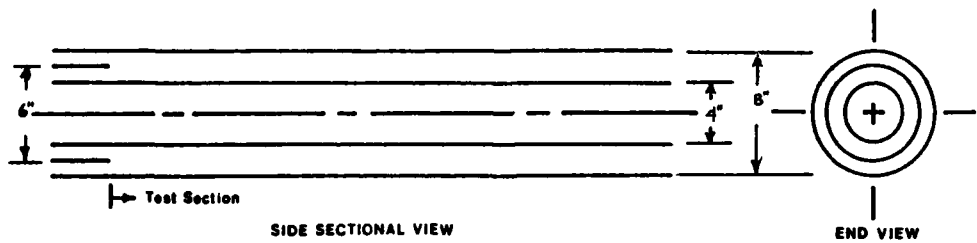
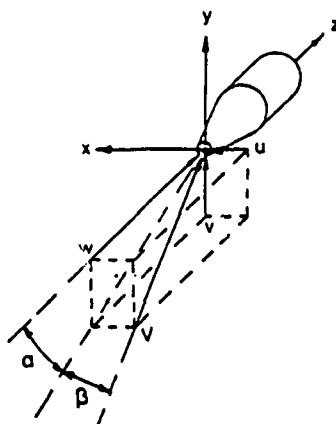


Figure 3. Test Section for Experiments

Table I  
EXPERIMENTS

Test	$\alpha$ $(\dot{m}_o / \dot{m}_i)$
1	0.00
2	0.47
3	1.00
4	2.13
5	3.91



$$\begin{aligned} u &= V \sin \beta \\ v &= V \sin a \cos \beta \\ w &= V \cos a \cos \beta \end{aligned}$$

Figure 4. Body-Fixed Coordinate System

Erwin (Ref. 10) describes this type of probe and provides typical calibration data for it. The procedure described by Erwin for using this type of probe requires that the pressures from 2 holes on opposite sides of the conical surface be nulled. Baker, Gallington, and Minster (Ref. 11) describe a calibration procedure that does not require moving the probe to a null position during measurement. The compressed air system used in the experiments conducted for this paper limited the time of measurement and thus prohibited the use of the procedure described by Erwin. Also, the radial and angular location of the probe head changed

when the probe was rotated, an undesirable condition in an axisymmetric coordinate system. The calibration procedure described by Baker et al. eliminates these drawbacks; however, the accuracy of the measurements is compromised by the larger calibration regime. Dring, Joslyn and Hardin (Ref. 12) describe a modified five-hole probe whose head remains in an essentially constant position when the probe is rotated. The high accuracy requirement and the limited time of measurement are satisfied by the type of probe described by Dring et al. used with a modification of the calibration and measurement procedures described by Baker et al.

One small probe (Figure 5) was manufactured according to the instructions provided by Gallington and Hollenbaugh (Ref. 13). This probe was calibrated using the methods of Baker et al. over a small range of angle of attack ( $\alpha$ ) and a large range of angle of sideslip ( $\beta$ ). During measurement, the probe is rotated (Figure 6a-b) to minimize the pressure difference between the 2 pressure holes on the conical surface that are directly related to the angle of attack ( $\alpha$ ). Since nulling is not required for determining the exact angle of attack, the time for measurement of the flow by the five-hole probe is reduced considerably. The accuracy of the measurements remains high since the probe is calibrated for a small difference in the flow's angle of attack relative to the probe's axis and for a large range of angle of sideslip.

Once the calibration coefficients have been determined, then measurement of the pressure at the 5 holes on the probe,  $P_1$  through  $P_5$ , yields a value for each of the following properties:

1. Axial velocity,  $w$
2. Tangential velocity,  $v$
3. Radial velocity,  $u$
4. Total velocity,  $V$
5. Static Pressure,  $P_S$

### 6. Total Pressure, $P_T$

In axisymmetric flow with swirl, the tangential and axial momentum fluxes are very important properties, as shown by Eqns. (B12) through (B18) in Appendix B. (This appendix develops the analytical integral relationships for determining the swirl number from the momentum fluxes.) The axial and tangential momentum fluxes can be written as follows for incompressible axisymmetric flow:

$$M_z' = \rho(w^2 - v^2/2) \quad (1)$$

$$M_\theta = \rho v w \quad (2)$$

where  $M_z'$  is the axial-momentum flux,  $M_\theta$  is the tangential-momentum flux, and  $\rho$  is the density of incompressible fluid.

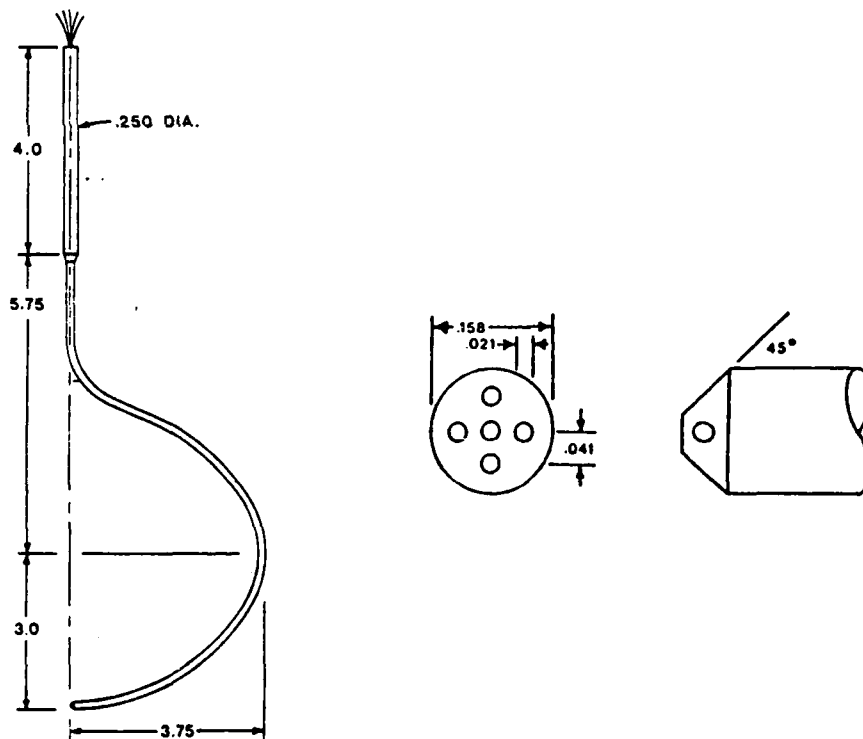


Figure 5. Dimensions of Probe in Inches

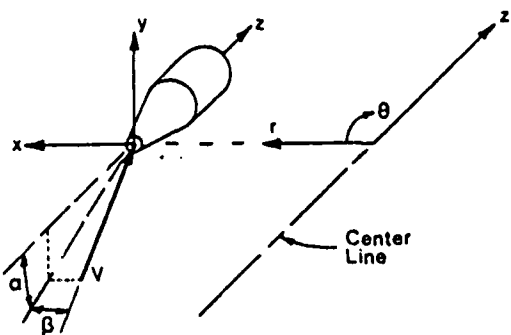


Figure 6a. Alignment of Body-Fixed and Axisymmetric Coordinate System

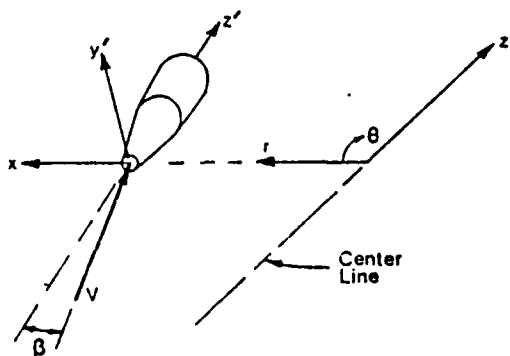


Figure 6b. Probe Rotated to Null Flow Angle

### III. Test Apparatus

The test apparatus consists of the following elements:

1. High pressure dual air supply system
2. Concentric dual plenum section
3. Swirl generator and nozzles section
4. Test section
5. Measurement system

Figure 7 is a diagram of the high pressure air supply system. Figure 8 shows the next 3 elements of the test apparatus as listed above. Detail drawings of the plenum section, the swirl generator and nozzle section, and the probe in the outside wall of the test section are shown in Figures 9, 10 and 11, and 12, respectively. The measurement system appears in Figure 13.

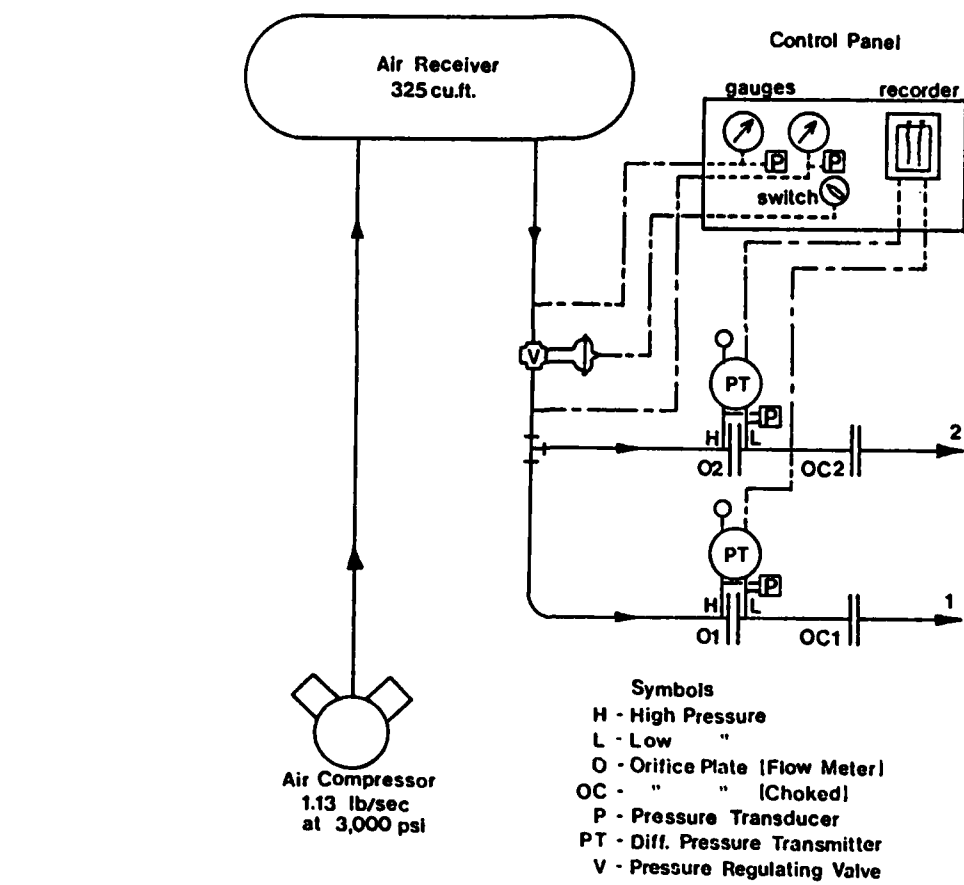


Figure 7. Modified High Pressure Dual Air Supply System

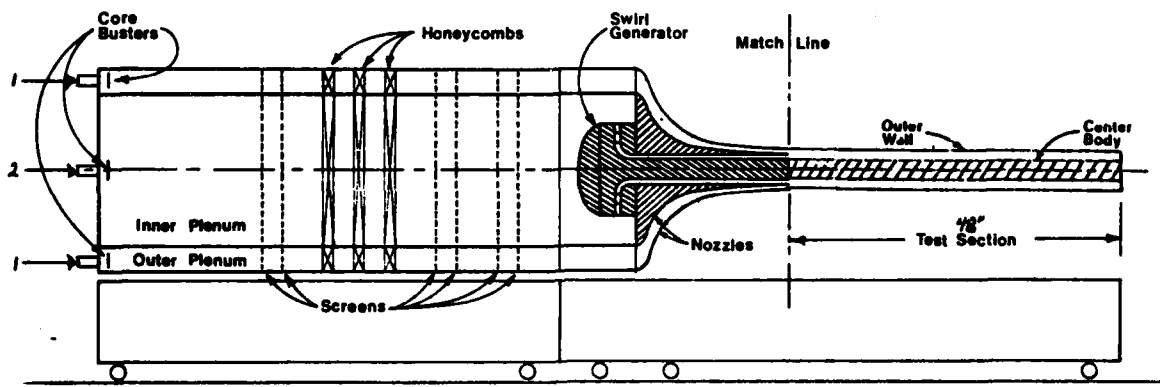


Figure 8. Test Apparatus

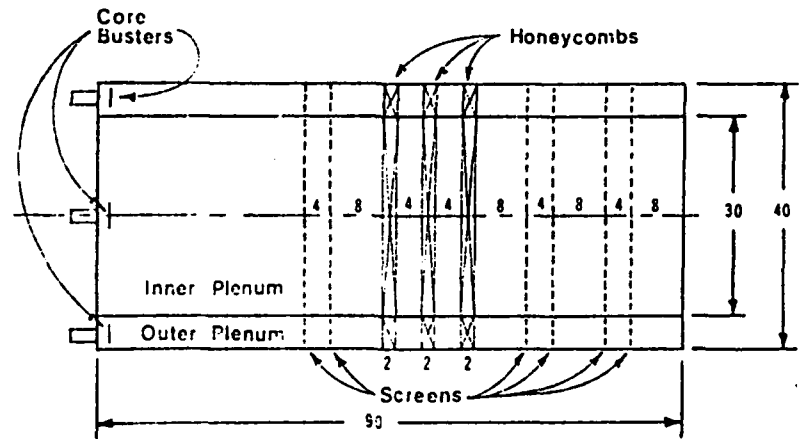


Figure 9. Dual Concentric Plenum System

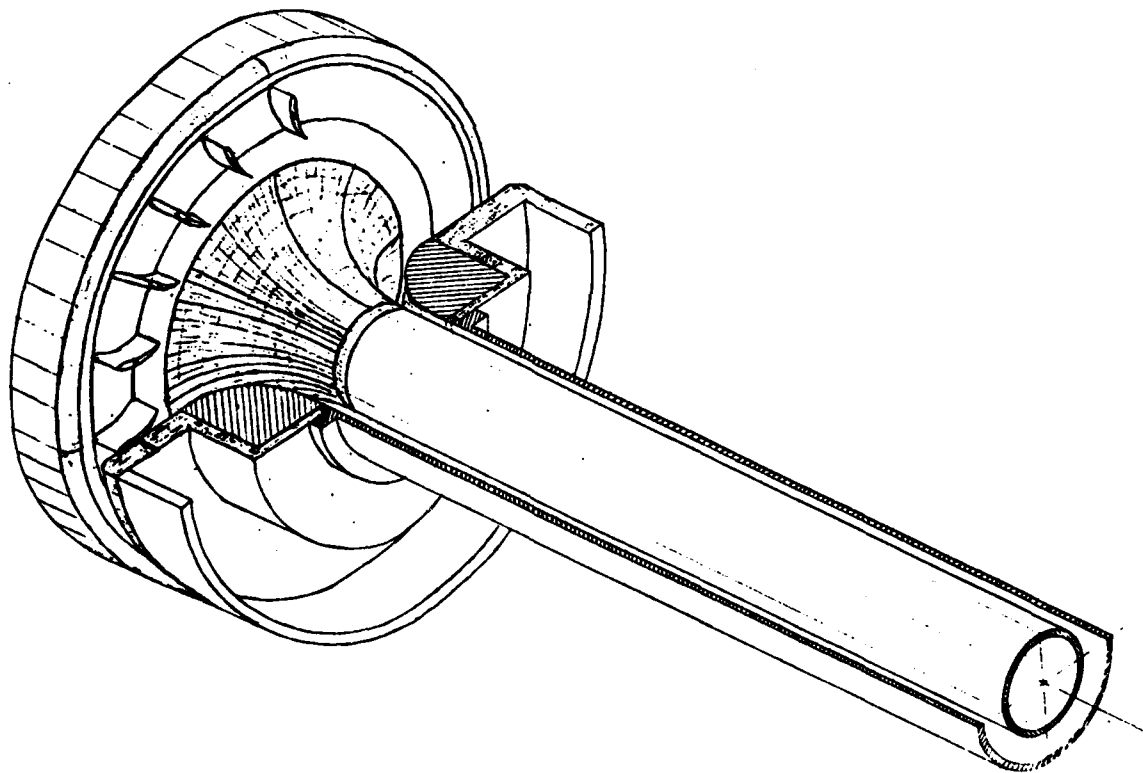


Figure 10. Isometric Section of Swirl Generator

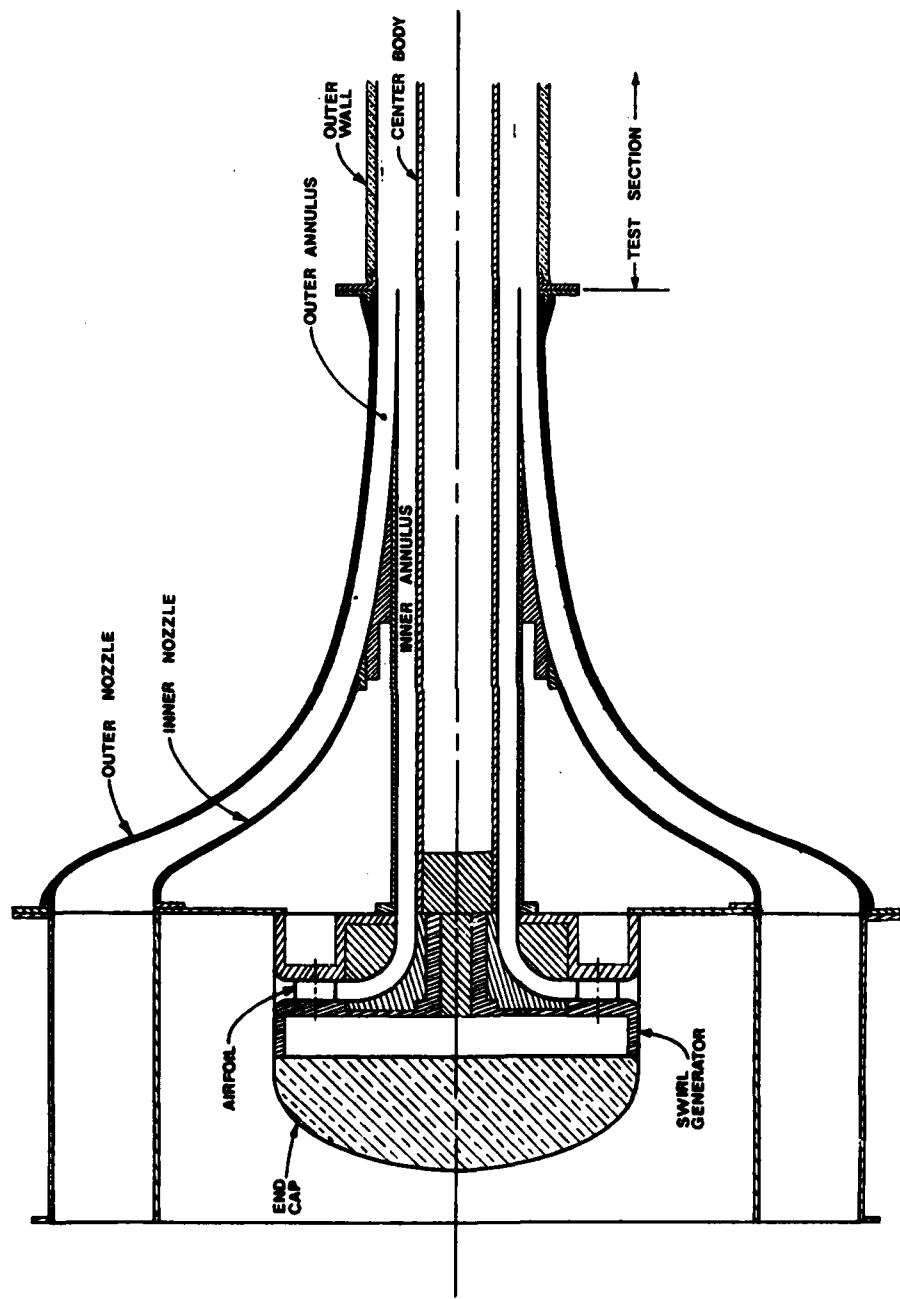


Figure 11. Swirl Generator and Nozzles

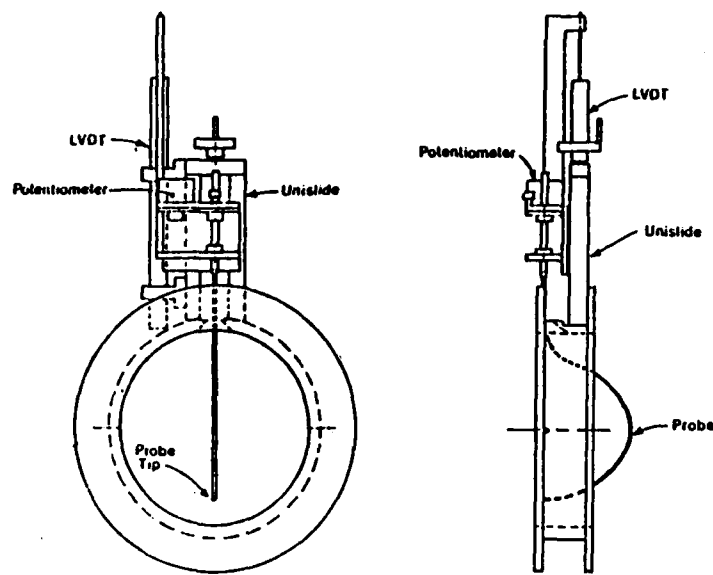


Figure 12. Probe Traversing Mechanism and Section of Outside Wall

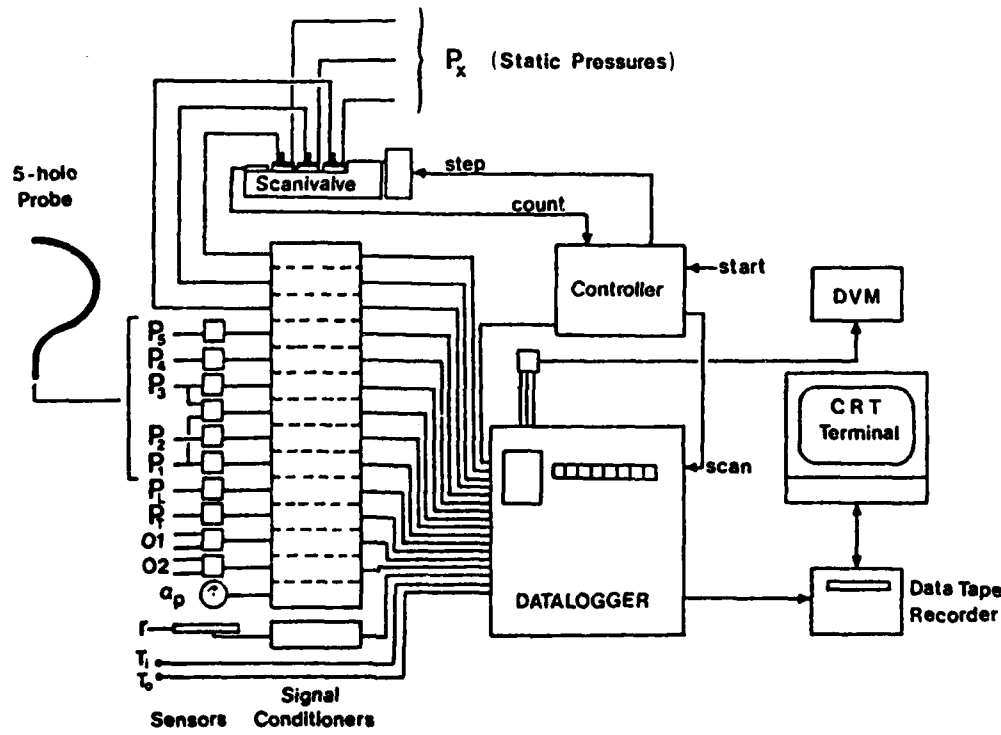


Figure 13. Measurement System

**IV. Results**

Five tests were conducted to measure the turbulent mixing of coaxial air streams with swirl present. The data used for the tests is presented in Appendix A of Ref. 14.

In the test configuration, 2 streams of air (inner stream with swirl) from concentric annuli flow into a constant-area annular duct. The reduced data gathered during this set of experiments is contained in Figures A1 through A5 in Appendix A and Figures 14, 16, 17, 18, 19, and 26. Measurements were taken for 5 different mass flow ratios,  $\alpha$ 's, or runs. Table II lists these 5 mass flow ratios and the 3 character abbreviations used to differentiate the data runs of each mass flow rate. This table also lists the figures in Appendix A containing the reduced data for the data runs, and the swirl number,  $S$  [defined by Eqn. (B20) in Appendix B of this report], at the first axial location,  $z = 0.25$  inches.

In runs XX1 ( $\alpha = 0.00$ ), a region of recirculation is established at the entrance of the test section between the inner swirling stream and the outside wall. About 4 inches downstream from the test section entrance, the inner swirling stream separates from the centerbody because of the large adverse pressure gradient (Figure 14), producing a region of flow reversal. Further downstream (about 8 inches from the entrance), the flow re-attaches to the centerbody. The streamline pattern for runs XX1 is sketched in Figure 15.

In runs XX2 ( $\alpha = 0.47$ ), the flow from the outer annulus prevents the establishment of an outer region of recirculation and reduces the magnitude of the adverse pressure gradient on the centerbody (Figure 16) preventing separation. The flow from the outer annulus also reduces the outward-growth rate of the tangential-momentum flux and its associated tangential velocity.

In runs XX3 ( $\alpha = 1.00$ ), the adverse pressure gradient on the

centerbody is further reduced by the flow from the outer annulus (Figure 17). The initial difference in axial-momentum flux between the inner and outer streams is lower than for runs XX2, and the outward-growth rate of the tangential velocity is further reduced.

In runs XX4 ( $\alpha = 2.13$ ), the outside wall of the test section and the higher velocity of the outside stream cause the boundary between the 2 streams to move inward before any significant outward growth of tangential velocity. The inward growth of axial-momentum flux reduces the outward transfer of tangential-momentum flux and its associated tangential velocity. The magnitude of the adverse pressure gradient present on the initial section of the centerbody (Figure 18) is reduced by the inward growth of the outer stream.

In runs XX5 ( $\alpha = 3.91$ ), both walls of the test section have adverse pressure gradients (see Figure 19). The adverse pressure gradient on the outside wall is caused by the inward spread of the outer stream. The inward transfer of axial-momentum flux further reduces the outward transfer of tangential-momentum flux, as compared to runs XX4.

The half-radius growth of the swirl (tangential) velocity,  $b$ , versus axial location is plotted in Figure 20 for runs XX1 through XX5. The increase in outward growth with increased swirl agrees with the results obtained by Pratte and Keffer (Ref. 15) for a swirling free-jet (Figure 21). The reduction in outward growth of the swirl velocity caused by a flowing outer stream agrees with the results obtained by Lander and Morse (Ref. 9) for swirling jet with and without an external stream (Figure 22). When the initial axial-momentum flux of the outer stream is greater than that of the inner stream (runs XX4 and XX5 in Figure 20), the rate of the inward transfer of axial momentum more than offsets the outward transfer of tangential momentum in the initial portion of the test section, and the half-radius of the swirl velocity is reduced.

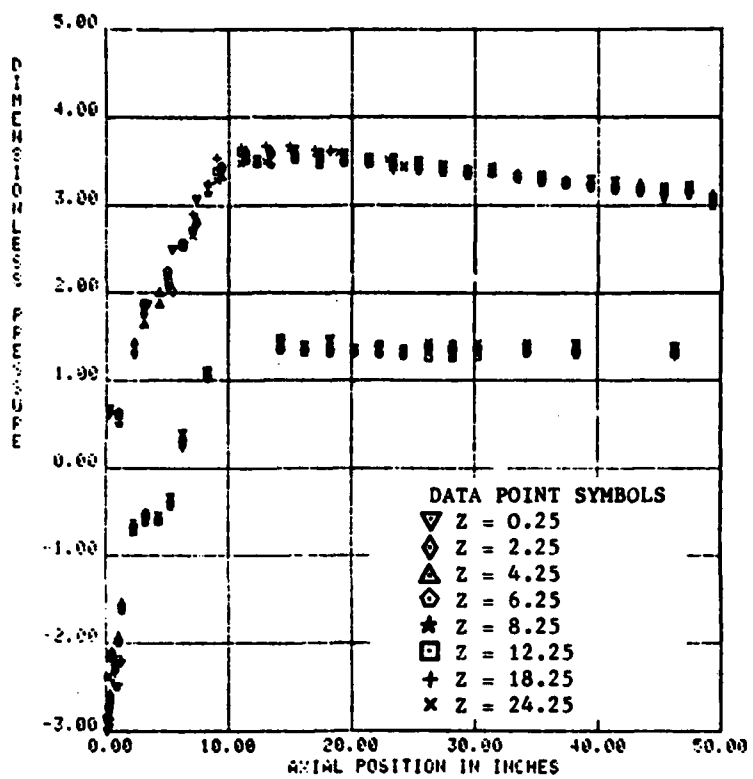


Figure 14. Static Pressure on 4-Inch and 8-Inch Tubes, Runs XX1 (See p.89 for Definition of Dimensionless Static Pressure)

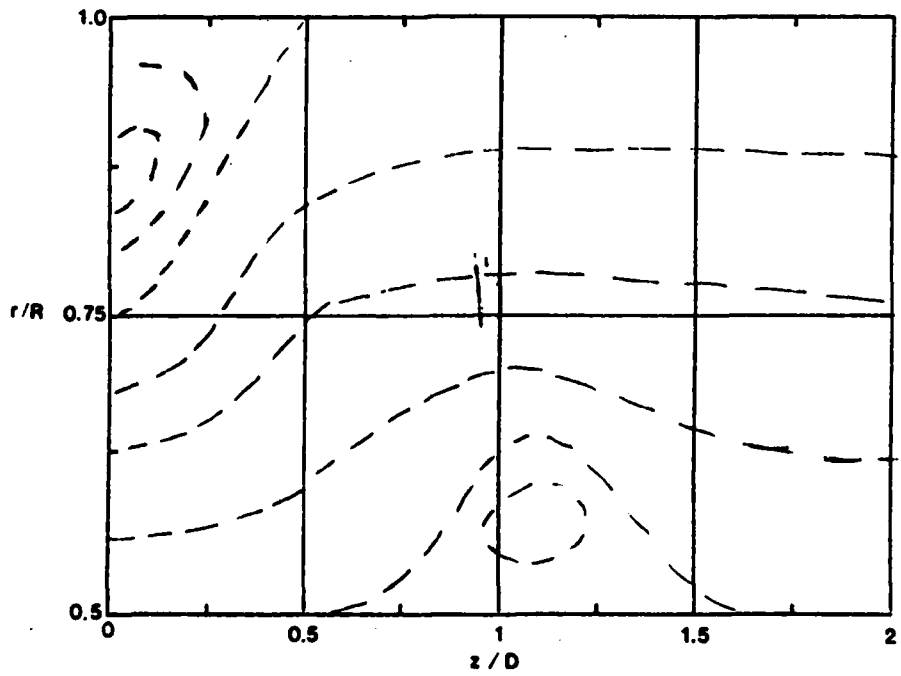


Figure 15. Streamline Pattern for Runs XX1

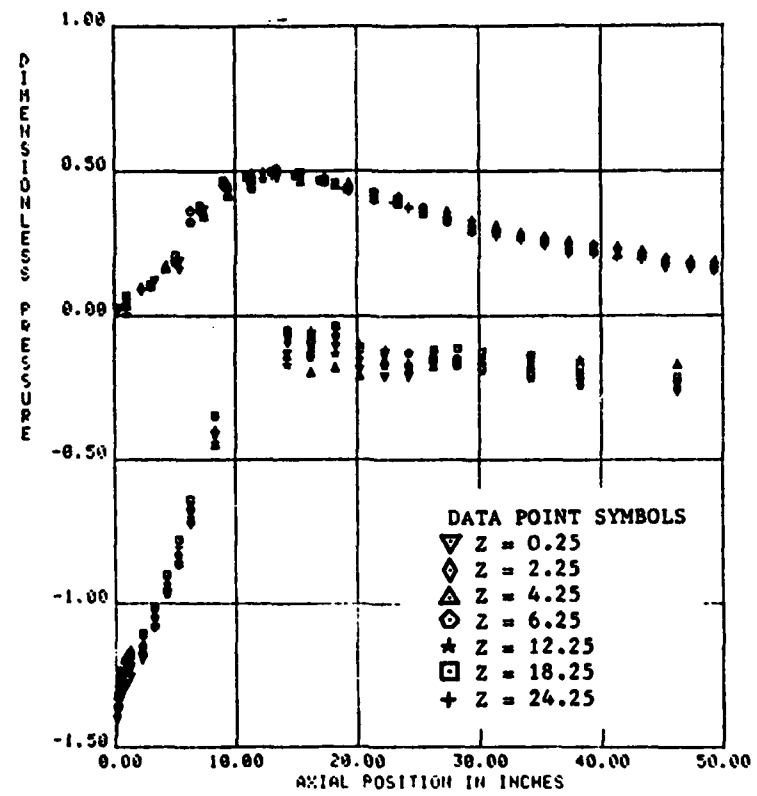


Figure 16. Static Pressure on 4-Inch and 8-Inch Tubes, Runs XX2

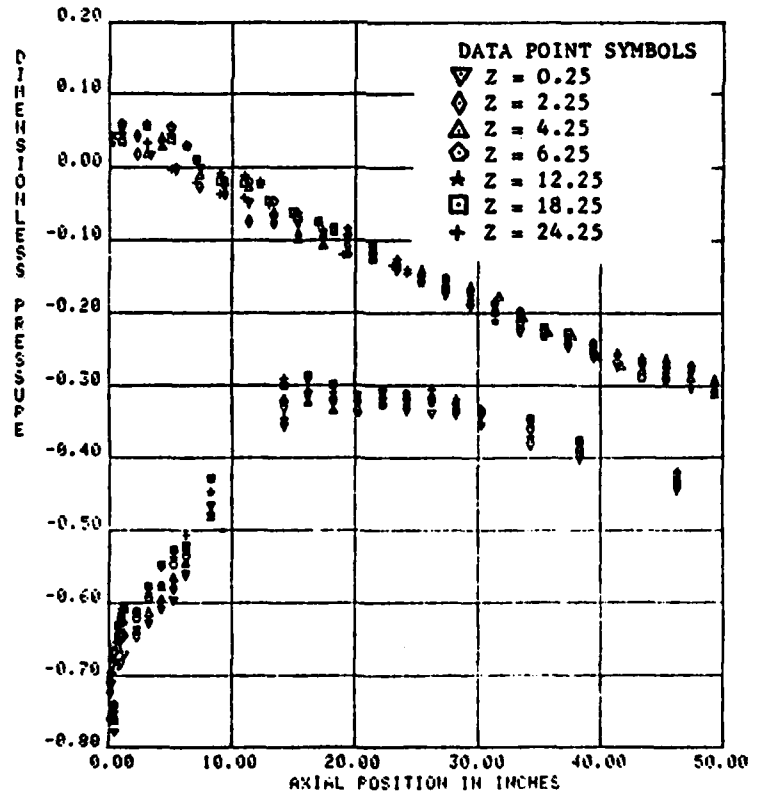


Figure 17. Static Pressure on 4-Inch and 8-Inch Tubes, Runs XX3

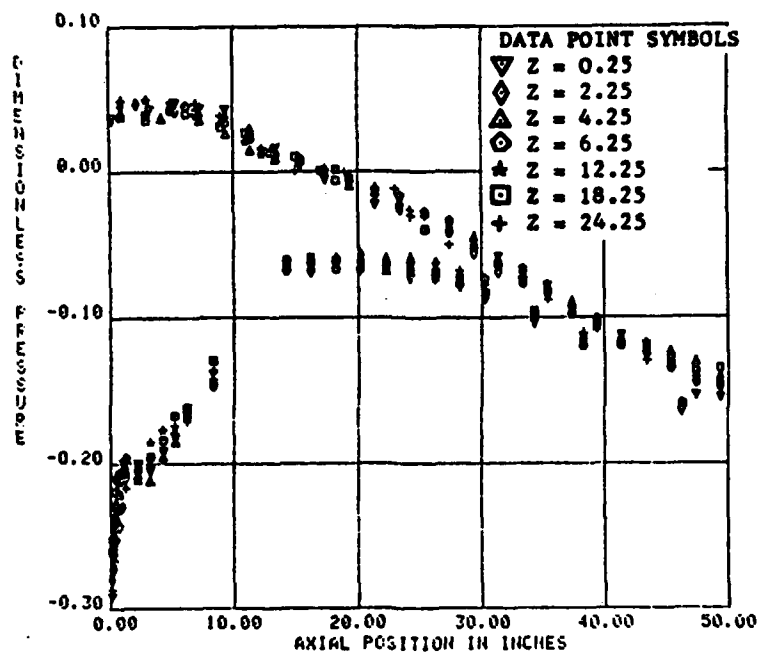


Figure 18. Static Pressure on 4-Inch and 8-Inch Tubes, Runs XX4

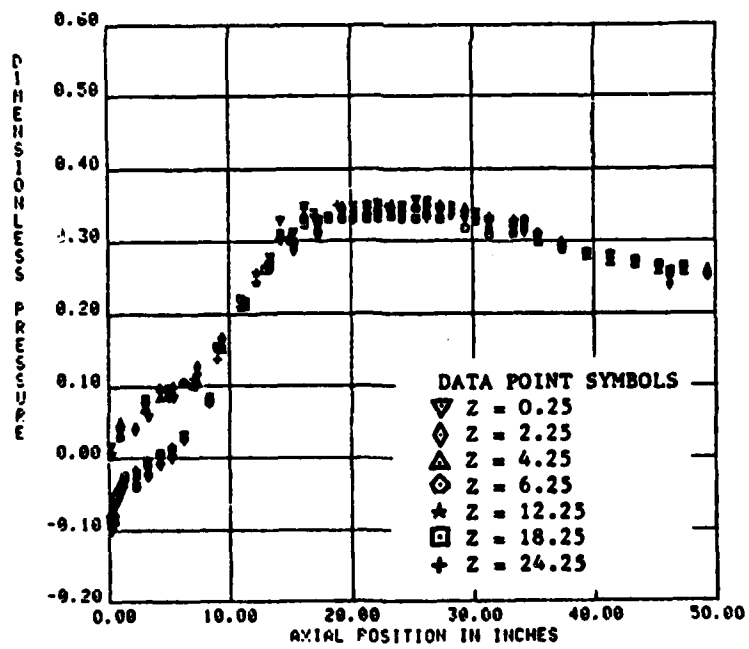


Figure 19. Static Pressure on 4-Inch and 8-Inch Tubes, Runs XX5

Table II  
FLOW RATIOS FOR TESTS

Flow Ratios		Abbreviation of Data Runs	Figures	Swirl S
$\alpha$	$V_o / V_i$			
0.00	0.000	XX1	IV-1, IV-13, & A-1	.1762
0.47	0.336	XX2	IV-3, IV-13, & A-2	.1579
1.00	0.714	XX3	IV-4, IV-13, & A-3	.1096
2.13	1.512	XX4	IV-5, IV-13, & A-4	.0379
3.91	2.793	XX5	IV-6, IV-13, & A-5	.0125

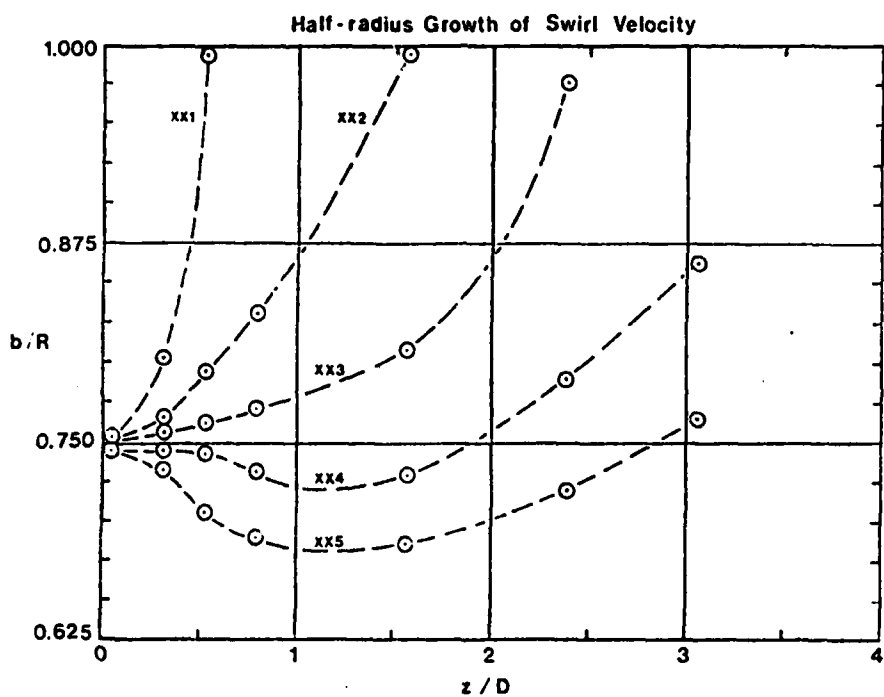


Figure 20. Half-Radius Growth of Swirl Velocity for Test

Three sets of tests for a swirling annular free-jet were conducted by the author (Ref. 14) using the test sections shown in Figure 23. The half-radius growth of swirl velocity,  $b$ , versus axial location is plotted for each test in Figure 24. A comparison of Figures 20, 21, 22, and 24 indicates the influence of swirl, centerbody, and external stream on the mixing rate (the results of this comparison are included in the next section).

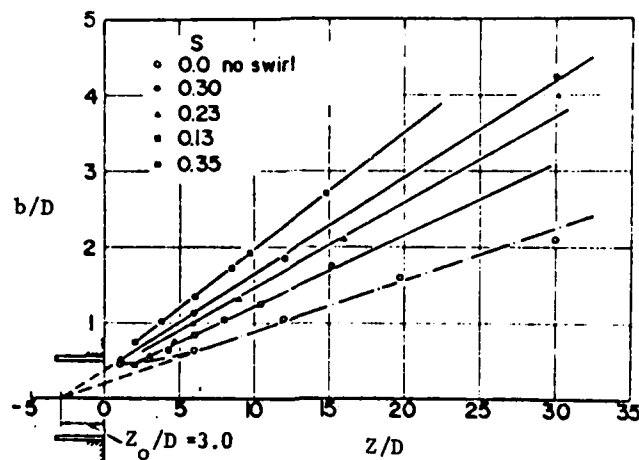


Figure 21. Half-Radius Growth as a Function of Swirl Number for Swirling Free-jet (Ref. 15)

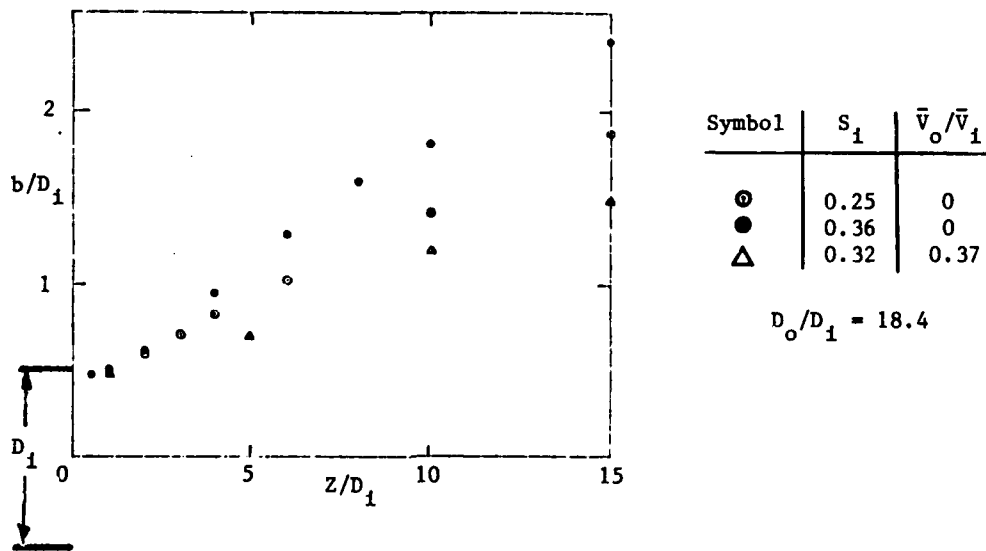


Figure 22. Half-Radius Growth of Swirl Velocity for Swirling Jet with and without External Flow (Ref. 9)

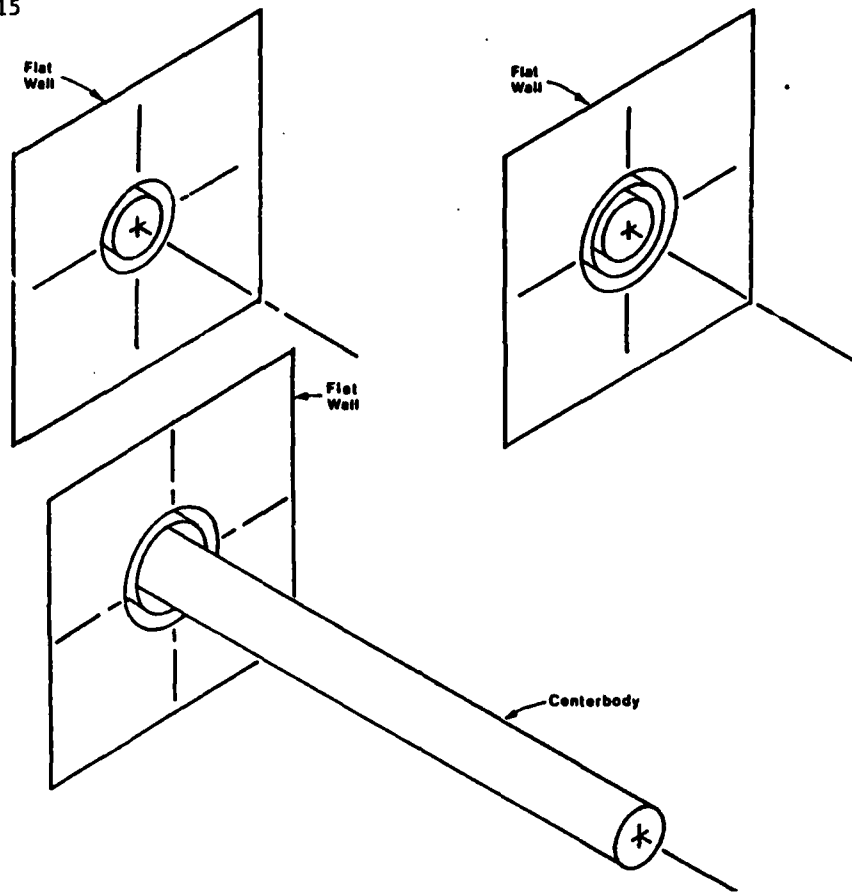


Figure 23. Test Sections for Swirling Annular Free-jet Experiments

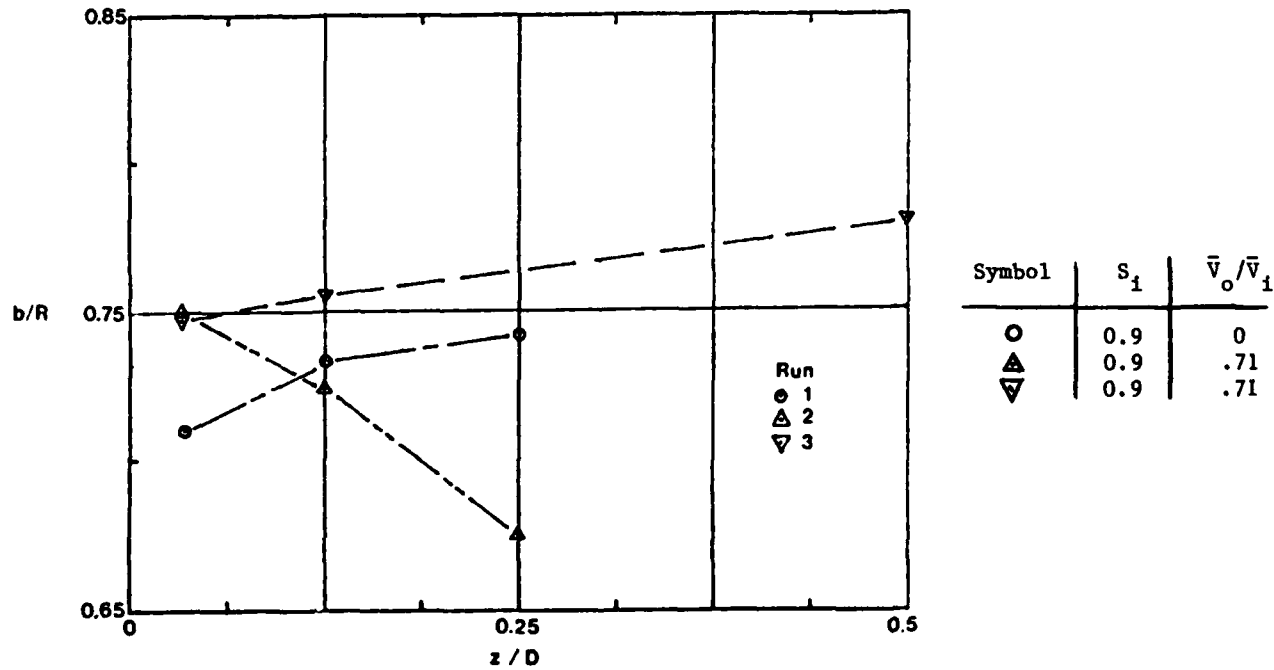


Figure 24. Half-Radius Growth of Swirl Velocity for Swirling Annular Free-jets

The variation of the swirl number,  $S$ , with axial distance for runs XX1 through XX5, is plotted in Figure 25. The swirl number has been normalized by its value at the first axial location,  $S_0$ . This initial value of the swirl number is listed in Table II. The results indicate that the decay of the swirl number with axial distance for runs XX1, XX2, and XX3 is dominated by the decay of the tangential momentum with axial distance. This result agrees with those obtained in a previous study of swirl-dominated flows (Ref. 3). The results for runs XX4 seem to indicate that this region of flow is dominated by the decay of the axial momentum with axial distance. The variation of the swirl number for runs XX5 is an anomaly caused by the use of the five-hole probe in the outer edge of its calibration region. Here small errors in predicted flow direction had a much greater effect on the tangential momentum flux than on the axial momentum flux. This type of anomaly can be prevented by using the probe near the center of its calibration region where errors in flow direction are much smaller.

The variation of the static pressure along the outside wall of the inner annulus upstream of the test section is presented in Figures 26 and 27 for runs XX1 through XX5. The static pressures in Figure 26 have been nondimensionalized by the dynamic pressure associated with the average axial velocity in the test section ( $\bar{V}$ ), and those in Figure 27 have been nondimensionalized by the dynamic pressure associated with the average axial velocity in the inner annulus ( $\bar{U}$ ). The influence of the outer stream on the pressure along the outside wall of the inner annulus can be seen for runs XX3, XX4, and XX5 by comparing Figures 26 and 27. For runs XX1 and XX2, the static pressure on the outside wall and at the end of this wall are only a function of the dynamic pressure of the inner stream and the axial location (Figure 27). The upstream influence for runs XX3, XX4, and XX5 can be seen in Figure 27 (i.e., the higher the mass flow

ratio,  $\alpha$ , the farther upstream the influence).

The coefficient of friction,  $c_f$ , presented in Table III, was calculated from static pressure measurements along the centerbody and outside wall (see plots of wall static pressure in Appendix A). These calculations were based on the dynamic pressure  $Q (= 1/2 \rho \bar{V}^2)$ . The higher values of the coefficient of friction at the outer wall reflect the existence of larger tangential velocities near this wall and the higher turbulence present due to this extremely unstable boundary layer. Scott and Rask (Ref. 16) explain that this increase in the coefficient of friction at the outer wall is caused by unstable flow, which increases the turbulent production and promotes turbulent transfer.

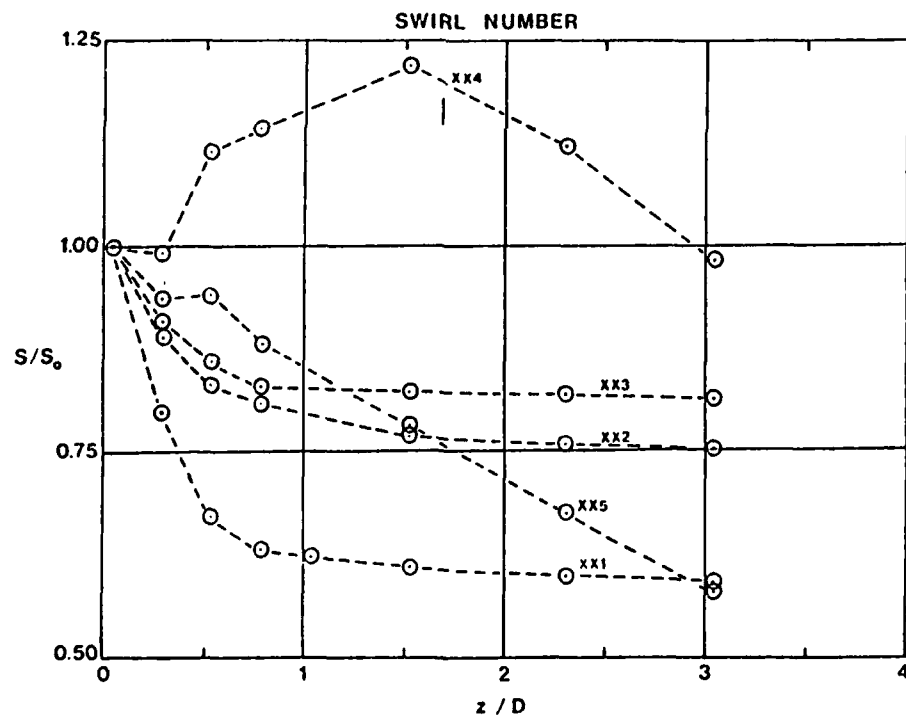


Figure 25. Swirl Number Decay

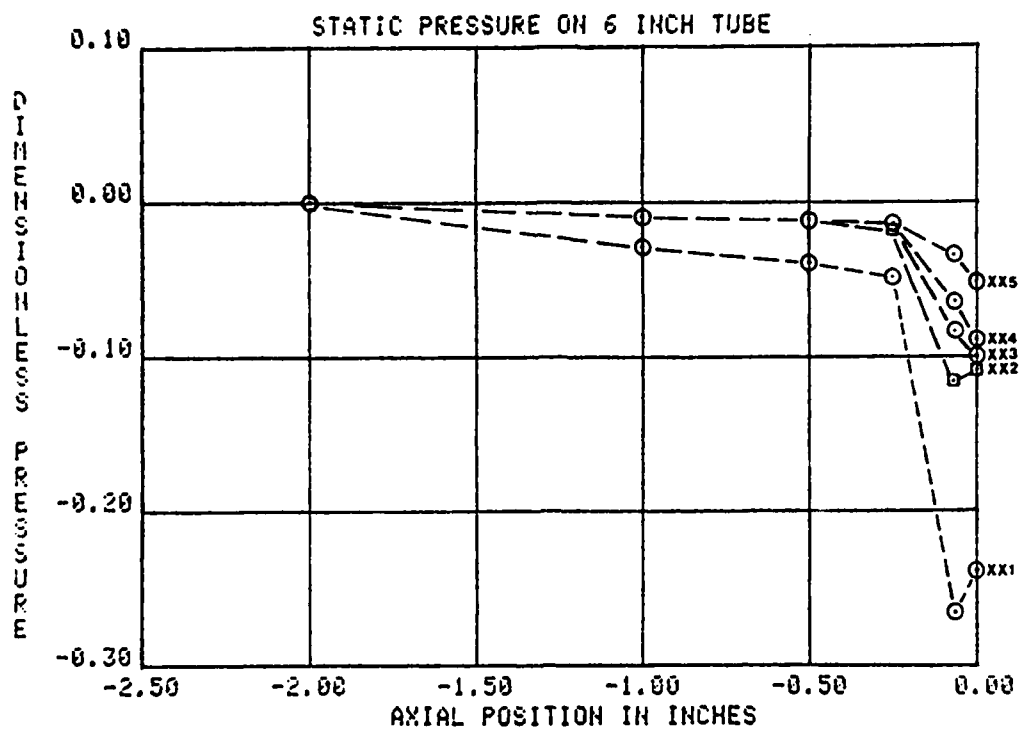
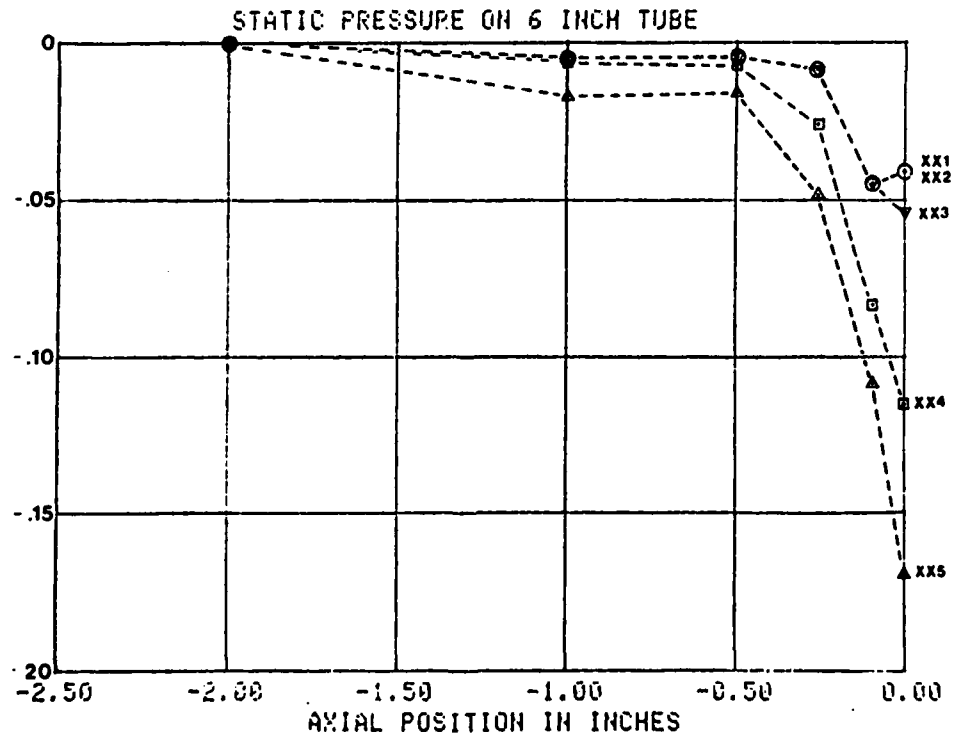
Figure 26. Dimensionless Pressure Based on  $\bar{V}$ Figure 27. Dimensionless Pressure Based on  $\bar{U}$

Table III  
COEFFICIENT OF FRICTION

Runs	Centerbody	Outside Wall
XX1	0.0016	0.0140
XX2	0.0031	0.0108
XX3	0.0059	0.0093
XX4	0.0048	0.0048
XX5	0.0043	0.0043

#### V. Conclusions and Recommendations

Experimental investigation of the flow field resulting from the mixing of incompressible co-annular air streams with substantial swirl present in the inner stream revealed a number of important fluid dynamic phenomena. The flow field is highly complex with significant radial and axial gradients in velocities, pressures, and momentum fluxes. The Rayleigh instability caused by the decrease in tangential momentum in the radial direction increases the mixing of the 2 streams.

On the basis of the experimental results, the following remarks can be made regarding the initial mixing region (for the swirl rates tested):

1. The growth rate of the half-radius of the swirl velocity,  $b$ , for the swirling annular free-jet is much lower than the growth rate of a swirling free-jet because of the swirling annular free-jet's region of recirculation, shown in Figure 2, and its effect on the flow.
2. The addition of a coflowing external stream to the swirling annular free-jet reduces the half-radius of swirl velocity,  $b$ , in the initial region (see Test 2 in Figure 23).
3. The addition of a centerbody to a swirling annular free-jet with coflowing external stream causes the

half-radius of the swirl velocity, b, to grow in the initial region (see Tests 2 and 3 in Figure 23).

4. The addition of an outside wall to a swirling annular jet with coflowing external stream and centerbody does not affect the growth rate of the half-radius of the swirl velocity, b, in the initial region (see Test 3 in Figure 23 and Test XX3 in Figure 20).
5. For concentric annular streams with a centerbody and an outside wall:

- a. an increase in the axial momentum of the outer stream reduces the radial transfer of tangential momentum and the rate of growth of the half-radius of the swirl velocity, b, and
- b. an increase in the velocity ratio (outside to inside velocity) increases the influence of the outside stream on upstream pressures on the outer wall of the inner annulus.

The author recommends that further experiments be conducted on the mixing of constant-area annular flows with swirl to widen the existing data base. These experiments should include

1. measurement of wall static pressures on all walls upstream of the test section,
2. measurement with different swirl ratios (tangential to axial velocity) of the inner stream, and
3. measurement of Reynolds shear stresses.

As further data becomes available on the behavior of confined flows with swirl, analytical methods must be developed to describe these flows.

A multi-hole pressure probe must be calibrated in strong velocity and static-pressure gradients before this measurement device can be used in

flows with higher swirl ratios. Research into the behavior of seven-hole pressure probes in severe velocity and temperature gradients is currently being conducted by the author.

### Symbols

#### English Symbols

b	half-radius of tangential velocity, location where velocity is 1/2 its maximum
$c_f$	coefficient of friction
D	diameter
$G_z$	axial momentum, defined by Eqn. (B18)
$G_\theta$	tangential momentum, defined by Eqn. (B12)
L	length
$M_z$	axial momentum flux, defined by Eqn. (B13)
$M_z'$	axial momentum flux, defined by Eqn. (1)
$M_\theta$	tangential momentum flux, defined by Eqn. (2)
$\dot{m}$	mass flow rate
P	pressure
Q	dynamic pressure ( $= 1/2 \rho \bar{V}^2$ )
r, R	radius
S	swirl number, defined by Eqn. (B16)
T	temperature
$\bar{U}$	average axial velocity in inner annulus
u	radial velocity
v	total velocity
$\bar{v}$	average axial velocity in test section
v	tangential velocity
w	axial momentum, defined by Eqn. (B13)
w	axial velocity

x  
y  
z }  
space coordinates

Greek Symbols

$\alpha$	angle of attack; mass flow ratio ( $= \dot{m}_0 / \dot{m}_1$ )
$\beta$	angle of sideslip
$\theta$	angle in cylindrical coordinate system
$\rho$	density
$\tau$	shear stress
$\psi$	incompressible stream function

Subscripts

i	inside
o	reference state; outside
s	static
t	total or stagnation property
z	axial
$\alpha$	angle of attack
$\beta$	angle of sideslip
$\theta$	tangential
0-5	referring to different locations in space

Superscripts

'	instantaneous variation
-	time average, spatial average

References

1. Schetz, J.A., Injection and Mixing in Turbulent Flow, Progress in Astronautics and Aeronautics, Vol. 68, American Institute of Aeronautics and Astronautics, New York, 1980.
2. King, M.K., R.R. Rothfus, and R.I. Kermode, "Static Pressure and Velocity Profiles in Swirling Incompressible Tube Flow," A.I.ChE. Journal, Vol. 15, No. 6, Nov. 1969, pp. 837-842.
3. Lilley, D.G., "Swirl Flows in Combustion: A Review," AIAA Journal, Vol. 15, No. 8, Aug. 1977, pp. 1063-1078.
4. Chigier, N.A. and J.M. Beer, "Velocity and Static-Pressure Distributions in Swirling Air Jets Issuing from Annular and Divergent Nozzles," Journal of Basic Engineering, Trans. ASME, Dec. 1964, pp. 788-796.
5. Chigier, N.A. and A. Chervinsky, "Experimental Investigation of Swirling Vortex Motion in Jets," Journal of Applied Mechanics, Trans. ASME, June 1967, pp. 443-451.
6. Fujii, S., K. Eguchi, and M. Comi, "Swirling Jets with and without Combustion," AIAA Journal, Vol. 19, No. 11, Nov. 1981, pp. 1438-1442.
7. Habib, M.A. and J.H. Whitelaw, "Velocity Characteristics of Confined Coaxial Jets with and without Swirl," Journal of Fluid Mechanics, Vol. 102, March 1980, pp. 47-53.
8. Ribeiro, M.M. and J.H. Whitelaw, "Coaxial Jets with and without Swirl," Journal of Fluid Mechanics, Vol. 96, Part 4, 1980, pp. 769-795.
9. Launder, B.E. and A. Morse, "Some Experiments on the Turbulent Swirling Jet with and without an External Stream," Unpublished Paper.
10. Erwin, J.R., "Experimental Techniques," Aerodynamics of Turbines and Compressors, High Speed Aerodynamics and Jet Propulsion, Vol. X, Section D, Princeton, 1964.
11. Barker, K., R. Gallington, and S. Minster, "Calibration of Five-Hole

- Probes for On-Line Data Reduction," Aeronautics Digest, Spring 1979,  
USAFA-TR-79-7, USAF Academy, CO, July 1979.
12. Dring, R.P., H.D. Joslyn, and L.W. Hardin, "Experimental Investigation  
of Compressor Rotor Wakes," United Technologies Research Center Report  
AFAPL-TR-79-2107, Jan. 1980.
13. Gallington, R.W. and C.F. Hollenbaugh, "A Fast Method for Accurate  
Manufacture of Small Five-Hole Probes," Aeronautics Digest, Spring 1979,  
USAFA-TR-79-7, USAF Academy, CO, July 1979.
14. Mattingly, J.D., "Experimental Investigation of the Mixing of Highly  
Swirling Flows," Dissertation, University of Washington, 1982.
15. Pratte, B.D. and J.F. Keffer, "The Swirling Turbulent Jet," Journal  
of Basic Engineering, Vol. 95, 1973.
16. Scott, C.J. and D.R. Rask, "Turbulent Viscosities for Swirling Flow in  
a Stationary Annulus," Journal of Fluids Engineering, Trans. ASME, Dec.  
1973, pp. 557-566.
17. Bird, R.B., W.E. Stewart, and E.N. Lightfoot, Transport Phenomena,  
Wiley, 1960.

Appendix A

EXPERIMENTAL RESULTS

The tables below contain the experimental data gathered in 5 sets of experiments. This data has been nondimensionalized for presentation and ease of analysis. The quantities used to nondimensionalize the data are shown in Table A1, while the values used to nondimensionalize the data and the average reference values for each test are presented in Table A2.

Table A1  
DIMENSIONLESS QUANTITIES FOR DATA PLOTS

Dimensional		Dimensionless Quantity
Symbol	Quantity	
w	Axial Velocity	$w/\bar{V}$
v	Tangential Velocity	$v/\bar{V}$
u	Radial Velocity	$u/\bar{V}$
V	Total Velocity	$V/\bar{V}$
$P_T$	Total Pressure	$(P_T - P_o)/Q$
$P_S$	Static Pressure	$(P_S - P_o)/Q$
P	Wall Static Pressure	$(P - P_o)/Q$
$M_z'$	Axial Momentum Flux	$M_z'/Q$
$M_\theta$	Tangential Momentum Flux	$M_\theta/Q$

$P_o$  = the static pressure on the outer wall of the inner stream at  
 $Z = -2$  inches

$Q$  = the dynamic pressure ( $= 1/2 \rho \bar{V}^2$ )

$\bar{V}$  = the average axial velocity in the test section

Table A2  
AVERAGE REFERENCE VALUES

Test	$\dot{m}_o + \dot{m}_i$ (lb/sec)	$\alpha$	$\bar{V}$ (ft/sec)	$P_o$ (psig)
XX1	.652	0	33	-0.010
XX2	.652	0.47	33	0.015
XX3	.652	1.0	33	0.016
XX4	.652	2.13	33	0.014
XX5	.652	3.91	33	0.008

Reference Density = 0.079 lbm/ft<sup>3</sup>

USAFA-TR-83-15

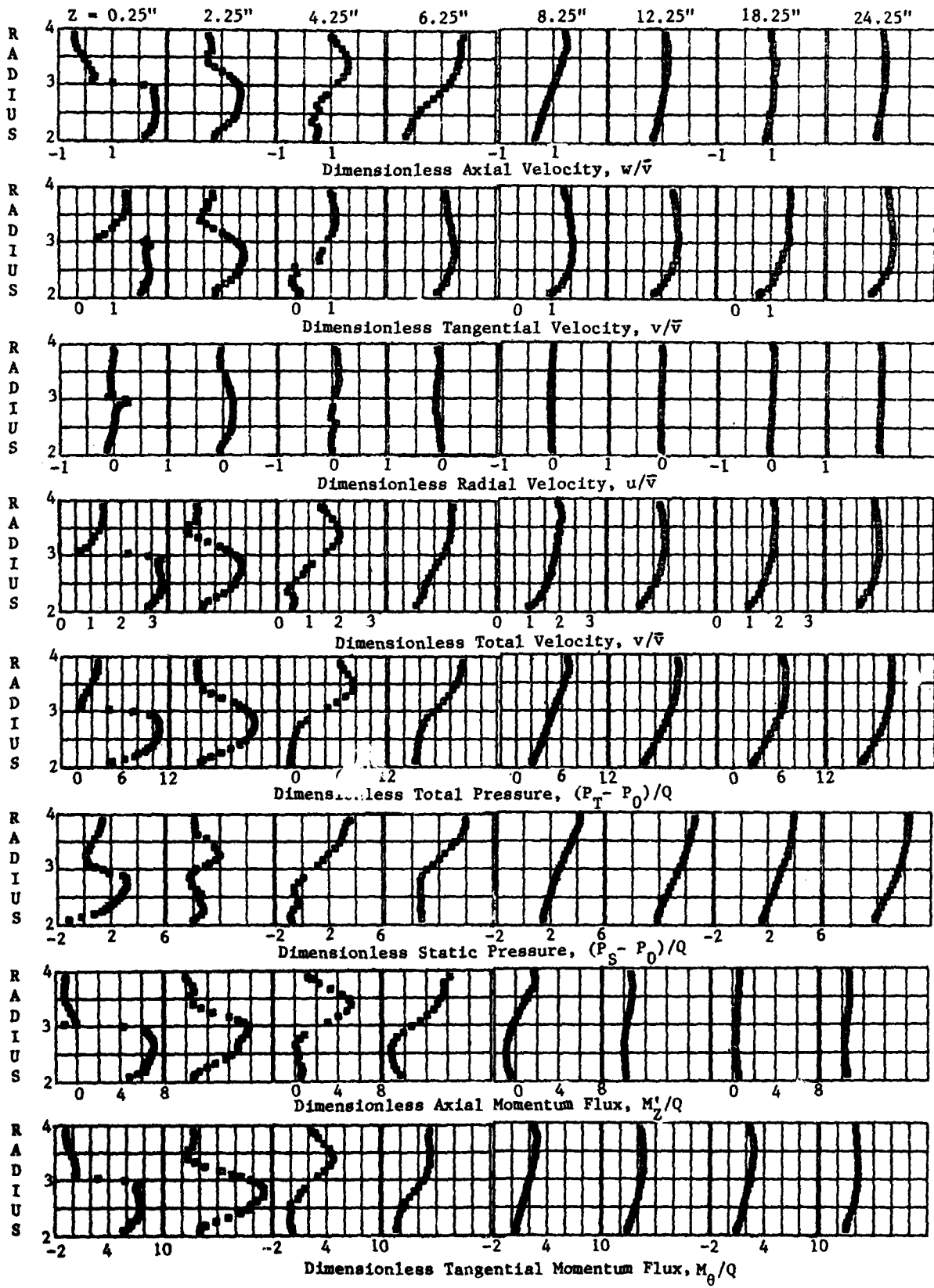


Figure A1. Test Runs XXI

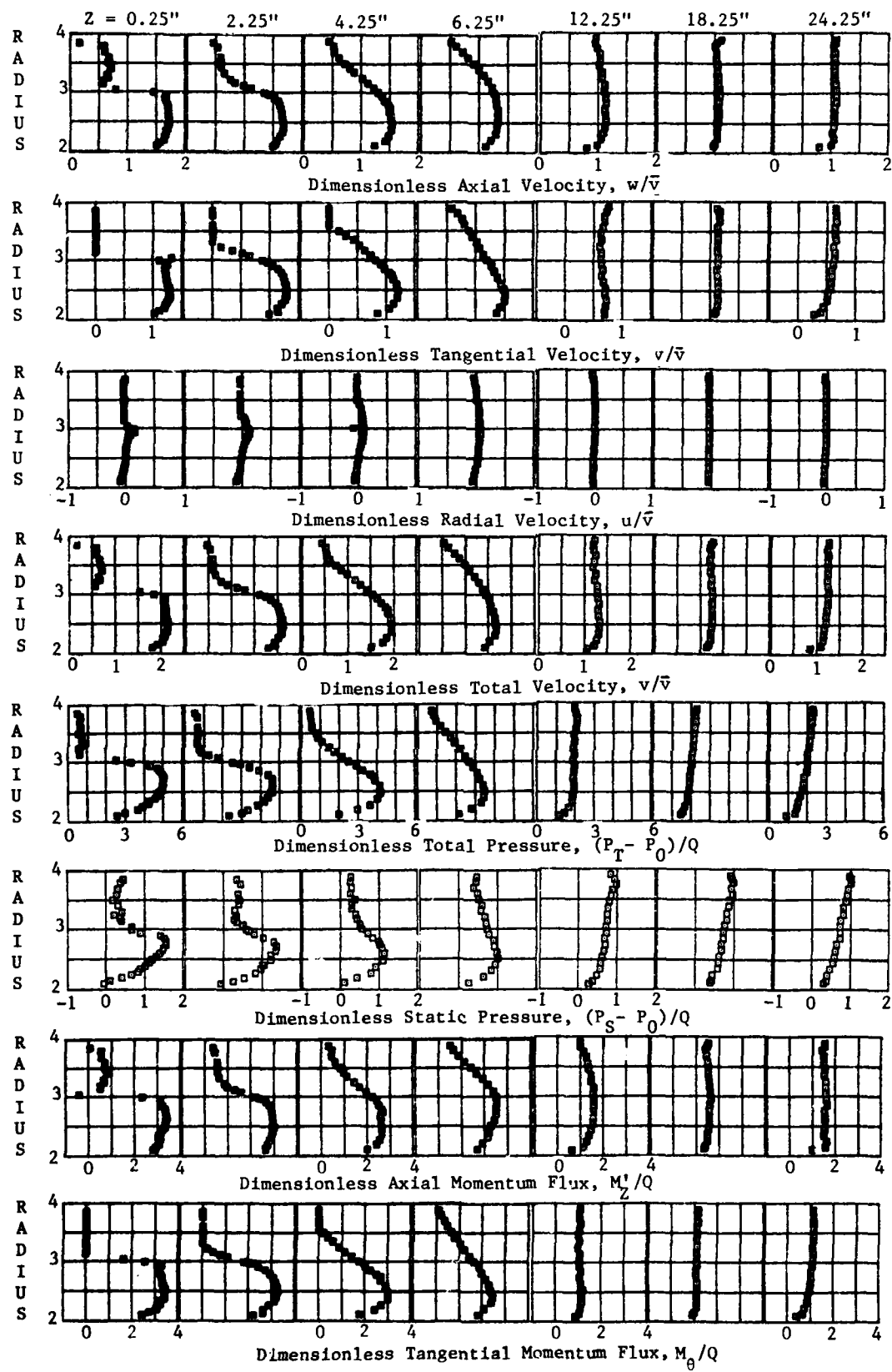


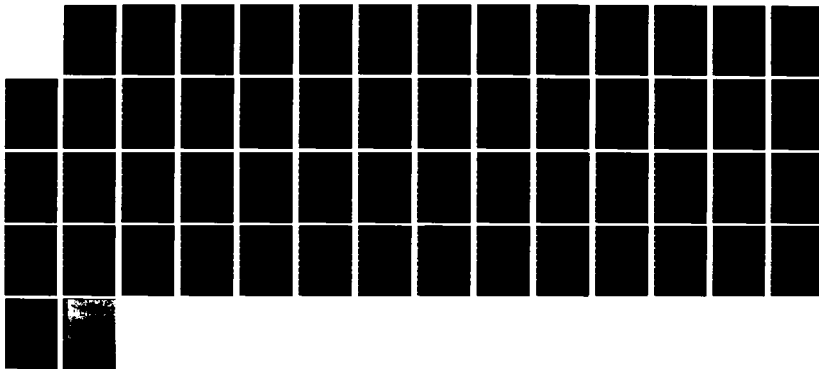
Figure A2. Test Runs XX2

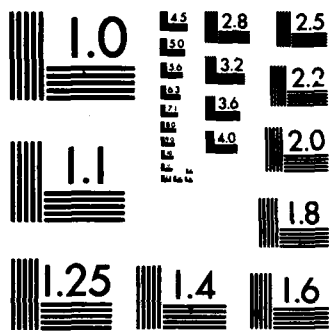
AD-A135 073 AIR FORCE ACADEMY AERONAUTICS DIGEST - FALL/WINTER 1982 2/2  
(U) AIR FORCE ACADEMY CO J DEJONGH ET AL. SEP 83  
USAFAS-TR-83-15

UNCLASSIFIED

F/G 20/4

NL





MICROCOPY RESOLUTION TEST CHART  
NATIONAL BUREAU OF STANDARDS-1963-A

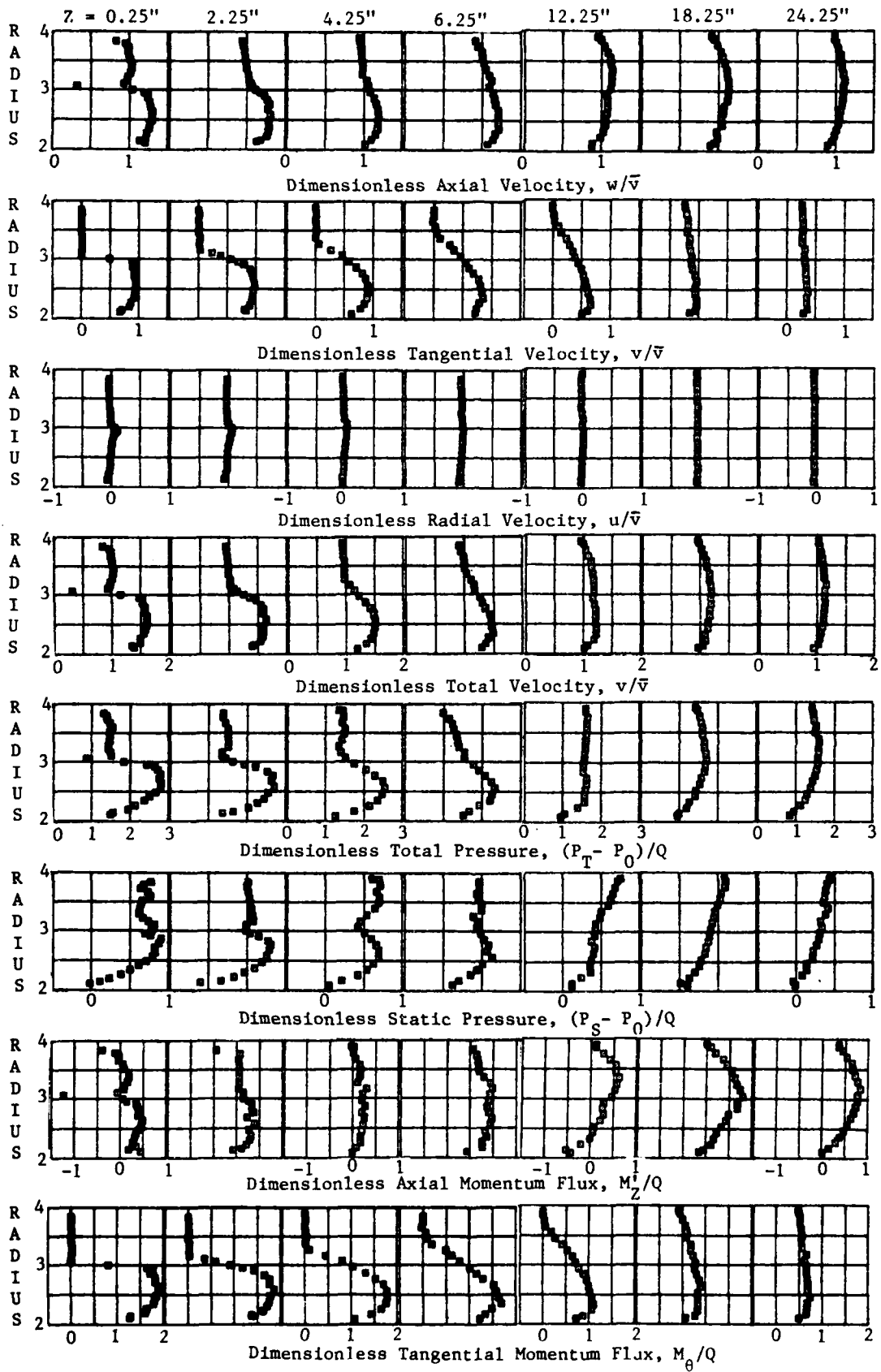


Figure A3. Test Runs XX3

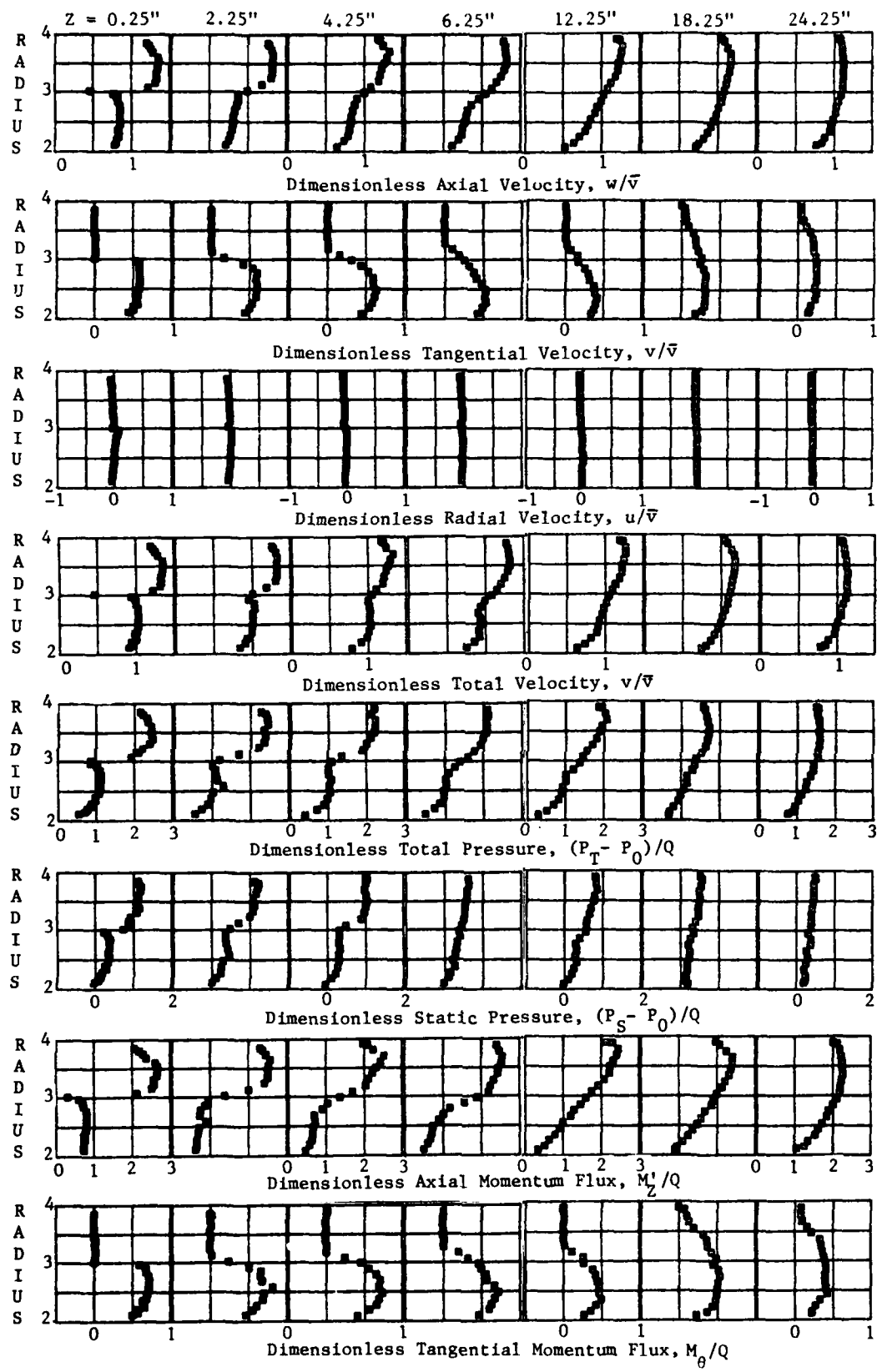


Figure A4. Test Runs XX4

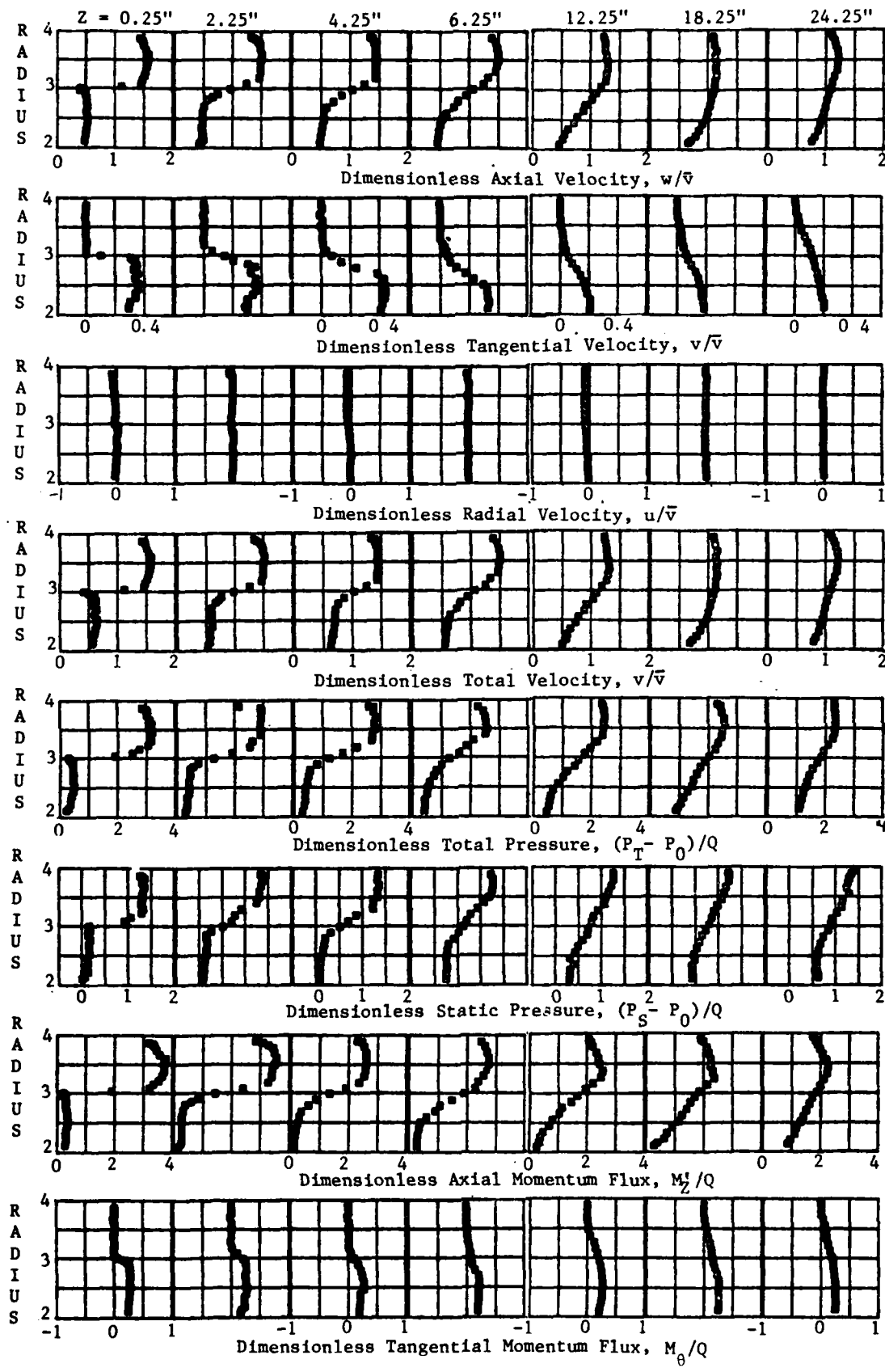


Figure A5. Test Runs XX5

Appendix B

DEVELOPMENT OF INTEGRAL RELATIONSHIPS FOR AXISYMMETRIC FLOW  
WITH SWIRL IN AN ANNULAR CHANNEL  
FORMED BETWEEN CONCENTRIC CONSTANT AREA CYLINDERS

I. Introduction

The annular channel and the nomenclature for axisymmetric flow are shown in Figure B1. Momentum integral relationships were developed to analyze experimental data obtained for this flow configuration.

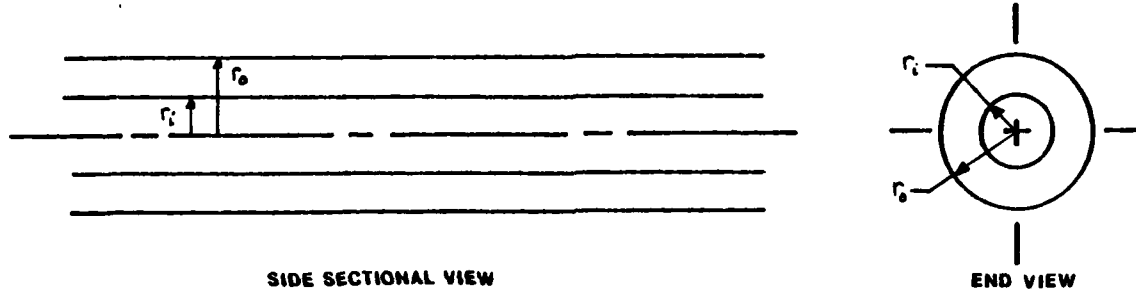


Figure B1. Annular Channel

II. Development of Integral Momentum Equations

For circular jets with or without swirl, the mean axial velocity ( $w$ ) is much greater than the mean radial velocity ( $u$ ), and gradients in the radial direction are much larger than those in the axial direction. Because the flow under consideration is for a nozzle Reynolds number greater than a few thousand, the viscous stresses are assumed to be much smaller than the corresponding turbulent shear stresses. Under these conditions, the time-averaged Navier Stokes equations yield the following relationships for incompressible flow:

$$-\frac{v^2}{r} = -\frac{\partial P}{\partial r} - \frac{1}{r} \frac{\partial}{\partial r} [r \overline{u'^2}] + \frac{\overline{v'^2}}{r} \quad (B1)$$

$$u \frac{\partial v}{\partial r} + \frac{uv}{r} + w \frac{\partial v}{\partial z} = - \frac{\partial}{\partial r} (\bar{u}'v') - 2 \frac{\bar{u}'v'}{r} - \frac{\partial}{\partial z} (\bar{v}'w') \quad (B2)$$

$$u \frac{\partial w}{\partial r} + w \frac{\partial w}{\partial z} = - \frac{\partial P}{\partial z} - \frac{1}{r} \frac{\partial}{\partial r} (\bar{r}u'v') - \frac{\partial}{\partial z} (\bar{w}'^2) \quad (B3)$$

where the prime ('') denotes the turbulent fluctuation, and the overbar denotes the time average of the quantity.

Because  $\partial(\bar{v}'w')/\partial z$  is very small in comparison with  $\partial(\bar{u}'v')/\partial r$ , it can be ignored in Eqn. (B2) above. If the turbulent normal stresses ( $\bar{u}'^2$ ,  $\bar{v}'^2$ , and  $\bar{w}'^2$ ) are ignored, and the turbulent shear stresses are denoted as

$$\tau_z = - \rho \bar{u}'w' \quad (B4)$$

$$\tau_0 = - \rho \bar{u}'v' \quad (B5)$$

then Eqns. (B1) through (B3) become

$$\frac{v^2}{r} = - \frac{1}{\rho} \frac{\partial P}{\partial r} \quad (B6)$$

$$u \frac{\partial u}{\partial r} + \frac{uv}{r} + w \frac{\partial v}{\partial z} = - \frac{1}{\rho} \frac{\partial \tau_\theta}{\partial r} + \frac{2}{\rho} \frac{\tau_\theta}{r} \quad (B7)$$

$$u \frac{\partial w}{\partial r} + w \frac{\partial w}{\partial z} = - \frac{1}{\rho} \frac{\partial P}{\partial z} + \frac{1}{\rho r} \frac{\partial}{\partial r} (r\tau_z) \quad (B8)$$

Integration of Eqn. (B6) with respect to the radius from the inner radius ( $r_i$ ) to a radius ( $r$ ) in the flow yields

$$P(r,z) - P(r_i,z) = \rho \int_{r_i}^r (v^2/r) dr \quad (B9)$$

Multiplying Eqn. (B7) by  $\rho r^2$  and integrating with respect to the radius from the inner radius ( $r_i$ ) to the outer radius ( $r_o$ ) yields

$$\frac{d}{dz} \left[ \rho \int_{r_i}^{r_o} r^2 wv dr \right] = (r^2 \tau_\theta) \Big|_{r_i}^{r_o} \quad (B10)$$

Multiplying Eqn. (B8) by  $\rho r$  and integrating with respect to the radius from the inner radius ( $r_i$ ) to the outer radius ( $r_o$ ) yields

$$\frac{d}{dz} \left[ \int_{r_i}^{r_o} (\rho + \rho w^2) r dr \right] = (r \tau_z) \Big|_{r_i}^{r_o} \quad (B11)$$

Eqns. (B10) and (B11) can be simplified further by defining the terms within each integral as follows.

$$G_\theta = \int_{r_i}^{r_o} \rho r^2 w v dr = \int_{r_i}^{r_o} M_\theta r^2 dr \quad (B12)$$

where  $M_\theta = \rho w v$

$$W = \int_{r_i}^{r_o} (\rho - \rho_0 + \rho w^2) r dr = \int_{r_i}^{r_o} M_z r dr \quad (B13)$$

where  $M_z = \rho - \rho_0 + \rho w^2$  and  $\rho_0$  is a reference pressure.

Using the above definitions of  $G_\theta$  and  $W$ , Eqns. (B10) and (B11) simplify to

$$\frac{dG_\theta}{dz} = (r^2 \tau_\theta) \Big|_{r_i}^{r_o} \quad (B14)$$

$$\frac{dW}{dz} = (r \tau_z) \Big|_{r_i}^{r_o} \quad (B15)$$

Eqns. (B14) and (B15) are the momentum relationships that can also be obtained by control volume analysis (Ref. 17). Eqn. (14) relates the change in the axial direction of the radially integrated angular momentum to the tangential shear stress at the walls. Eqn. (B15), on the other hand, relates the change in the axial direction of the radially integrated pressure plus axial momentum (total "stream thrust") to the axial shear stress at the walls.

### III. Swirl Number

The swirl number for a flow is the ratio of the angular momentum to the total "stream thrust" times an appropriate radius. It is a dimensionless number that is used to characterize flows containing swirl. The exact form of the equation used to calculate the swirl number varies between references (see Refs. 1 and 8). The swirl number ( $S$ ) can be defined as

$$S = G_\theta / (r_o W) \quad (B16)$$

where  $G_\theta$  and  $W$  are defined by Eqns. (B12) and (B13), respectively, and  $r$  is the outer radius of the annular channel. As defined above, the swirl number is constant in the axial direction when the shear stresses at the wall are negligible.

An alternate definition of the swirl number ( $S$ ) can be obtained by noting that Eqn. (B13) can be integrated by parts to give

$$W = \int_{r_i}^{r_o} (P - P_o + \rho w^2) r dr$$

$$w = \frac{(P - P_o)r^2}{2} \Big|_{r_i}^{r_o} + \int_{r_i}^{r_o} \rho(w^2 - v^2/2) r dr \quad (B17)$$

When the axial momentum,  $G_z$ , is defined as

$$G_z = \int_{r_i}^{r_o} \rho(w^2 - v^2/2) r dr = \int_{r_i}^{r_o} M'_z r dr \quad (B18)$$

where  $M'_z = \rho(w^2 - v^2/2)$ , then Eqn. (B17) becomes

$$W = G_z + \frac{(P - P_o)r^2}{2} \Big|_{r_i}^{r_o} \quad (B19)$$

The swirl number ( $S$ ) can then be defined as follows

$$S = \frac{G_\theta}{r_0 G_z + (r_0/2) \left[ (P_{r_0} - P_0)r_0^2 - (P_{r_1} - P_0)r_1^2 \right]} \quad (B20)$$

where  $G_\theta$  and  $G_z$  are defined by Eqns. (B12) and (B18), respectively.  $P_{r_0}$  and  $P_{r_1}$  are the wall static pressures at  $r = r_0$  and  $r = r_1$ , respectively;  $P_0$  is a constant reference pressure; and  $r_1$  and  $r_0$  are the inner radius and the outer radius of the annular channel, respectively.

Eqn. (B20) for the swirl number ( $S$ ) is more desirable to work with than Eqn. (B16) because the integrals for determining  $G_\theta$  and  $G_z$  contain only the axial velocity,  $w$ , and the tangential velocity,  $v$ , whereas Eqn. (B16) for the swirl number ( $S$ ) requires that the static pressure ( $P$ ) in the flow be integrated between the inner and outer wall for the calculation of  $W$  [Eqn. (B13)]. Since present measurement methods permit a more accurate measurement of the wall static pressure than the static pressure in the flow, Eqn. (B20) yields a more accurate value of the swirl number ( $S$ ).

Eqn. (B20) for the swirl number ( $S$ ) can be simplified when it is applied to a swirling stream flowing into a space of uniform pressure,  $P_0$ . When a centerbody is present, the swirl number is given by

$$S = \frac{G_\theta}{r_0 G_z + (r_0/2) (P_0 - P_{r_1}) r_1} \quad (B21)$$

where  $r_0$  is the outer radius of the stream at its exit,  $r_1$  is the radius of the centerbody,  $P_0$  is the ambient pressure, and  $P_{r_1}$  is the wall static pressure on the centerbody. When no centerbody is present, the swirl number is given by

$$S = G_\theta / (r_0 G_z) \quad (B22)$$

where  $r_0$  is the outer radius of the stream at its exit.

**SECTION IV**

**Thermodynamics and Heat Transfer**

NEW CONTROLS FOR ADVANCED RESIDENTIAL HEATING SYSTEMS

Robert C. Winn\*

**Abstract**

Solar heating systems and heating systems capable of storing low-cost, off-peak electrical energy can reduce the cost of heating a residence. But the conventional control strategies used with these systems often do not reduce the system's peak electrical power needs. In this paper, I describe the development of optimal control strategies for use with these heating systems. These strategies can be approximated by easily implemented proportional strategies, shown by computer simulation to significantly reduce the operating cost of the systems. Widespread use of the proportional strategies will considerably reduce the maximum electrical power required.

I. Introduction

Consumers ultimately pay for all of the costs associated with the generation of electricity. These costs fall into 2 categories, fuel and demand. Fuel costs are determined by the amount of coal or oil burned in the power plants. Demand costs are determined by the rate at which energy is used. The costs associated with purchasing and maintaining electrical generating equipment are examples of demand costs. These costs can be very high, because the utility must have enough generating capacity to satisfy the largest instantaneous power requirement (the peak demand) it will ever experience. If this peak demand occurs only rarely, some of the utility's generating equipment is used only rarely, so the demand cost must be high in order to pay back the investment on this equipment. Each consumer's electric bill is his or her part of the utility's fuel and demand costs, that is, the utility's "cost of supply."

To compute a consumer's share of the utility's cost of supply, we must consider 3 items: the amount of energy used, the rate of consumption, and when it is used. The amount of energy and the rate of

---

\*Major, USAF, Associate Professor of Aeronautics, DFAN

use correspond to fuel and demand costs, respectively. The time of day when the energy is used determines multipliers which are applied to each of those costs. Late at night, when the utility's electrical generating requirement (its load) is very low (the off-peak period), the multipliers are low. On the other hand, during the late afternoon, when the utility's load is high (the on-peak period), the multipliers are high. Two consumers using the same amount of energy with the same peak demand would have significantly different shares of the utility's cost of supply if one confined his use of electricity to the evening (when the multipliers are low) while the other confined his use of electric to the afternoon (when the multipliers are high).

With the consumer's share of the utility's cost of supply in mind several residential heating systems have recently been designed to reduce the cost of heating a home electrically. Of these, solar heating systems and off-peak energy-storage heating systems are the most promising. Solar heating systems reduce fuel costs by replacing electrical energy with collected solar energy. Off-peak energy-storage heating systems reduce heating costs by storing energy bought from the utility during the utility's off-peak period and then using the stored energy for heating the residence during the utility's on-peak period. The use of either system should result in low demand costs. However, the conventional control strategy for these systems uses energy in storage as it is needed to keep the residence warm. But this strategy does not address the situation in which the energy storage is depleted before the end of the utility's on-peak period. If this depletion should occur, the backup heating system must come on, a situation that these heating systems are supposed to avoid. Thus, the conventional control strategy does not achieve the full potential of either system.

for cost of supply reduction.

The purpose of this study is to develop and evaluate improved control strategies for the heating systems mentioned above. A control strategy is a regulation of the use of energy in storage. To develop new control strategies, I used an optimization technique that can be applied to time-varying systems. The control strategies resulting from this optimization give an upper limit on the performance of the systems. Unfortunately, these optimal control strategies are impossible to implement in a practical controller. Therefore, I developed easily implemented approximations to the optimal control strategies. These approximations are called proportional control strategies. The conventional, proportional, and optimal control strategies were evaluated using a computer program developed for the Electric Power Research Institute (EPRI) by Arthur D. Little, Inc. The program, "EPRI Methodology for Preferred Solar Systems" (EMPSS), performs detailed simulations of the operations of the various heating systems. In addition, the program uses the results of the simulation to determine the cost of supply of electricity for that residence (Ref. 1). The cost-of-supply calculations used data appropriate for the Public Service Company of New Mexico (Albuquerque) for the year 1990 (Ref. 2). I also used the results of the EMPSS simulations to estimate the effect on the utility of widespread use of the heating systems and control strategies studied in this paper.

## II. System Descriptions

For this study, I considered 3 residential heating systems: a baseline electric resistance heating system, an off-peak storage heating system, and a solar heating system. Each is used to satisfy the space-heating and domestic hot-water requirement of a well-insulated,

single-story residence. The baseline system provides back-up heating for the other systems. Schematic diagrams of the systems are shown in Figure 1.

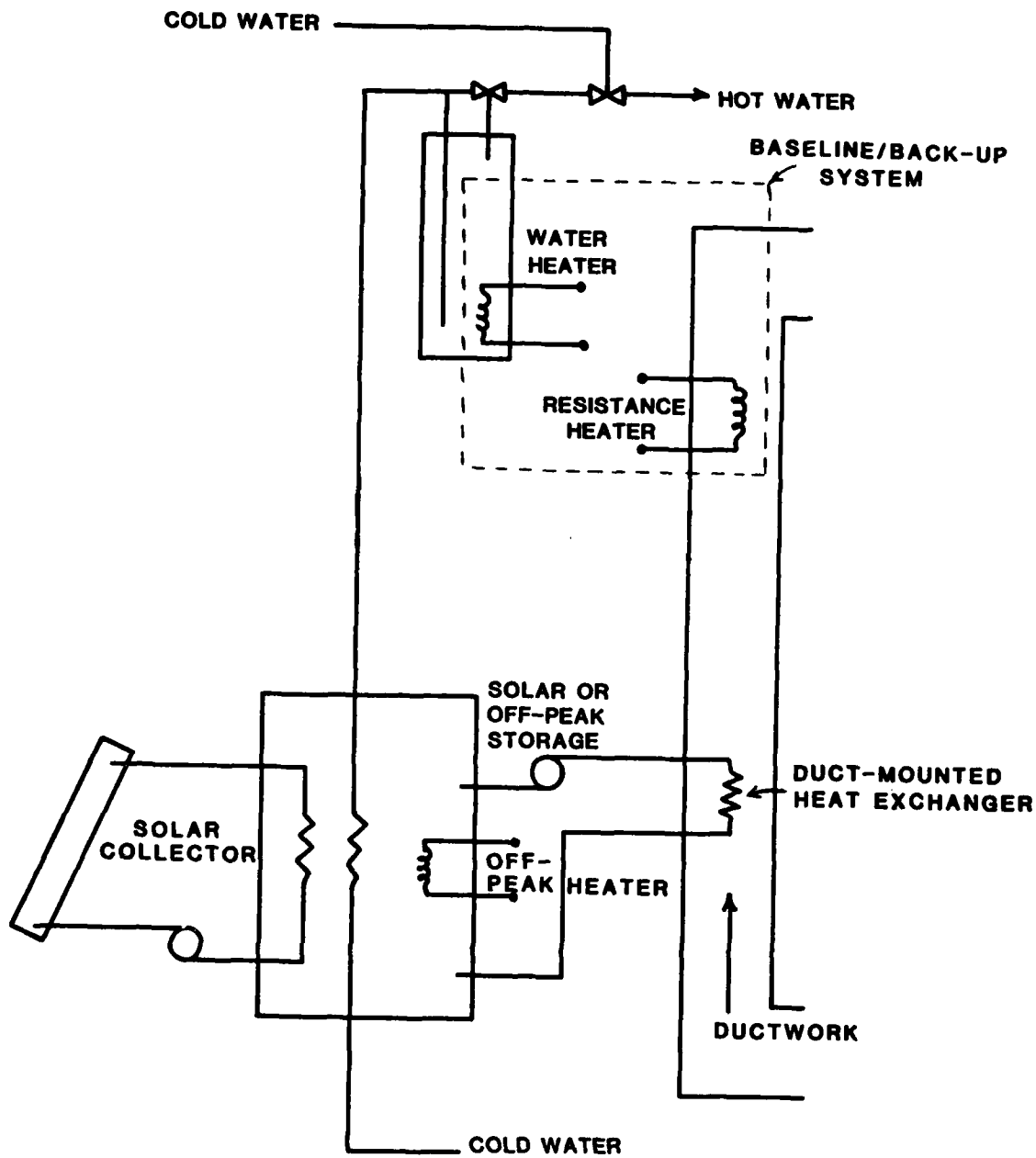


Figure 1. Schematic of Solar and/or Off-Peak Systems

The baseline system provides a basis for comparison with the other systems. It supplies energy to the residence by means of a duct-mounted electric resistance heater. The energy is distributed by forced air, and the system is controlled by a room thermostat.

The off-peak storage heating system consists of a water storage tank and a circulating pump. The conventional operating procedure is to heat the storage water to 140 degrees F when the utility's off-peak period begins and then, during the utility's on-peak period, to use the stored energy to satisfy the residence's heating and domestic hot water energy needs until the water in storage has reached 90 degrees F.

The solar heating system is composed of solar collectors, circulating pump, and water storage tank. Energy is collected and stored whenever possible. The conventional control strategy is to supply energy for both heating and domestic hot water whenever the storage temperature rises above 90 degrees F.

The limiting temperatures in the storages, 90 degrees F and 140 degrees F, are typical for the systems described above. If different temperatures had been used, the numerical results shown later in this paper would be different, but the conclusions would be identical.

### III. Control Strategies

The conventional strategy for energy discharge from off-peak or solar storage is to use the energy in storage to satisfy the heating and hot-water load until the temperature in storage is reduced to 90 degrees F. But there is a problem with this strategy. If the available energy in storage is depleted before the end of the utility's on-peak period, a large coincident demand may result. By coincident demand, I mean the electrical power required during the utility's on-peak period. This situation is illustrated in Figure 2, which shows the electrical demand

for a residence in Albuquerque, New Mexico, for a day when the utility experiences its maximum systemwide load for the heating season.

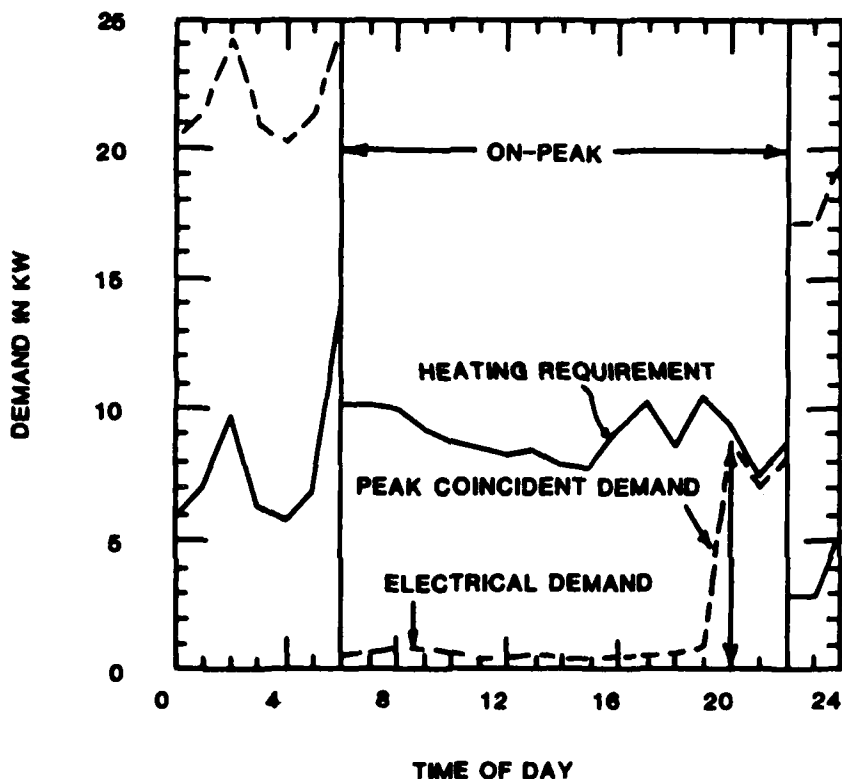


Figure 2. Conventional Strategy for Off-Peak Storage on the Utility's Peak Load Day

By 2000 hours (10:00 pm), the available internal energy from storage has been depleted, resulting in an electrical demand of approximately 9 kW at the residence. The fuel cost of supply for energy supplied by the utility on that day is shown in Figure 3 (Ref. 2).

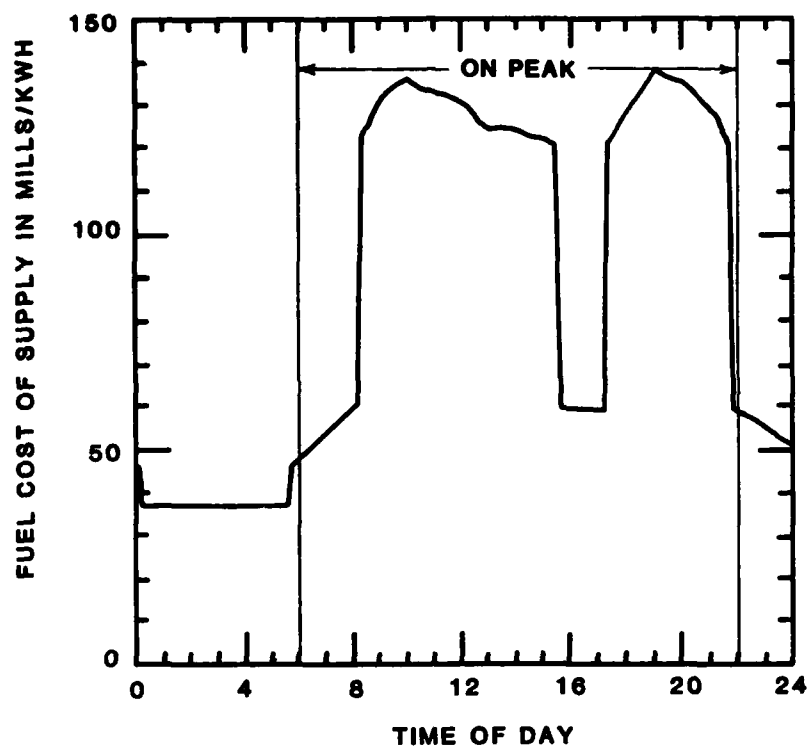


Figure 3. Fuel Cost of Supply on the Utility's Peak Load Day

The residential demand (Figure 2) is quite large at the same time that the cost of supply (Figure 3) is high. Clearly, the use of the off-peak storage system with conventional control has not resulted in a significant decrease in the power generation required of the utility. But an improved control strategy can significantly reduce the coincident demand and consequently reduce the maximum power required of the utility.

To determine the best control strategy for the discharge of off-peak or solar storage, we can use the methods of dynamic optimization, specifically Pontryagin's Maximum Principle (Ref. 3). I formulated the optimization problem to determine the on-peak power

requirement,  $\dot{Q}_{\text{on-peak}}$ , to minimize

$$J = \int_{t_0}^{t_f} [\dot{Q}_{\text{on-peak}}(t)]^2 dt \quad (1)$$

where

$t_0$  is the time at the start of the on-peak period,

$t_f$  is the time at the end of the on-peak period, and

$\dot{Q}_{\text{on-peak}}$  is the on-peak electrical power requirement.

This objective function [Eqn. (1)] is subject to constraints which, in this case, are the energy balances on the residence and storage (as modeled in Figure 4),

$$C_e dT_e / dt = \dot{Q}_{\text{on-peak}} + \dot{Q}_{\text{st}} - \dot{Q}_{\text{load}} \quad (2)$$

$$C_s dT_s / dt = \dot{Q}_{\text{sol}} - \dot{Q}_{\text{st}} - \dot{Q}_{\text{loss}} \quad (3)$$

where

$C_e$  is the thermal capacitance of the enclosure (residence) (kJ/°C),

$T_e$  is the temperature of the enclosure (residence) (°C),

$\dot{Q}_{\text{st}}$  is the rate of energy removal from storage (kW),

$\dot{Q}_{\text{load}}$  is the heating requirement of the enclosure

(residence) (kW),

$C_s$  is the thermal capacitance of the storage (kJ/°C),

$T_s$  is the storage temperature (°C),

$\dot{Q}_{\text{sol}}$  is the rate of supply of solar energy to storage (kW),

and

$\dot{Q}_{\text{loss}}$  is the rate of energy loss from storage (kW).

These equations are determined from energy balances on the residence and the storage, as modeled in Figure 4. Minimizing  $J$  will minimize the product of coincident demand ( $\dot{Q}_{\text{on-peak}}$ ) and on-peak energy consumption ( $\dot{Q}_{\text{on-peak}} dt$ ) while satisfying the energy balance equations that describe the temperature history of the residence and the storage. EMPSS and most other detailed simulations use a much more elaborate system of equations, but the purpose of those simulations is to provide accurate load and temperature histories. In fact, the purpose of this optimization problem is to develop an analytical expression for the optimal rate of energy discharge from storage and, as such, the dynamic equations above are quite adequate. Once the optimal control strategy is determined, it may then be programmed into the more detailed EMPSS simulation to determine its effect on the utility's cost of supply.

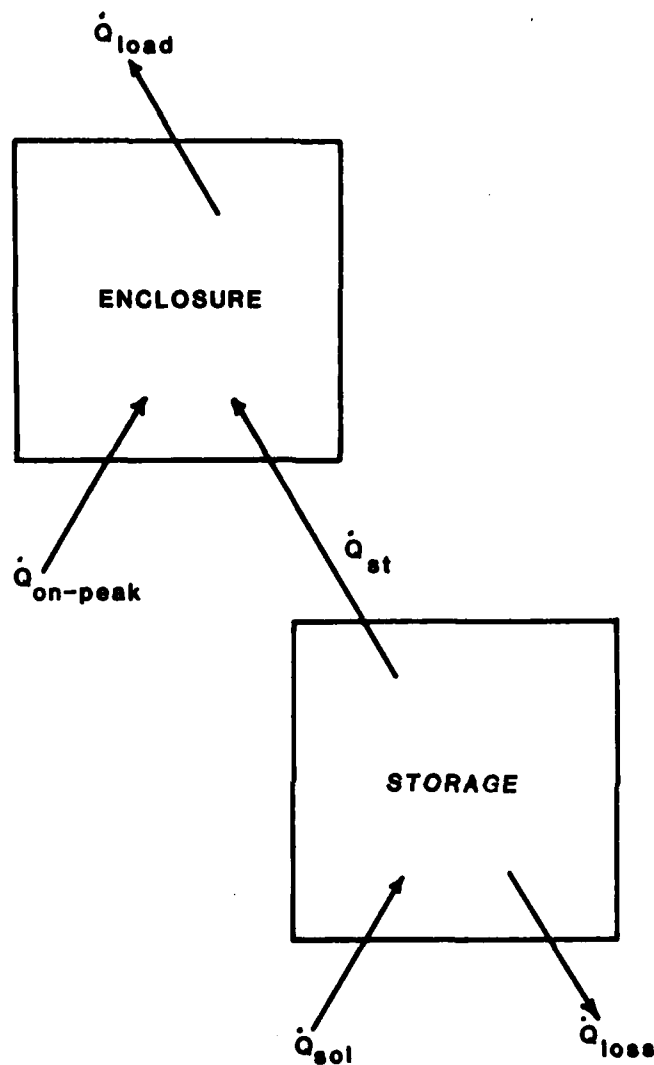


Figure 4. Off-Peak and/or Solar Heating System Schematic

Several reasonable assumptions make this problem a very straightforward one to solve. First, in a well-designed heating system, the storage losses are small and can safely be ignored in formulating a control strategy. Second, the enclosure temperature is held nearly

constant during the on-peak period by the thermostat in the enclosure. Certainly, when many residences are considered, the utility sees the enclosure temperature as constant, and, therefore, the time derivative of enclosure temperature is effectively zero. Third, the initial and final storage temperatures can be specified. The storage temperature at  $t_0$  is the maximum storage temperature (140 degrees F in this study). The temperature at  $t_f$  is the temperature  $T_{s,min}$ , below which the circulating pump is deactivated (90 degrees F in this study). With these assumptions, the problem can be solved. The details of the solution and a complete justification of the assumptions may be found in Ref. 4. The resulting optimal discharge rate is

$$\dot{Q}_{st}^* = \bar{\dot{Q}}_{load} + \bar{\dot{Q}}_{sol} + C_s(T_s - T_{s,min}) / (t_f - t_0) \quad (4)$$

where the overbar indicates the average over the entire on-peak period.

Implementation of this optimal control strategy requires knowledge of the current instantaneous heating requirement, the total energy requirement during the remainder of the on-peak period, and, in the case of solar heating, the total amount of solar energy to be delivered to storage during the on-peak period. Although this knowledge is impossible to achieve with complete accuracy, we can easily determine an approximation of the optimal control strategy by estimating the load and the solar energy collection. For example, if the load is modeled as constant throughout the on-peak period, and if it is assumed that no solar energy will be collected during this period, the approximation to the optimal discharge rate from storage is

$$\dot{Q}_{st} = C_s(T_s - T_{s,min}) / (t_f - t_0) \quad (5)$$

This approximation is called the proportional discharge strategy.

#### IV. Simulation Results

The performance of the selected systems under 3 control strategies was compared using the EMPSS computer program. As mentioned earlier,

implementation of the optimal control strategy in the computer simulation requires information not normally available. I was able to acquire this information, however, by saving the heating loads and the solar energy collection rates calculated by EMPSS in a simulation using the conventional control strategy. This data was then used to calculate the optimal control strategy. Although this technique is not a practical implementation procedure, it does provide an upper limit to the performance of the different systems against which the performance under conventional and proportional control can be compared.

#### A. Off-Peak Storage Heating System

Table I presents the peak coincident demand for the peak heating months (December, January, and February) and the associated costs of supply that result from using conventional, proportional, and optimal discharge of off-peak storage for the entire year of 1990.

In January and February, both the proportional and optimal control strategies reduced the peak coincident demand to a level lower than that achieved by the conventional control. In December the total on-peak heating load never exceeded the energy storage capacity, so the system performances are identical, regardless of control strategy. The use of the optimal control strategy, as expected, results in the best system performance and the lowest cost; however, the performance is only slightly better than if proportional control were used.

As mentioned earlier, implementation of the optimal control strategy requires some knowledge of the future. For a typical day, one can estimate this required information quite well by using a curve fit of the average weather data or some other modeling technique; however, the monthly peak coincident demand does not occur on a typical day. Rather, it occurs on the day that has the largest instantaneous heating

requirement,  $Q_{load}$ , during the on-peak period. An analysis of the Albuquerque weather shows that these "worst" days have outdoor temperatures that are low and nearly constant all day long. This means that the  $Q_{load}$  is relatively constant throughout the on-peak period. Therefore, a best fit of weather data will not be adequate to accurately predict the time-varying heating requirement on the "worst" days. Because the proportional control strategy assumes a constant heating requirement, this strategy results in heating costs similar to those of the optimal control strategy, as shown by the results in Table I.

Table I.  
OFF-PEAK STORAGE DISCHARGE STRATEGY COMPARISONS

	Baseline Heating System	Off-Peak Storage System		
		Conventional Strategy	Proportional Strategy	Optimal Strategy
December Peak Coincident Demand	7.28 kW	.63 kW	.63 kW	.63 kW
January Peak Coincident Demand	13.32 kW	12.61 kW	5.59 kW	3.60 kW
February Peak Coincident Demand	12.32 kW	10.33 kW	4.59 kW	3.49 kW
Coincident Demand Annual Cost of Supply in 1990 Dollars & % of Baseline	\$2551 100%	\$1340 53%	\$783 31%	\$658 26%
Fuel Annual Cost of Supply in 1990 Dollars & % of Baseline	\$1396 100%	\$979 70%	\$913 65%	\$909 65%
Total Annual Cost of Supply in 1990 Dollars & % of Baseline	\$3946 100%	\$2319 59%	\$1697 43%	\$1567 40%

Figures 2, 5, and 6 depict the heating requirement and the electrical demand necessary to satisfy it for conventional, proportional, and optimal control strategies, respectively, on the day when the highest utility load for the entire heating season occurred. The use of the conventional strategy results in a large coincident demand at 2000 hours (8:00 pm) because storage was depleted before the end of the on-peak period. The use of proportional control strategy ensures that energy will be left in storage for use at the end of the on-peak period, so no large coincident demand occurs. The same is true of the optimal control.

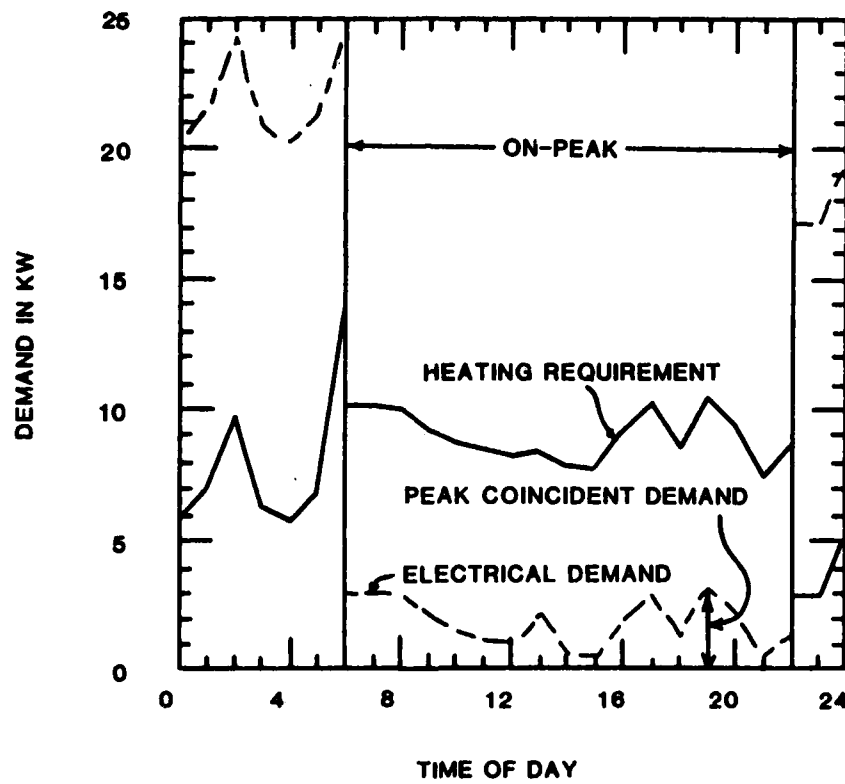


Figure 5. Proportional Strategy for Off-Peak Storage on the Utility's Peak Load Day

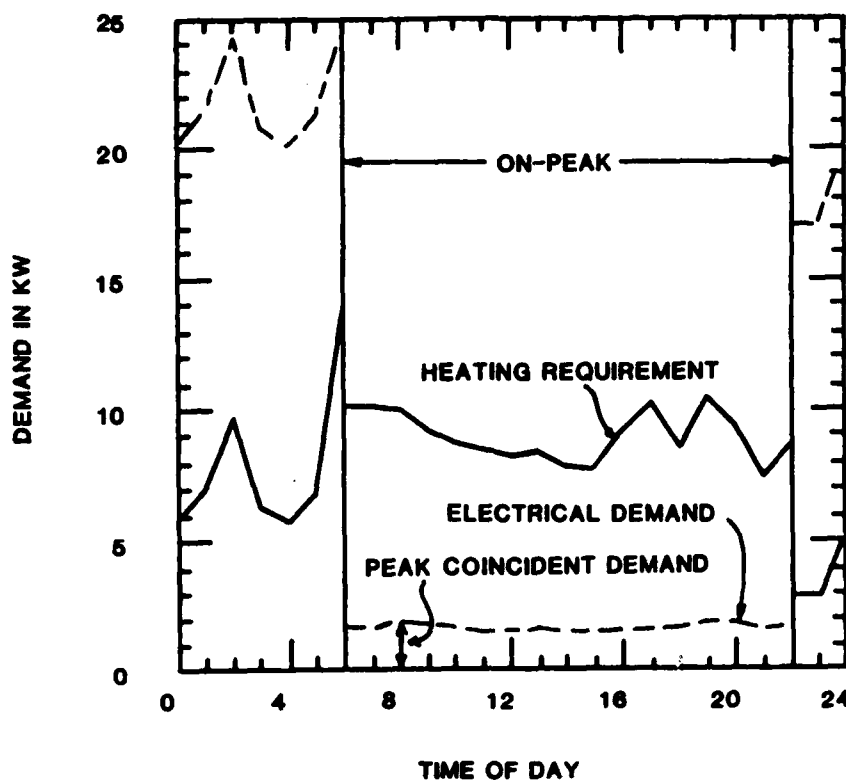


Figure 6. Optimal Strategy for Off-Peak Storage on the Utility's Peak Load Day

The proportional control strategy achieved the greatest monthly reduction in peak coincident demand in January. In fact, when the proportional control strategy is used, some reduction in coincident demand will occur any time the storage is not sufficient to meet the heating requirement. During the spring and fall, the heating load is so small and the storage so large that any strategy will satisfy the entire on-peak load.

Although the optimal discharge from storage resulted in the lowest utility cost of supply, implementation of that control requires exact

knowledge of the heating rates for the upcoming day. Implementation of the proportional strategy, on the other hand, does not require any capability to predict loads. If relatively accurate load prediction were available, one would expect the performance to be better than that of the proportional strategy but still not as good as that of the optimal strategy. To determine how accurate the load prediction must be to improve upon the performance of the proportional strategy, simulations were performed with known errors in the heating rate predictions used to determine the control. I assigned a specified error to each hourly heating rate. The results of the year-long simulations appear in Figure 7.

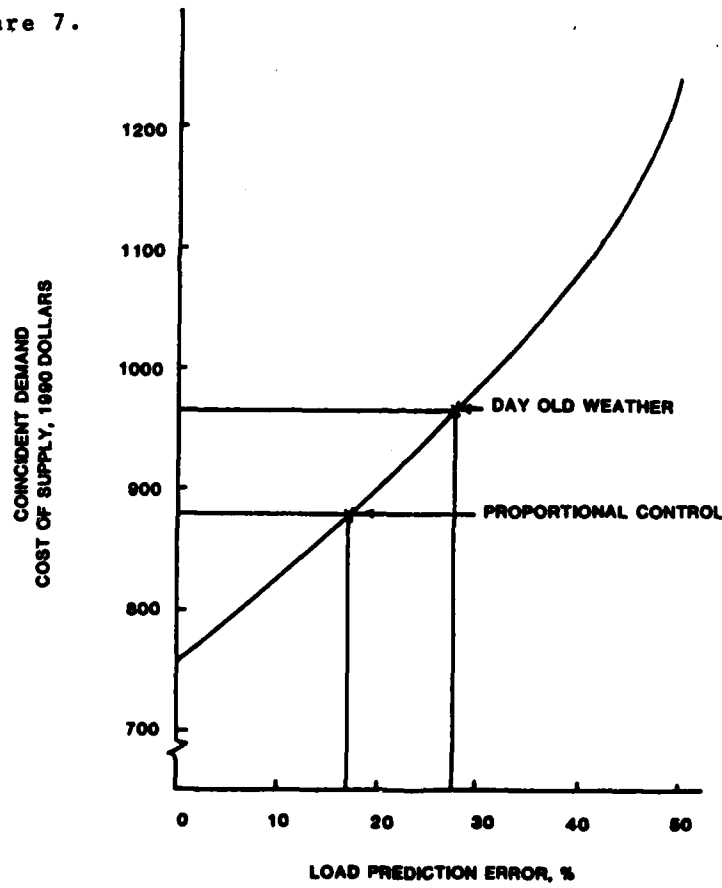


Figure 7. Influence of Load Prediction Error on Coincident Demand Cost of Supply

The coincident demand cost of supply which resulted from the use of proportional discharge corresponds to a load prediction error of about 17 percent. By contrast, using a control strategy that assumes that today's weather will be the same as yesterday's is equivalent to a load prediction error of 28 percent. It is difficult and therefore expensive to achieve a load prediction error lower than 17 percent.

#### V. Utilitywide Impact

The widespread use of the proportional control strategy would significantly affect the utility. I made an assessment of this impact by assuming that 66,000 new homes would be built in the Albuquerque service area from 1981 to 1990. Table II summarizes this data, presenting the cumulative effect of the use of many off-peak storage heating systems. In reviewing the table, assume that the off-peak storage heating systems will replace conventional resistance heating.

Table II  
UTILITY IMPACT ASSESSMENT

Market Saturation	Delta Energy, MWh	Delta Demand Cost	Delta Fuel Cost	Delta Cost of Supply	Delta Demand Peak, MW
100%	35,100	-117	-32	-147	-61
50%	17,600	- 58	-16	- 74	-31
25%	8,800	- 29	- 8	- 37	-15

Note: Costs are in millions of 1990 dollars.

In Table II, Delta Energy is the net change in the energy consumption resulting from use of the system for one year. This term is positive

because off-peak storage systems use more energy than conventional systems. The Delta Cost Values presented are in millions of 1990 dollars. The negative values indicate annual savings. The Delta Demand Peak is the change in the utility demand at the hour of the annual peak utility demand. The market saturation is the percentage of new homes that use the system in question.

The information presented in Table II was generated by assuming a linear relationship between market saturation and the quantities listed, but this pattern is not accurate for high market saturation. In fact, in this study, with a market saturation of 16 percent, the systemwide load decreased during the day and increased at night until the peak loads were equal. Any market saturation beyond 16 percent will increase the systemwide load, despite the decrease in the daytime load, because the nighttime load continues to increase.

The use of many off-peak storage systems will affect systemwide load (particularly on peak load days). Figures 8 and 9 show this effect for a peak load day. In Figure 8, the solid line is the expected load curve for the peak load day in January; the dashed line is the load curve if 16 percent of the new homes use off-peak storage with the conventional discharge strategy. Notice that the 2 curves are identical for the last few hours of the on-peak period. The change in the utility load curve (if 16 percent of the new homes use proportional discharge of off-peak storage) is presented in Figure 9. The demand at the end of the on-peak period is significantly less than the value resulting from the use of the conventional control.

#### B. Solar Heating System

The conventional strategy for the discharge of solar storage is to use energy from storage if it is available, but little thought has

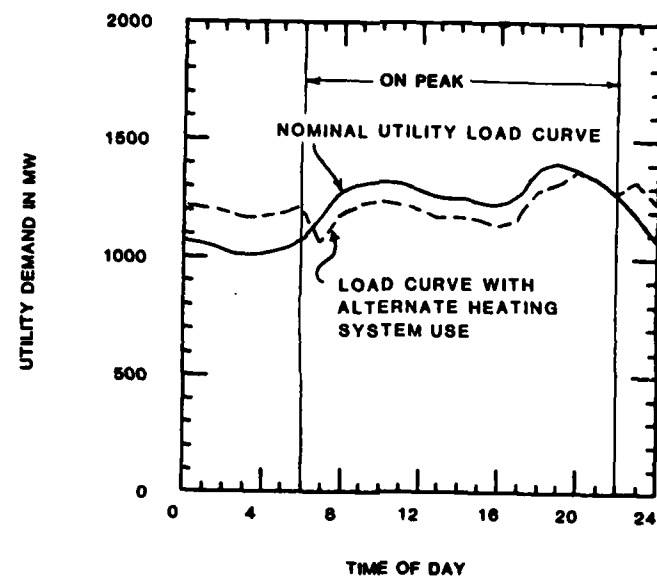


Figure 8. January Peak Day Utility Impact due to 16 Percent Saturation of Off-Peak Storage Systems with Conventional Discharge

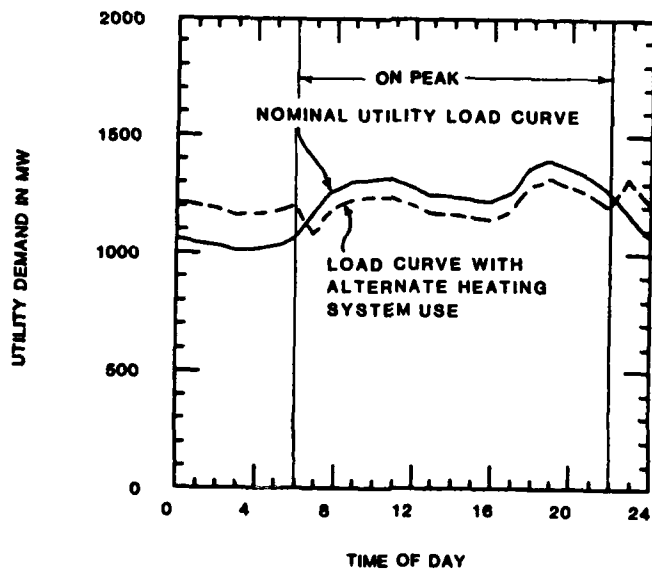


Figure 9. January Peak Day Utility Impact due to 16 Percent Saturation of Off-Peak Storage Systems with Proportional Discharge

been given in the past to control strategies designed to reduce coincident demand. The optimal control strategy described by Eqn. (4), however, is designed to reduce coincident demand. For a solar heating system, the proportional discharge strategy is a good approximation of this optimal control because of the nearly constant heating requirement on the utility's "worst" days.

The conventional, proportional, and optimal discharge strategies for the utility's peak load day in January are depicted in Figures 10, 11, and 12. The conventional strategy results in a very low electrical demand during the middle of the day. Comparison of the electrical demand in Figure 10 with the utility fuel cost in Figure 3 suggests that the solar contribution occurs at a time of low utility demand. In fact, the characteristics of the solar heating system under conventional control tend to accentuate the difference between the "peaks" and "valleys" on the utility load curve. The proportional and the optimal discharge strategies reduce the afternoon peak electrical demand. But the peak coincident demand still occurs in the morning, because there is little energy in storage at the beginning of the day. It is not until some energy has been collected that differences in the discharge strategies can be seen. It should be noted that this day happened to be sunny. If it had been a cloudy day, all 3 strategies would have obtained essentially identical results. The proportional strategy may help, but it will not hurt.

The results of simulations of a solar heating system with conventional, proportional, and optimal controls are presented in Table III. In January the peak coincident demand is reduced significantly by using proportional or optimal control, but the same is not true in December and February. The reason for the lack of improvement in December and February is that the day on which the peak coincident

demand occurred was the second of 2 successive cloudy days. There was very little energy in solar storage, so the discharge strategy, conventional or proportional, had little effect on system performance. But a completely discharged storage is a rather common occurrence during the peak heating season. During the spring and fall, the heating load is low, so storage is completely depleted less often, and the different discharge strategies have a more marked effect on overall system performance. The decrease in the coincident demand cost of supply for the proportional and optimal strategies, shown in Table III, is largely due to the improved performance during the spring and fall. The fuel cost of supply is virtually the same for each control strategy even though less solar energy is collected when either proportional or optimal control is used. This similarity of cost occurs because the proportional and optimal strategies save the collected energy to replace only expensive on-peak electrical energy.

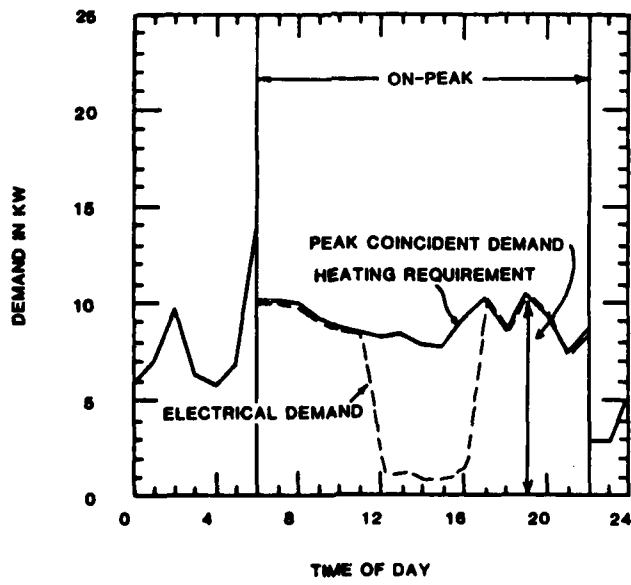


Figure 10. Conventional Strategy for Solar Storage on the Utility's Peak Load Day

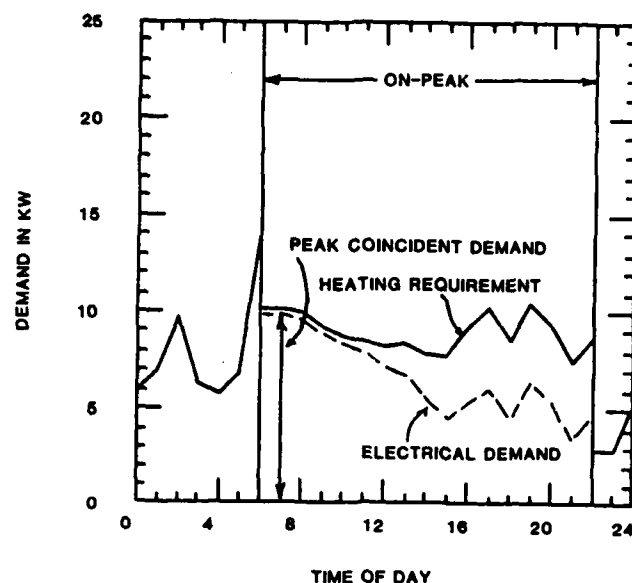


Figure 11. Proportional Strategy for Solar Storage on the Utility's Peak Load Day

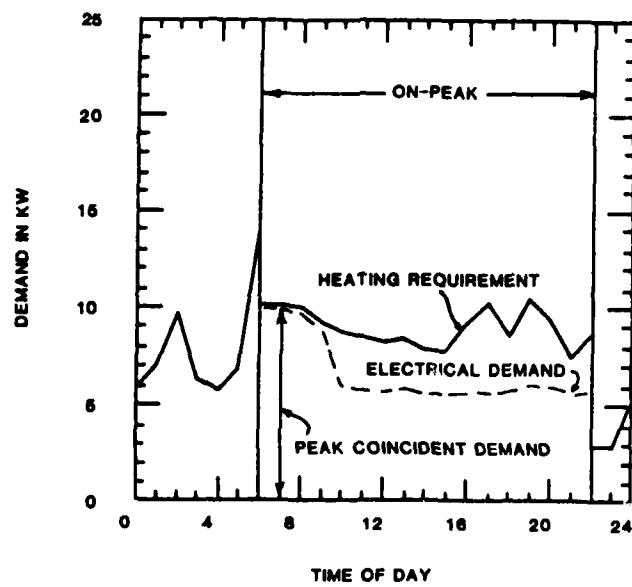


Figure 12. Optimal Strategy for Solar Storage on the Utility's Peak Load Day

Table III  
SOLAR STORAGE DISCHARGE STRATEGY COMPARISONS

	Baseline Heating System	Solar Heating System		
		Conventional Strategy	Proportional Strategy	Optimal Strategy
December Peak Coincident Demand	7.28 kW	6.83 kW	6.87 kW	6.78 kW
January Peak Coincident Demand	13.32 kW	13.07 kW	10.29 kW	9.59 kW
February Peak Coincident Demand	12.32 kW	11.84 kW	11.73 kW	11.74 kW
Coincident Demand Annual Cost of Supply in 1990 Dollars & % of Baseline	\$2551 100%	\$2227 87%	\$2020 79%	\$1905 75%
Fuel Annual Cost of Supply in 1990 Dollars & % of Baseline	\$1396 100%	\$705 51%	\$730 52%	\$691 49%
Total Annual Cost of Supply in 1990 Dollars & % of Baseline	\$3946 100%	\$2932 74%	\$2749 70%	\$2596 66%

Implementation of the optimal discharge strategy is more difficult for solar than for off-peak storage systems. In addition to needing an estimate of the heating load for the entire on-peak period, the optimal discharge of solar storage requires advanced knowledge of the amount of solar energy to be collected. But accurate prediction of the collection of solar energy is very difficult to achieve. Because of the high cost and difficulty of implementing the optimal control, the recommended strategy for solar systems is a proportional control strategy.

Figures 13 and 14 present the changes in the load curve on the peak heating load day if 34 percent of the new homes were to use solar heating systems with conventional and proportional control strategies.

This percentage results in the flattest utility load curve. The conventional strategy actually makes the utility load curve more uneven while the peak demand is unchanged. The use of solar heating systems with the proportional control strategy results in a more uniform load curve with a reduced peak demand.

**VI. Implementation**

The proportional discharge strategy can be implemented by using a microprocessor-based controller. The only input to the controller is the storage temperature, measured at specified time intervals throughout the on-peak period. These intervals are chosen to coincide with the time period used by the utility in determining the demand charges. The minimum allowable storage temperature is subtracted from the current storage temperature to establish the available energy in storage. The available energy in storage is then divided by the time remaining until the end of the on-peak period. This procedure fixes the maximum allowable rate of energy discharge from storage, from which T, the minimum allowable temperature at the end of this time interval, is established. The circulating pump is allowed to remove hot water from storage to satisfy the heating requirement. If T is reached before the end of the time interval, the pump is disabled until the start of next time interval. The process is repeated until the end of the on-peak period.

**VII. Conclusions**

We can use the methods of dynamic optimization to develop improved control strategies for use in off-peak energy storage and solar heating systems. These strategies cause the systems to be operated so that the heating requirements are satisfied, and the peak coincident demand is

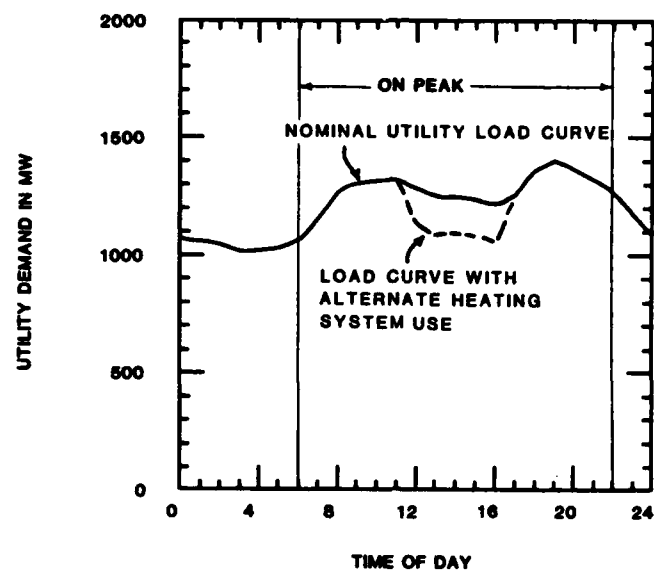


Figure 13. January Peak Day Utility Impact due to 34 Percent Saturation of Solar Heating Systems with Conventional Discharge

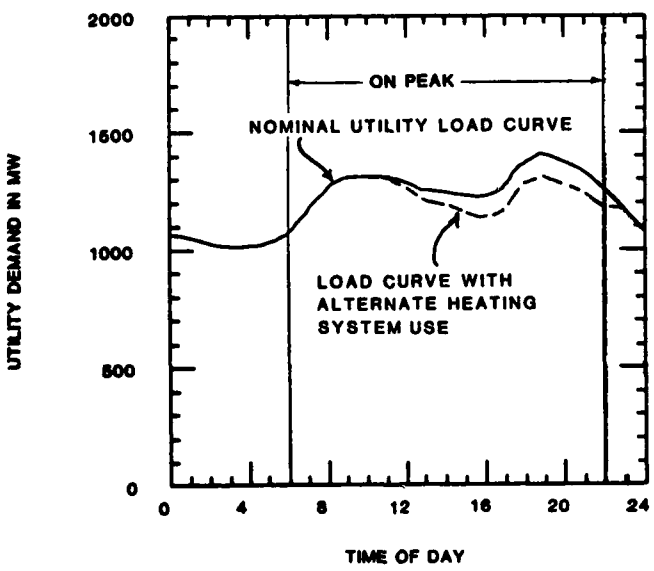


Figure 14. January Peak Day Utility Impact due to 34 Percent Saturation of Solar Heating Systems with Proportional Discharge

minimized. The optimal control strategies are difficult to implement because precise future knowledge of the time varying heating requirement is required; however, simple approximations of the optimal control strategies are easily implemented. These approximations, called proportional strategies, produce system performance clearly superior to that produced by conventional strategies. When the proportional strategy is used in place of the conventional control, computer simulations showed that the annual cost of electrical supply is reduced by 27 percent for off-peak storage heating systems and by 6 percent for solar heating systems. On a utility-wide basis, the use of the proportional control strategies results in a more constant utility load curve on the utility's peak day.

References

1. Arthur D. Little, Inc., "EPRI Methodology for Preferred Solar Systems (EMPSS) Computer Program Documentation," Arthur D. Little, Inc., Cambridge, Mass., 1978.
2. Zaininger Engineering Company, May 11, 1981, Personal Correspondence. Correspondence.
3. Bryson, A.E. and Y.C. Ho, Applied Optimal Control, Ginn and Company, Waltham, Mass., 1969.
4. Winn, R.C., "Optimal Control of Residential Heating and Cooling Systems," PhD Dissertation, Colorado State University, Fort Collins, CO, 1982.

USAFA-TR-83-15

## **SECTION V**

# **Engineering Education**

SOME TOPICS ON GAS FLOW: WAVE PROPAGATION (PART 1)

Daniel H. Daley\*

Editor's Note

The subject of wave propagation is one that most engineers have studied early in their careers. But like many "basic" subjects, it is one that we may not have thought about in a while. Sometimes it is interesting to take a fresh look at an old subject, and it is in this spirit that the following article on the mathematics and physics of wave propagation is presented.

This article is the first in a 2-part series. It introduces the wave equation by considering the motion of an elastic stretched string. Part 2, which will be published in the next issue of the Aeronautics Digest, will consider the application of the wave equation to linearized, 1-dimensional, unsteady gas flow.

I. Introduction

In many physical phenomena, a variation or disturbance in some property of a system is transmitted from point to point without transference of matter. This is called wave propagation. The motion of a disturbance along a stretched string, surface waves on water, sound waves, and electromagnetic waves are all examples of wave propagation. In the case of sound waves, the property disturbances being propagated are, simultaneously, displacement, pressure, and density. On the other hand, only one property disturbance, displacement, is propagated along a stretched string or along the surface of an incompressible fluid. When small disturbances are propagated in this manner, with no losses, the motion is described mathematically by the so-called wave equation. This equation was first derived for a vibrating string by d'Alembert in 1747 and for fluid motion by Leonhard Euler in 1759 (Ref. 1). Since a form of this equation arises in supersonic, linearized, 2-dimensional, steady flow of a gas, we plan to introduce the wave equation and examine its solution in this paper. The motion of an elastic stretched string, the prototype applied to problems involving wave propagation, will be

---

\*Colonel, USAF, Permanent Professor and Head, DFAN

used to introduce the wave equation.

### II. Wave Equation for Vibrating String

Consider a string having a mass per unit length of  $\rho$  and subjected to a uniform tension,  $\tau$ . The equilibrium position of the string lies along the  $x$ -axis. The displacement,  $y$ , of the string from the  $x$ -axis is taken to be so small that the tension,  $\tau$ , is constant; that the motion of any particle of string is perpendicular to the  $x$ -axis; and that the angle between the  $x$ -axis and any line tangent to the string is of such size that the sine, tangent, and radian value of the angle are all equal.

Figure 1 shows a small element of an isentropic string displaced from the  $x$ -axis.

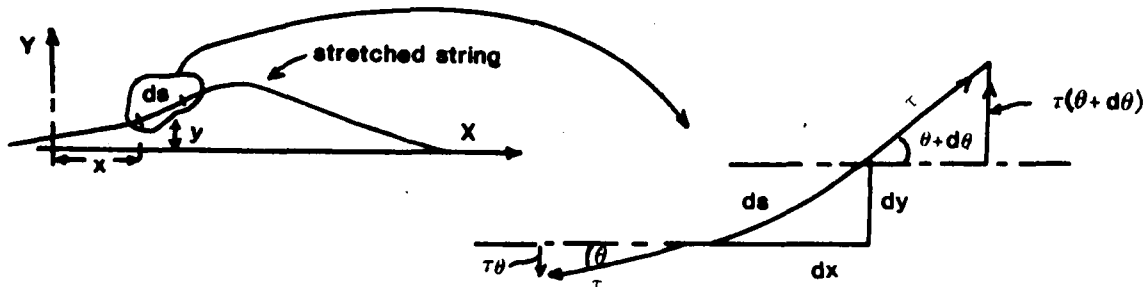


Figure 1. Forces Acting at Ends of String Element  $ds$  as Time t

We desire to find the equation of motion of this element. Since the displacement,  $y$ , of the element depends upon its position along the  $x$ -axis and time, we can expect the equation of motion to show a relation between the dependent variable,  $y$ , and the independent variables  $x$  and time,  $t$ . Because of the small displacement assumed,  $ds = dx$ ,  $\sin \theta = \theta = \tan \theta = \partial y / \partial x$  (why is this a partial derivative?), and  $d\theta = d(\partial y / \partial x) = (\partial^2 y / \partial x^2) dx$ . Applying  $F = ma$  in the form  $\delta F_y = (\delta m) a_y$  to the string

element shown in the y direction, we have

$$\delta F_y = -\tau \theta + \tau(\theta + d\theta) = \tau d\theta = \tau \frac{\partial^2 y}{\partial x^2} dx \quad (1)$$

$$\delta m = \rho ds = \rho dx \quad (2)$$

$$a_y = \frac{\partial^2 y}{\partial t^2} \quad (3)$$

so that the equation of motion for any element of the string is

$$\tau \frac{\partial^2 y}{\partial x^2} dx = (\rho dx) \frac{\partial^2 y}{\partial t^2} \quad (4)$$

or

$$\frac{\tau}{\rho} \frac{\partial^2 y}{\partial x^2} = \frac{\partial^2 y}{\partial t^2} \quad (5)$$

It is convenient to let

$$c = \sqrt{\frac{\tau}{\rho}} \quad (6)$$

where c has the dimensions of velocity. Using this we get

$$c^2 \frac{\partial^2 y}{\partial x^2} = \frac{\partial^2 y}{\partial t^2} \quad (7)$$

This equation, which describes and governs how the displacement, y, may vary with x and t, is called the wave equation. It is typical of motions in which a property variation (not necessarily a displacement) is propagated along a medium at a constant velocity, c.

The wave equation is known to be satisfied by any function in which the independent variables x and t always appear in the form  $(x + ct)$  or  $(x - ct)$ . For example, the dreamed-up function

$$y = A(x - ct)^3 + B \sin(x - ct) \quad (8)$$

will satisfy Eqn. (7). Using the chain rule of differentiation,

$$\frac{\partial y}{\partial x} = \frac{dy}{dz} \frac{\partial z}{\partial x} \quad \text{or} \quad \frac{\partial y}{\partial t} = \frac{dy}{dz} \frac{\partial z}{\partial t} \quad (9)$$

where  $z = x - ct$  in the present case, the derivatives  $\partial^2 y / \partial x^2$  and  $\partial^2 y / \partial t^2$  for the above function can be found. When these are substituted

into Eqn. (7), we find that the equation is satisfied by the function assumed above.

The general solution of the wave equation is expressed in the form

$$y = f(x - ct) + g(x + ct) \quad (10)$$

where  $f$  and  $g$  are any functions whatever of  $(x - ct)$  and  $(x + ct)$ , respectively. It is left as an exercise for the reader to show, by the procedure outlined in the example above, that Eqn. (10) does satisfy Eqn. (7). To investigate the physical meaning of the solution of the wave equation, let us set  $g = 0$  in Eqn. (10) and examine the solution  $y = f(x - ct)$ . In Figure 2 we plot  $y$  versus  $(x - ct)$  for this function.

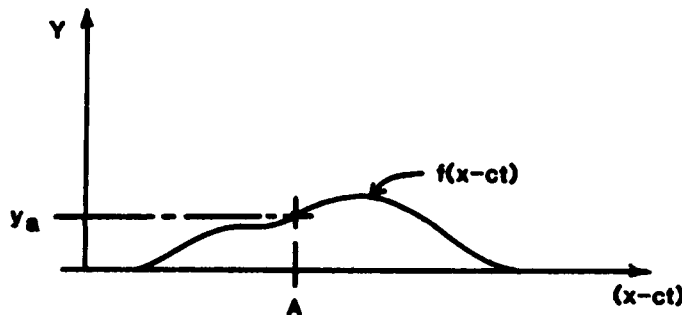


Figure 2. Arbitrary Curve Representing  $y = f(x - ct)$

Consider any point  $y_a$  on the curve in Figure 2 corresponding to a fixed value  $A$  of  $(x - ct)$ . Now, as time progresses, the value of  $(x - ct)$  corresponding to  $y$  remains fixed at  $A$  even though  $ct$  increases with time. This means that the  $x$  coordinate of  $y_a$  must increase with time such that, for increased values of  $ct$ ,  $x - ct$  remains constant at  $A$ . Since  $ct$  increases by an amount  $c$  in a unit interval of time,  $x$  must also increase by an amount  $c$  in a unit interval of time. It follows that the  $x$ -coordinate of  $y$  increases at the rate of  $c$ , and that the displacement  $y_a$  is propagating along the positive  $x$ -axis at this rate.

Let us illustrate the above points by using the  $x$ - $y$  coordinate

system. Again, we consider the solution  $y = f(x - ct)$ . The curve of this function is shown in Figure 3 at time  $t_1$ .

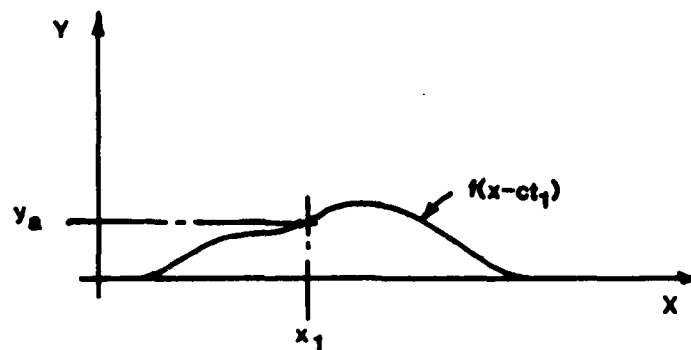


Figure 3. x-y Plot of the Function  $f(x - ct)$  at Time  $t_1$

This curve may be interpreted as the x and y coordinates of a disturbance in a stretched string at the instant  $t_1$ .

For any displacement  $y_a$  located at  $x_1$  on the curve of Figure 3 at time  $t_1$ , we ask, where will the displacement  $y_a$  be located along the x-axis as time progresses? The answer is that at any instant  $t$  later than  $t_1$ , the value of  $x$  corresponding to  $y_a$  will be such that the quantity  $(x - ct)$  at time  $t$  has the same value that it had at time  $t_1$ . This condition must be true, so that the function  $f(x - ct)$  will give the same value  $y_a$  at time  $t_1$  and  $t$ . Mathematically we write, for constant  $y_a$ ,

$$(x - ct) = (x_1 - ct_1) \quad (11)$$

or

$$x = x_1 + c(t - t_1) \quad (12)$$

which says that the x-coordinate of  $y_a$  at time  $t$  equals the x-coordinate of  $y_a$  at time  $t_1$  increased by an amount  $c(t - t_1)$ . Since  $y_a$  is any point on the curve of Figure 3, Eqn. (12) means that the x coordinates of all points on the curve and, hence, the curve itself, are increasing at the rate  $c$ . Therefore, the disturbance represented by

$$y = f(x - ct) \quad (13)$$

is propagating, without change in shape, along the positive x-direction at the rate  $c$ , as depicted in Figure 4.

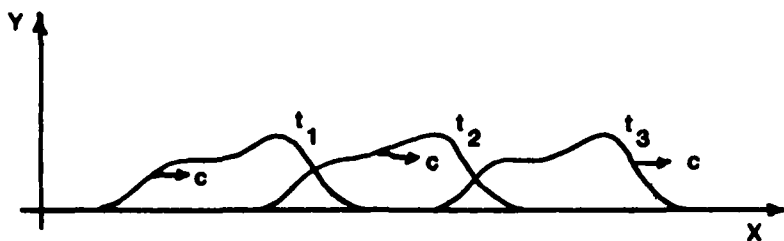


Figure 4.  $t_1$ ,  $t_2$ , and  $t_3$  Positions of a Wave Propagating along the x-Axis at Speed  $c$

A disturbance propagated in this manner is called a wave, and the motion represented by  $f(x - ct)$  is referred to as wave motion.

In Figure 4 we have interpreted the solution by referring to the x-y coordinate system at given times  $t_1$ ,  $t_2$ , and  $t_3$ . It is instructive to examine the motion further by referring to the x-t plane for any given displacements  $y_a$ ,  $y_b$ , and  $y_c$ . The lines in the x-t plane along which any given displacement  $y$  is constant are called characteristics of the wave equation. These characteristics, given by Eqn. (12), are shown by this equation to be straight lines having the slope  $c$  relative to the t-axis.

The characteristics corresponding to the function  $f(x - ct)$  are shown on the x-t coordinate system of Figure 5. A plot of  $f(x - ct)$  is also superimposed on this figure for the time  $t_1$ . The x-t diagram is a time table with the characteristic lines giving time and position information for any displacement  $y$  whose position is known at some given time. The displacements  $y_a$ ,  $y_b$ , and  $y_c$  shown in the figure at time  $t_1$  may be located at any time  $t_n$  by reference to the characteristics a, b,

and c, respectively. Conversely, the time at which any displacement on the curve at time  $t_1$  will be, or was, at a given location  $x_n$  is readily found when the characteristics of the wave equation are plotted on the x-t diagram. For example, the intersections of characteristics a, b, and c (with a horizontal line through  $t_n$ ) locate the x position of displacements  $y_a$ ,  $y_b$ , and  $y_c$  at  $t_n$ . Similarly, the intersections of a, b, and c (with a vertical line through  $x_n$ ) identify the times at which displacements  $y_a$ ,  $y_b$ , and  $y_c$  are at  $x_n$ .

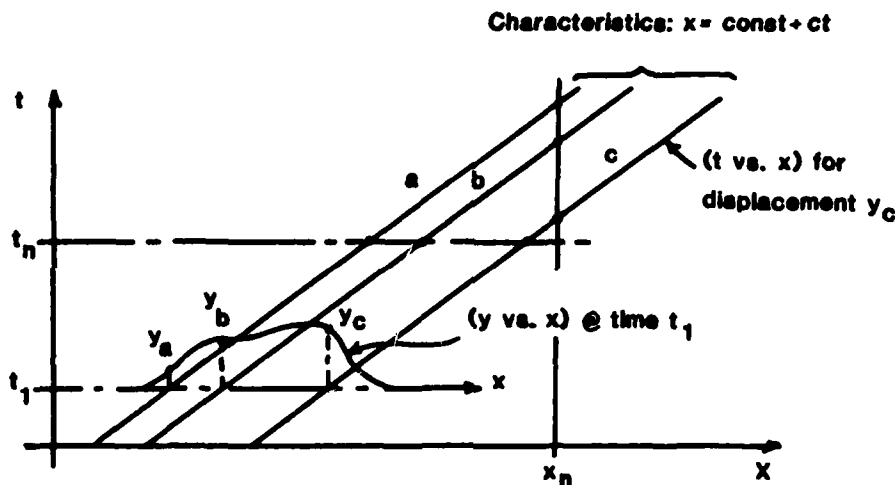


Figure 5. Characteristics in x-t Diagram

### III. Interacting Simple Waves

The discussion to this point has assumed that the function g of Eqn. (10) is 0. If we now take f to be 0 and consider the function g to be other than 0, we find that  $g(x + ct)$  corresponds to wave motion propagating along the x-axis in the negative direction. These leftward-propagating waves have characteristics given by

$$x + ct = \text{const.} \quad (14)$$

or

$$x = \text{const.} - ct \quad (15)$$

When the wave-equation solution involves only  $f(x - ct)$  or  $g(x + ct)$ , the wave described by the solution is called a simple wave. The wave shown in Figure 5 is a simple wave described by the function  $y = f(x - ct)$ . Figure 6 shows a leftward-traveling simple wave and a rightward-traveling simple wave along with their respective characteristics.

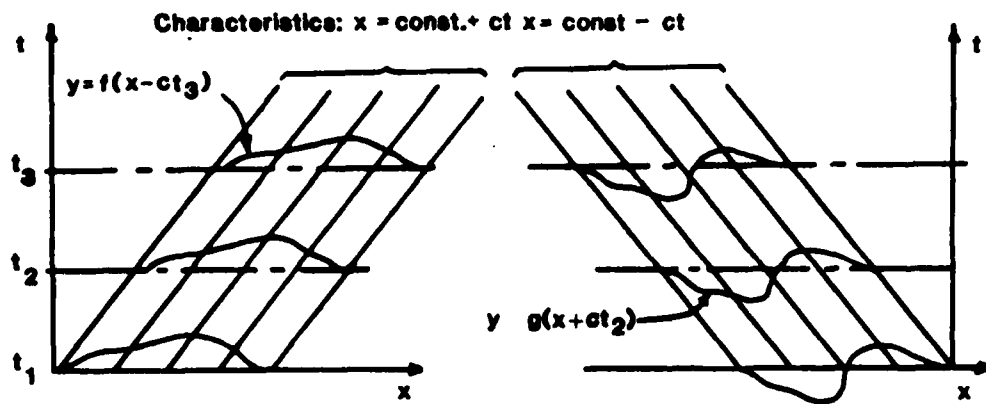


Figure 6. Rightward- and Leftward-Propagating Simple Waves

The characteristics of the waves are in the  $x$ - $t$  plane. To save space, the wave itself is shown at times  $t_1$ ,  $t_2$ , and  $t_3$  plotted in an  $x$ - $y$  plane superimposed on the  $x$ - $t$  plane. The zero point of the  $y$ -axis in this superimposed set of  $x$ - $y$  axes is coincident with  $t_1$ ,  $t_2$ , and  $t_3$  in turn.

A family of waves consists solely of leftward-traveling waves or of rightward-traveling waves. When both families of simple waves are present and intersect, their effects are additive within the general solution [Eqn. (10)] of the wave equation [Eqn. (7)]. These ideas are

illustrated in Figure 7, where the  $x-t$  and  $x-y$  diagrams are shown for a vibrating string.

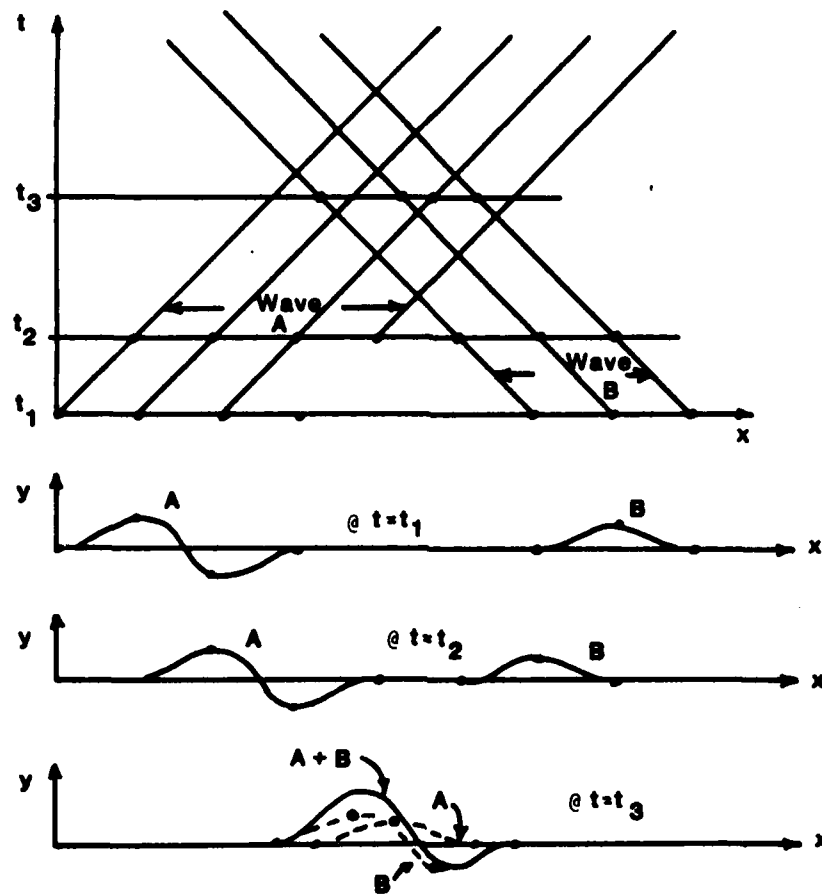


Figure 7. Motion of Vibrating String with Simple Waves of Each Family Interacting

The arbitrary rightward- and leftward-moving disturbances A and B, respectively, are propagating along the string at the rate given by  $\sqrt{\tau/\rho}$ . Some of the wave-equation characteristics are drawn in the  $x-t$  diagram for waves A and B.

With the position of the disturbances A and B known at time  $t_1$ , the  $x-y$  coordinates of the string can be determined at times  $t_2$  and  $t_3$ ,

because any given displacement  $y$  propagates along a given characteristic line in the  $x$ - $t$  diagram. The string locations, as determined by this method for times  $t_2$  and  $t_3$ , are shown in the figure. At  $t_3$  the string displacement is that resulting from adding A and B graphically. The mathematical justification for this addition follows from

$$y = f(x - ct) + g(x + ct) \quad (16)$$

where  $f$  and  $g$  are the  $y$  displacements denoted by A and B, respectively.

Any wave can be thought of as a combination of simple waves of both families. Thus, in principle, any wave may be resolved into simple waves of each family, very much as a vector may be resolved into components. As an example, consider a string with tension vibrating in its fundamental mode, as in Figure 8.

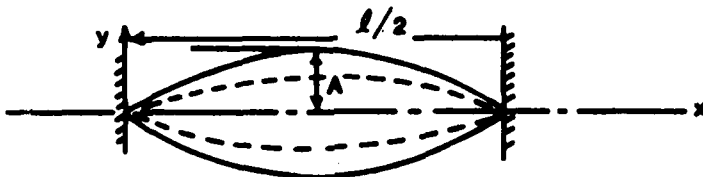


Figure 8. String of Length  $\ell/2$  Vibrating in Fundamental Mode

To start the motion, the string is displaced a distance  $A$  at its midpoint and released at time 0. Each point on the string then moves vertically about the  $x$ -axis in simple harmonic motion described by

$$y = (y_0) \cos \left( \frac{2\pi}{\ell} c t \right) \quad (17)$$

where  $c = \sqrt{\tau/\rho}$  and where the amplitude  $y_0$  of any element of the string is a function of its  $x$ -coordinate. The displacement amplitude at any value of  $x$  along the string is

$$y_0 = A \sin \left( \frac{2\pi}{l} x \right) \quad (18)$$

so that  $y_0 = 0$  at  $x = 0$  and  $l/2$ , and  $y_0 = A$  at  $x = l/4$  in agreement with the figure. The vibrating motion is fully described, then, by

$$y = \left( A \sin \left( \frac{2\pi}{l} x \right) \right) \cos \left( \frac{2\pi}{l} c t \right) \quad (19)$$

The motion represented by this equation can be interpreted as the result of rightward- and leftward-moving simple waves given by

$$y = f(x - ct) + g(x + ct) \quad (20)$$

where  $f$  and  $g$  are represented by

$$f(x - ct) = A/2 \sin \left( \frac{2\pi}{l} (x - ct) \right) \quad (21)$$

and

$$g(x + ct) = A/2 \sin \left( \frac{2\pi}{l} (x + ct) \right) \quad (22)$$

so that

$$y = A/2 \sin \left( \frac{2\pi}{l} (x - ct) \right) + A/2 \sin \left( \frac{2\pi}{l} (x + ct) \right) \quad (23)$$

At time  $t = 0$  Eqns. (23) and (19) give the same value of  $y$ . A plot of  $y$  versus  $x$  for Eqn. (23) at subsequent instants of time, using the characteristics of Eqn. (23) in the manner of Figure 7, will verify that the motion represented by Eqn. (23) is equal to that of Eqn. (19). Figure 9 shows the resulting motion corresponding to Eqn. (19) as determined graphically using Eqn. (23). It is convenient to use the non-dimensional time  $\bar{t} = t/P$ , where  $P$  is the period of the resultant motion given by  $P = l/c$ , and the non-dimensional distance  $\bar{x} = x/l$  for the  $x-t$  coordinates. For reference, the position of the displacements  $m$  and  $n$ , which propagate along the characteristics labeled  $m$  and  $n$ , are shown on the simple waves.

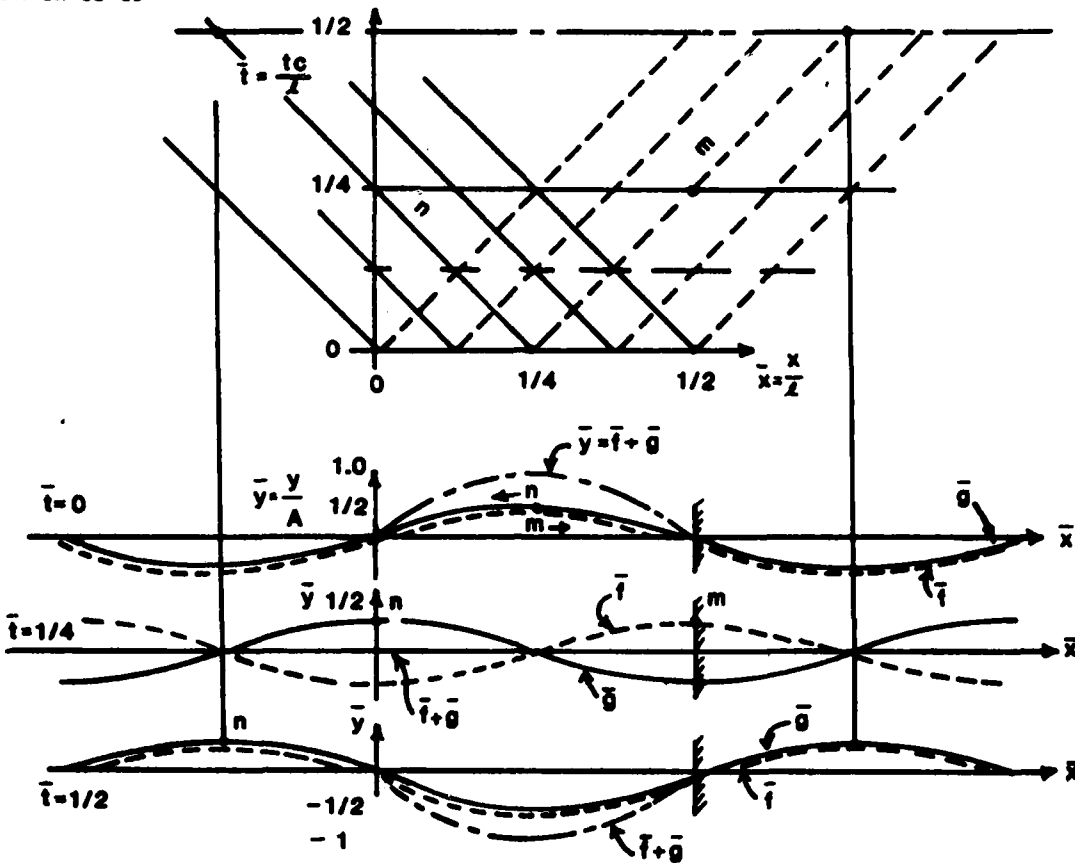


Figure 9. Motion of String Vibrating in Fundamental Mode as Sum of

$$(\bar{f} + \bar{g}) = \frac{f + g}{A} = \frac{1}{2} \sin(2\pi(\bar{x} - \bar{t})) + \frac{1}{2} \sin(2\pi(\bar{x} + \bar{t}))$$

#### IV. Conclusions

Our description of the vibration of Figure 8 (as superimposed simple wave motions) requires that we assume that a leftward-traveling simple wave is continuously entering the string at its right-hand end and leaving at the left-hand end, while a rightward-traveling wave is continuously entering and leaving the string in the opposite direction. In this simple example, we were able to write down explicitly the functions  $f(x - ct)$  and  $g(x - ct)$  for the motion. It would not have been necessary, therefore, for this example, to resort to the graphical solution of Figure 9. In general, however, one cannot easily write explicit mathematical equations for  $f$  and  $g$ . For this reason, the

graphical method of obtaining characteristics illustrated by Figure 9 proves to be a powerful tool for studying any general motion.

References

1. Thompson, Philip A., Compressible Fluid Mechanics, McGraw-Hill Book Company, New York, 1972, p. 162.

**SECTION VI**

**The Engineer's Bookshelf**

dichotomy is probably quite accurate, his statement also contains the answer to the dilemma: Scientists can bridge the gap between what they do and the great masses who do not understand its significance. That key concept is the art of writing well. Finkelstein differentiates between engineers and writers, implying that the two are mutually exclusive. But that assumption need not be true. Conscientious engineers will continually seek to develop, improve, and refine their writing skills. As they do so, they'll discover that writing isn't simply the act of recording predetermined data, but is the process of thinking, discovering, and creating what they actually know about their science.

When, through writing, engineers discover their science, they naturally want to share those discoveries with others. But to do so effectively, engineers need to translate the material for those readers who are not intimately familiar with the research or testing. Some scientists might argue, however, that it is demeaning to simplify, illustrate, or explain, in common language, their important discoveries. If you share this belief, please read the following statements written by three famous physicists. Albert Einstein said: "Most of the fundamental ideas of science are essentially simple, and may, as a rule, be expressed in a language comprehensible to everyone." (Ref. 2, page xxix) When many of us think of Einstein, we imagine a half-crazed genius, standing in front of a blackboard filled with complex formulas, and lecturing with a thick German accent. But much of his writing doesn't fit this stereotypical image. For example, Einstein, by using an analogy of tea leaves swirling in the bottom of a cup of tea, clearly described the effect of Brownian movement on the curvature of rivers. And he illustrated the famous theory of relativity by discussing the movement of trains at the depot in Berne, Switzerland. Einstein made his seemingly

complex ideas accessible to laymen by being always conscious of his audience, and by using language to express, not impress.

Another physicist who believes in clear writing is Werner Heisenberg, formulator of the "uncertainty principle." Discussing the obscure writing of some scientists, he said: "Even for the physicist the description in plain language will be a criterion of the degree of understanding that has been reached." (Ref. 2, page xxix) When we read "puffy" and obscure writing in many scientific journals, can we assume (as Heisenberg does) that the writers actually don't understand their science? Is bloated language simply a smoke screen concealing emptiness or a lack of thought?

Engineers obviously do a lot of thinking. They spend countless hours testing square missiles in wind-tunnel labs, computing Laplace transformations, and devising elaborate schematic diagrams illustrating the aerodynamic effects of flutter and divergence. What a shame if all this effort were wasted because the engineers had never learned the importance of good writing as the most effective means of communicating their findings to others! Or as Erwin Schrodinger asserts, "If you cannot -- in the long run -- tell everyone what you have been doing, your doing has been worthless." (Ref. 2, page xxix)

Maybe engineers would try harder to communicate with a lay audience if they actually felt others were interested in the results (and implications) of tests and experiments. For those engineers who are reading this article, may I assure you that many of us are interested (even fascinated) by what you're doing. In discussing the New Physics, Zukav expresses this same fascination for the work of Max Planck, Louis de Broglie, Max Born, and Niels Bohr:

Physics, in essence, is simple wonder at the way things are and a divine (some call it compulsive) interest in how that is so. Mathematics is the tool of physics. Stripped of mathematics, physics becomes pure enchantment. (Ref. 2, page 4)

I'm certainly not asking engineers to eliminate mathematics from their writing because I recognize what an important tool mathematics is. But I'm afraid that many engineers rely much too heavily on math, forgetting to explain what it means and why it's important.

Discovering and then explaining what the discovery means should be of equal importance in engineering. In fact, the engineer who can perfect and synthesize the two is destined for greatness. In The Dancing Wu Li Masters, Zukav argues that polished scientists and humanists have achieved that synthesis:

In short, scientists discover and technicians apply. However, it is no longer evident whether scientists really discover new things or whether they create them. Many people believe that "discovery" is actually an act of creation. If this is so, then the distinction between scientists, poets, painters and writers is not clear. In fact, it is possible that scientists, poets, painters and writers are all members of the same family of people whose gift it is by nature to take those things we call commonplace and to re-present them to us in such ways that our self-imposed limitations are expanded. Those people in whom this gift is especially pronounced, we call geniuses. (Ref. 2, pp. 9-10)

Yes, engineers who know how to write can create our tomorrows. So let's write, revise, write again, revise, and write again until we discover what our science actually means and then share that vision with others. For books that address these and many other provocative ideas, I highly recommend Pirsig's Zen and the Art of Motorcycle Maintenance and Zukav's The Dancing Wu Li Masters. Also, if you agree or disagree with my ideas, I'd like to hear from you. And I'd welcome your suggestions for topics you'd like to see me discuss in future editions of the Digest. My address is Department of English, USAF Academy, CO 80840.

#### References

1. Pirsig, Robert M. Zen and the Art of Motorcycle Maintenance: An Inquiry into Values, Bantam Books, New York, 1979.

USAFA-TR-83-15

2. Zukav, Gary. The Dancing Wu Li Masters: An Overview of the New Physics, Bantam Books, New York, 1980.

**USAFA-TR-83-15**

**SECTION VII**

**Errata**

## ERRATA

The following corrections should be made to issue number 9 of the Aeronautics Digest dated March 1983.

1. Page 6, Eqn. (3) should read:

$$\begin{aligned}
 C_{D_w}(\theta) = & -\frac{1}{2\pi q S_b} \left\{ \int_0^L \int_0^L S''(\xi) S''(x) \ln \left| \frac{x}{L} - \frac{\xi}{L} \right| d\xi dx \right. \\
 - & \left. \int_0^L \int_0^L \left[ S''(\xi) \frac{\beta}{2q} \frac{df}{dx} + S''(x) \frac{\beta}{2q} \frac{df}{d\xi} \right] \ln \left| \frac{x}{L} - \frac{\xi}{L} \right| d\xi dx \right. \\
 + & \left. \int_0^L \int_0^L \frac{\beta^2}{4q^2} \frac{df}{d\xi} \frac{df}{dx} \ln \left| \frac{x}{L} - \frac{\xi}{L} \right| d\xi dx \right\} \quad (3)
 \end{aligned}$$

2. Page 41, line 16 should read:

". . . the values of  $\gamma$  and  $C_p$  downstream . . ."

3. Page 41, line 18 should read:

". . . of  $\gamma$  and  $C_p$  are varied . . ."

4. Page 62, the title of Figure 5 should read:

". . . (for Given PR and  $N/\sqrt{\theta}$ )"

END

FILMED

12-83

DTIC